A Radar-Based In-Cabin Health Monitoring System

by

Ali Gharamohammadi

A thesis
presented to the University of Waterloo
in fulfillment of the
thesis requirement for the degree of
Doctor of Philosophy
in
Mechanical and Mechatronics Engineering

Waterloo, Ontario, Canada, 2024

Examining Committee Membership

The following served on the Examining Committee for this thesis. The decision of the Examining Committee is by majority vote.

External Examiner	Name: Alessandro Cidronali Title: Professor Department: Department of Information Engineering University: University of Florence
Supervisor(s)	Name: Amir Khajepour Title: Professor Department: Mechanical and Mechatronics Engineering Name: George Shaker Title: Adjunct Assistant Professor Department: Electrical and Computer Engineering
Internal Member	Name: Arash Arami Title: Assistant Professor Department: Mechanical and Mechatronics Engineering
Internal-external Member	Name: Nima Maftoon Title: Assistant Professor Department: Systems Design Engineering
Internal-external Member	Name: Plinio Morita Title: Associate Professor Department: Public Health and Health Systems

Author's Declaration

I hereby declare that I am the sole author of this thesis. This is a true copy of the thesis, including any required final revisions, as accepted by my examiners.

I understand that my thesis may be made electronically available to the public.

Abstract

The topic of in-cabin health care monitoring within vehicles has recently garnered significant attention. This technology serves two primary applications in a vehicle. First is the monitoring of the vital signs of drivers and passengers. Given the significant amount of time individuals spend driving daily, it is essential to monitor their vital signs to identify potential health issues at an early stage. If there is a health condition, autopilot mode of vehicle can be used. Second, it facilitates occupancy detection, which is crucial in detecting instances of a child being left behind in a vehicle. As a result, the need for in-cabin health care monitoring is rapidly increasing.

Radar technology is particularly popular for use in health monitoring systems due to a number of reasons, one of which is the privacy concern. While vision and thermal cameras can also be used for health monitoring, they may be perceived as invasive to an individual's privacy. Additionally, radar-based health monitoring systems are contactless, making them more suitable for in-vehicle applications where maintaining a certain distance from the subject is necessary. In addition, radar technology is often more cost-effective than other types of sensors.

In this thesis, frequency-modulated continuous wave (FMCW) radar systems are employed for in-cabin health monitoring. A dual radar system has been developed to monitor breathing patterns during driving, with a specific focus on detecting potential breathing issues. Because abdominal breathing may result in reduced chest displacement, it's essential to monitor both the chest and abdomen for early detection of any breathing abnormalities. In this system, separate radars are employed to monitor the movements of the chest and abdomen simultaneously. Various breathing abnormalities, including Tachypnea, Bradypnea, Biot, Cheyne–stokes, and Apnea, are explored. The proposed algorithm can detect the mentioned breathing abnormalities through breathing rate (BR) estimation and breath-hold period detection. In addition, the proposed method in this thesis estimates BR based on the multiple range bins. The experimental results demonstrate a maximum BR error of 1.9 breaths per minute using the proposed multi-bin technique. In addition, the dual radar fusion system can detect breath-hold periods with minimal false detections.

Secondly, multi-input-multi-output (MIMO) FMCW radars have been developed to monitor multiple people inside the vehicle in two different applications, including vital sign monitoring and occupancy detection. For vital sign monitoring, digital beamforming algorithms are explored to monitor various angles inside the vehicle. Different scenarios involving either a single subject or multiple subjects were deployed. The results indicate that the proposed system can monitor the breathing patterns of multiple subjects simultaneously when they are seated in the same row. However, when they are seated in different rows, the

reflected signals from subjects in the second row are combined with the subjects in the first row due to the multipath inside the vehicle. For occupancy detection, a novel approach that involves detecting the occupied space in each seat is presented in this thesis. The variance of detected points is suggested as an indicator of volume occupancy. In the conducted experimental study, which covers 70 different scenarios involving both single-subject and multi-subject situations, each seat is categorized into one of three labels: adult, baby, or an empty seat. The proposed approach achieves an overall accuracy of 96.7% using an AdaBoost classifier. Additionally, a miss-detection rate of 1.3% is achieved when detecting babies. The proposed approach demonstrates better robustness to multipath compared to the more commonly used energy-based approaches.

Thirdly, a radar system operating at 60 GHz and using FMCW technology is positioned behind a seat to monitor an individual's heart waveforms. The suggested algorithm accurately recognizes specific patterns in healthy subjects' heart waveforms, depicting two peaks followed by a valley in each cycle. High-frequency components related to breathing, often present in the heart band, are eliminated through variational mode decomposition (VMD) to refine the reconstructed heart waveform. The proposed method effectively detects and compensates body movements in seated individuals in the time domain, utilizing multiple range bins to identify and remove signals affected by strong body movements. A comprehensive investigation into heart rate variability (HRV) and heart rate (HR) estimation yields a median interbeat interval (IBI) estimation error of 30 ms and an average relative error of 4.8% for HR estimation using the VMD and multi-bin approach. Furthermore, the study focuses on analyzing a group of older adults to detect heart conditions, with those exhibiting a prolonged corrected QT interval (QTc) showing distinct heart waveforms compared to those without this condition. This specific heart waveform can serve as an indicator for detecting the mentioned heart condition. Additionally, the research delves into human body vibrations within vehicles, particularly in the presence of car body vibrations induced by road defects like cracks and potholes. A threshold based on z-axis acceleration is set to detect these road defects; exceeding 12 m/s^2 leads to the omission of the corresponding signal, followed by employing an autoregressive integrated moving average (ARIMA) model with forward forecasting to reconstruct the omitted sections. The experiments reveal a median IBI estimation error of 37 ms and an average relative error of 5.9% for HR estimation

Acknowledgments

First and foremost, I extend my heartfelt gratitude to my esteemed supervisors, Prof. Amir Khajepour and Prof. George Shaker, whose unwavering support, invaluable guidance, and constant encouragement have been instrumental throughout my PhD journey. Their expertise, mentorship, and scholarly wisdom have not only shaped my academic and research endeavors but have also instilled in me a profound understanding of engineering ethics and professionalism. I am truly fortunate to have had the privilege of working under their supervision, and I am deeply indebted to them for their profound influence on my scholarly growth and personal development.

I would like to express my sincere gratitude to Prof. Mohammad Pirani for his invaluable contributions to my research. His insightful comments, constructive feedback, and expert guidance have greatly enhanced the quality and rigor of my work.

I would also like to thank my friends and colleagues in the Wireless Sensors and Devices Lab (WSDL) and Mechatronic Vehicle Systems Lab.

Most importantly, I would like to express my deepest gratitude to my family - my parents, my brothers, and my nephew- for their unwavering support and encouragement throughout my life especially during this academic endeavor. Their love, encouragement, and unwavering belief in me have been a constant source of inspiration and motivation.

Table of Contents

List of Figures

List of Tables

List of Abbreviations

ADC	analog-to-digital converter
AI	artificial intelligence
BR	breathing rate
CFAR	constant false alarm rate
CWT	continuous wavelet transform
DAS	delay and sum
ECG	Electrocardiogram
EEMD	empirical mode decomposition
FCC	Federal Communications Commission
FMCW	frequency-modulated continuous wave
FFT	fast Fourier transform
HBMC	human body motion cancellation
HR	heart rate
HRV	heart rate variability
IR	infrared
LA	left atrium
LV	left ventricle
MIMO	multi-input-multi-output
MLE	maximum likelihood estimator
MUSIC	multiple signal classification
MVDR	minimum variance distortion less response
PCA	principal component analysis
PCTD	peak counting in the time domain
PFTV	peak of FFT of the target's vibration
pNN50	percentage of successive IBIs that differ by more than 50 ms
PPG	photoplethysmography
QTc	corrected QT interval
RA	right atrium
RMSSD	root mean square of successive difference

RV	right ventricle
SDRR	standard deviation of the RR interval
TI	Texas Instrument
UWB	ultra-wideband
VMD	variational mode decomposition
VVC	vehicle vibration cancellation

Chapter 1
Introduction

The field of in-cabin monitoring is rapidly emerging as a crucial aspect and popular area of study in the realm of smart car technology, both in terms of comfort and safety. This is primarily driven by the increasing amount of time we are spending on our daily commutes. This highlights the need for implementing measures to monitor the vital signs and physiological state of drivers and passengers, such as BR, HR, and HRV. There are several technologies available for in-vehicle occupancy detection. Among these, mechanical sensors that can measure weight, force, acceleration, or pressure are the most commonly used. These sensors can detect the presence and position of the occupants in the vehicle and can also be used to adjust the vehicle's settings, such as airbag deployment, seat belt tension, and climate control [1], [2]. Mechanical sensors can be divided into three common categories, including resistive [3], inductive [4], and capacitive [5]. Both resistive and inductive sensors have difficulty discriminating between humans and objects [6]. Capacitive sensors that can detect electric dispersion effects on human tissues are prone to high false detections [7]. Other commonly used technologies include camera vision [8], [9], and infrared (IR) sensors [10]. Although these sensors are more reliable, they pose privacy issues and are sensitive to sunlight and illumination levels. To overcome these challenges, radar technology can be employed.

In recent years, several innovative monitoring technologies have been proposed and developed inside the vehicles. One such technology is radar-based monitoring, which offers two major advantages over conventional camera-based or optical sensors: the ability to detect and monitor subjects through non-metallic objects [11] and the inherent privacy-preserving nature of its operation [6]. These benefits can be leveraged for applications beyond safety-related ones by continuously monitoring the postures and vital signs of vehicle occupants, such as airbag deployments or the detection of children left behind. This technology can also be used for functionalities such as controlling the air conditioning, gesture recognition for the human-machine interface of the vehicle infotainment system, and advanced health monitoring [6], [12], [13].

As noted earlier, radar-based sensors are one of the most promising ways to address the issues of dead spots in camera vision and dependence on environmental factors. This is why radars are now often explored to monitor people in different places, such as seniors homes [14], [15], vehicle cabins [16], and hospitals

[17]. In the automotive industry, Hyundai and Toyota have reportedly developed a radar-based monitoring system able to detect whether children have been left behind in the rear seat's dead spot [18], [19].

Table 1-1 represents various key applications of radar inside a vehicle based on the indexed papers and patents found on Google Scholar. The number of papers on occupant status monitoring and occupancy detection has increased in recent years. Occupant status monitoring is the most studied application, as research on driver health monitoring can help prevent car accidents. The primary approach in this application is to estimate BR and HR. Most studies have focused on accurate BR and HR estimation. However, deciding after BR and HR estimation can be more beneficial. One of the benefits of in-cabin radars is to detect drowsy drivers by identifying low BR or Apnea [20], [21], [22]. According to statistics, almost 30% of fatal car accidents involving deaths are caused by drowsy drivers [20].

Table 1-1: Different in-cabin monitoring applications by radar.

Key application	Main approach	Case study	Reference
Occupant status monitoring	BR and/or HR estimation	None	[23], [24], [25], [26], [27], [28], [29], [30], [31], [32], [33], [34], [35], [36], [37], [38], [39], [40], [41], [42]
		Sensor placement for accurate BR estimation	[43], [44], [45]
		Vital sign monitoring in an ambulance	[46]
		Drowsy driving detection	[20], [22], [47], [48], [49], [50]
		Biometric driver seat	[44]
		Angry driver	[51]
		Multiple targets' vital sign monitoring	[52], [53]
		Car vibrations suppression	[25], [54], [55], [56]
	Changes in the reflected power	Distracted driver detection by cellphone	[47]
		Random body movement cancellation	[25], [45], [57]
		Airbag	[58]
	Range-doppler map	Distracted/drowsy driver based on head motion	[59], [60], [61], [62], [63], [64]
	Range Doppler map, Changes in the phase of signals	Drowsy driver based on eye blink frequency	[21], [65], [66], [67], [68], [69]

Occupancy detection	Range-doppler map or time-frequency spectrum	Artificial intelligence (AI) to detect occupied seats	[6], [7], [70], [71], [72], [73], [74], [75], [76], [77], [78], [79], [80], [81], [82], [83], [84], [85], [86], [87], [88], [89], [90], [91], [92], [93], [94], [95]
	The amplitude of reflected signals	Left-behind child	[11], [96], [97], [98], [99], [100], [101], [102], [103], [104], [105], [106], [107], [108], [109], [110], [111]
	BR and HR difference	BR and HR estimation	[112], [113], [114]
Gesture recognition to assist drivers	Micro-doppler features	AI to detect gestures	[115], [116], [117], [118], [119], [120], [121], [122], [123]

The purpose of this thesis is to develop radar technology for in-cabin applications focusing on vital signs monitoring of drivers and passengers, including BR, HR, and HRV. In addition, this thesis proposes a novel approach to occupancy detection based on occupied volume.

1.1 Motivation

The technology of in-cabin vehicle health monitoring is rapidly becoming an essential component of passenger and vehicle safety. A number of monitoring technologies have been proposed and developed for this purpose, including RGB cameras [124], thermal cameras [125], and radars [126]. Among these technologies, radars offer a significant advantage over other sensors by allowing for subject detection and health monitoring without violating privacy. This benefit can be utilized for continuous monitoring of people's postures and vital signs. Many potential applications exist for radar-based technologies inside a vehicle [127]. As more precise radar-based occupant monitoring technologies are developed, it will be possible to enable a range of functionalities, such as controlling the air conditioner, gesture recognition for human-machine interfaces, and health monitoring. Health monitoring is the most crucial application of these functionalities inside a vehicle, as it allows for the estimation of vital signs such as BR, HR, and HRV [128].

Monitoring an individual's breathing and cardiac can be an important factor in determining their health and well-being during driving. Since driving accounts for a considerable amount of our daily lives, it is essential to track the status of drivers and passengers consistently to identify potential safety problems as early as possible. Driver status monitoring is the most practical factor that can enable advanced driver assistance systems to control the vehicle in emergencies, such as situations when the driver encounters Apnea, fatigue, stroke, trauma, or stress [45]. Breathing and heart patterns can provide important information about an individual's level of relaxation, stress, or fatigue, all of which can impact their ability

to operate a vehicle safely. As a result, monitoring the breathing and cardiac health of drivers and passengers is a crucial task that can be accomplished by contact and non-contact sensors.

The global population has witnessed a growing incidence of fatalities attributed to chronic and cardiovascular condition [129], [130]. Electrocardiography and echocardiography are the established standards for monitoring heart activity. Electrocardiograms (ECGs) track the heart's electrical activity, while echocardiograms provide insights into the heart's structure and blood vessels[131], [132]. These tools are effective for detecting cardiovascular conditions but come at a significant cost and require specialized training to operate. FMCW radar, a highly motion-sensitive sensor, offers a cost-effective and user-friendly alternative for certain conditions. Despite operating at millimeter wavelengths with limited skin penetration [43], FMCW radar can still detect skin vibrations caused by heartbeats. By correlating these movements with the ECG signal, which associates heart motions with P, Q, R, S, and T-waves, employing cardiological insights in conjunction with radar sensors is attainable. Recent studies primarily focusing on HR estimations are documented in references [133], [134], [135], [136], [137].

1.2 Objectives

The first objective of this Ph.D. thesis is to develop an advanced wireless sensor system utilizing mm-wave signals to monitor the health conditions of both drivers and passengers. Most recent studies are designed for use in an office or home [138], [139], [140]. Monitoring vital signs inside a vehicle is a challenging task due to the presence of various sources of noise that can degrade the quality of the signals being measured. FMCW radars provide a high-range resolution signal that can be used to overcome these challenges [141], [142], [143], [144] and enable monitoring of vital signs in a vehicle.

However, there are several challenges in using radars for health care monitoring inside vehicles. Due to the confined space inside a vehicle, the passengers' reflections can interfere with the driver's reflections. These interferer reflections pose a challenge in the detection of abnormal breathing and heart patterns [25]. Since the driver is non-vibrant during a breath-hold period, an interfering reflection from a vibrant passenger can be misinterpreted as a driver's reflection. This challenge can be addressed either by designing an optimum signal or an optimum setup.

The second objective of this thesis is to monitor breathing and heart patterns during normal driving activities, such as turning the wheel and shoulder checking, even when these activities are not periodic [57]. Some of the studies employed an expensive and intricate system to mitigate the effect of these movements [145], [146]. These studies used a less practical package size for this purpose, which adds discomfort for

the drivers. Therefore, it is crucial to use an affordable system to monitor individuals inside the vehicle. The aim of this thesis is to monitor the health condition of people while driving using off-the-shelf mm-wave radars, known for their compact size. These radars can sweep a high-frequency bandwidth. As the human body captures more than one range bin in these radars inside the vehicle, multiple range bins can be used for breathing patterns and heart waveform estimation.

Another objective of this thesis is to monitor the heart waveforms of individuals inside the vehicle as they can reveal crucial information. However, real-world scenarios present four major challenges that need to be addressed: high-frequency harmonics of breathing, body movements, range bin selection, and car body vibrations. In [132], [147], [148], [149], [150], [151], [152], [153], the participants were asked to hold their breath or breathe shallowly while seated to mitigate issues related to high-frequency harmonics of breathing and body movements. Additionally, in [154], [155], [156], some signal processing approaches have been employed to remove high-frequency harmonics of breathing and compensate for body movements. However, range bin selection is still a challenge in these investigations. Regarding car body vibrations, a mathematical investigation in [54] refines signals corrupted by car vibrations. However, this work lacks real-life scenario evaluation.

This thesis will delve into the technical aspects of utilizing mm-wave radars for in-cabin health monitoring. The goal of this thesis is to develop a novel, non-contact solution for vital sign monitoring in driving scenarios by using mm-wave radars. Additionally, it is crucial to monitor unhealthy participants, as recent studies have primarily focused on healthy participants only.

1.3 Thesis Outline

This thesis is structured as follows. In the second chapter, an overview of the existing literature concerning in-cabin health monitoring using radar technology is provided, including occupant status monitoring, occupancy detection, and gesture recognition for driver assistance. Additionally, important case studies for vital sign monitoring are reviewed.

In the third chapter, a novel method based on multi-bin breathing rate estimation using a dual radar system is presented. The proposed signal processing chain capable of detecting a wide range of breathing abnormalities, including Tachypnea, Bradypnea, Biot, Cheyne–stokes, and Apnea is explored. Additionally, different driving scenarios are tested by a dual radar system, and the results of the proposed breathing rate estimation are compared with those of conventional techniques.

In the fourth chapter, the monitoring of multiple individuals using a MIMO radar technology is investigated. The beamforming algorithm is employed to analyze radar data with known angles and ranges, enabling the extraction of breathing waveforms within the vehicle. The objective is to monitor multiple individuals inside the vehicle, considering variations in distance or angle from the radar. Furthermore, the chapter explores occupancy detection within the vehicle using a MIMO radar, with a specific focus on detecting children left behind.

In the fifth chapter, the heart waveform estimation system is proposed by a single radar installed behind the seat. First, a specific heart waveform is introduced as a healthy heart waveform. Other vibrations that can corrupt heart waveform are suppressed such as human body movements, breathing harmonics, and car body vibrations. Second, this specific heart waveform is also explored in people with QTc condition.

In the sixth chapter, the main findings of this study are concluded, and future works are highlighted. Firstly, the summary of contributions is highlighted, including novel dual radar fusion approach for breathing monitoring and exploration of heart waveform patterns in both healthy and unhealthy subjects. Secondly, the societal impact of this research is discussed. Thirdly, limitations of this research are acknowledged, and potential future works are introduced. Finally, publications of this research are listed.

In the appendices, there is a comprehensive review of recent studies in sensor selection, employed ground truth for in-cabin applications, most commonly used radars, and some studies based on micro-Doppler signatures for occupancy detection and gesture recognition. In addition, the proposed BR estimation approach is compared with the conventional one in some areas in Appendix F.

Chapter 2
Literature Review

This chapter presents a review of the literature on in-cabin health monitoring by radar, including occupant status monitoring, occupancy detection, and gesture recognition for driver assistance. For more details about the advantages of radar over other sensors in BR estimation, refer to Appendix A.

2.1 Different Applications of Radar Inside a Vehicle

Table 1-1 summarizes different in-cabin applications of radar, main approaches, and literature case studies. Figure 2.1 depicts the distribution of different approaches. The majority of studies have focused on occupant status monitoring. The number of publications showed a significant increase in 2021 and 2022, especially on occupant status monitoring approaches.

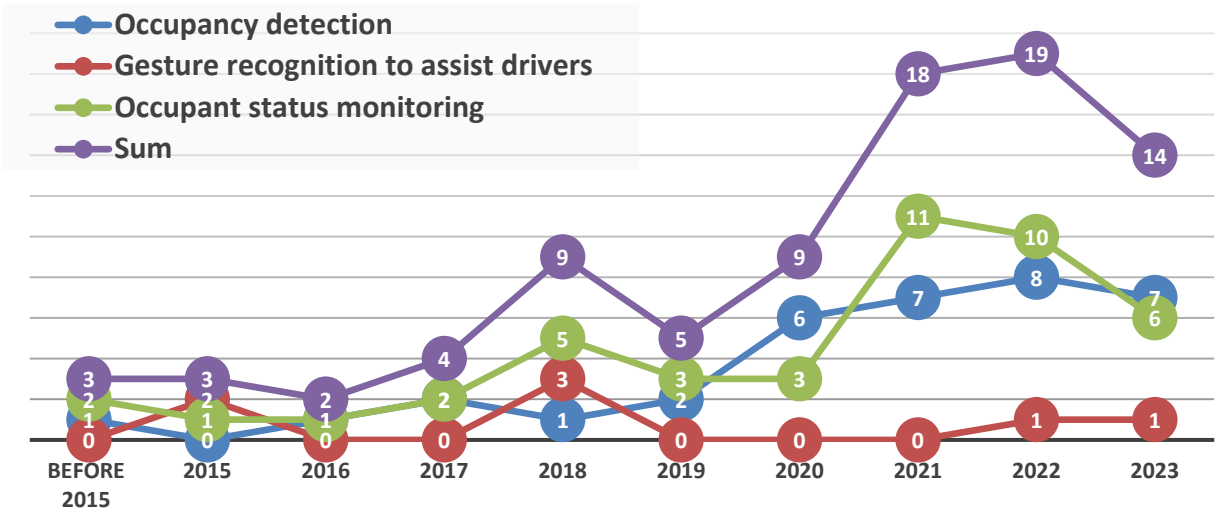

Figure 2.1: Distribution of recent studies in different approaches over the years.

2.1.1 Occupant Status Monitoring

Recent investigations mostly focused on occupant status monitoring for various reasons. Status monitoring is a major factor in assessing a person's health and detecting emergencies due to respiratory distress and heart attacks. Monitoring vital signs like BR can also reveal crucial information about a person's well-being and may reveal a variety of health conditions [157]. As the body tries to maintain the amount of oxygen available to the tissues, a change in BR is typically the first indication of a health issue [158], [159]. As

driving is increasingly becoming an inevitable part of our day, monitoring a driver's vital signs can enable early detection of health issues. This could enhance road safety.

Monitoring drivers can also alert them if they are experiencing stress or sleepiness, which can impact the risk of accidents. [25]. There are some ways to determine if the driver is sleepy. Most papers used HR and BR monitoring. A sudden decrease in BR and HR is indicative of driver drowsiness [20], [22], [47], [48], [49]. Additionally, head motion and eye blink frequency also can be monitored to detect sleepy drivers [21], [59], [60], [61], [65], [66], [67], [68], [69]. Recent studies have primarily utilized features extracted from micro-Doppler signatures. In [66], [68], a 77 GHz radar has recorded signals from eyeblink. They have used ensemble empirical mode decomposition to remove unnecessary information. Based on useful information, the signals were reconstructed and fed to a short-time Fourier transformation. Finally, a cell-average constant false alarm rate (CFAR) technique was applied to detect eye blinks. In [69], heartbeat and respiration signals were filtered before applying CFAR.

There are many ways to identify distracted drivers by radars. The most common solution is the use of micro-doppler signatures, especially head motions [59], [60], [61]. In [61], different head motions have been classified based on velocity-time maps by a neural network generated from a millimeter wave radar at 77 GHz placed in front of the driver. In [59], the range-time maps have been utilized to monitor head movements by a 60 GHz radar. Another common distraction is mobile usage. A distracted driver using a mobile can be recognized by scanning the reflected energy over time [47]. Anger issues can also be addressed by radars. In [51], the authors have focused on detecting an angry driver. They rely on changes in breathing rhythm and HR. If the detected anger exceeds the threshold value, the device sends a signal to the voice device mounted on the vehicle to play music to relieve anger.

It can be seen in Table 1-1 that a large number of recent works focused on measuring BR and HR accurately. In [23], [24], [25], [26], [27], [32], [160], the authors used different methods to reach this objective. When it comes to pulmonary diseases, respiratory rates may be used together with breathing patterns to both diagnose and track a person's health concerns. While the average resting respiratory rate varies from person to person, it generally ranges between 12 and 20 breaths per minute [161]. Apnea (cessation of breathing), Bradypnea (low respiratory rate), and Tachypnea (high respiratory rate) are the three types of abnormal respiratory rates [162]. Other atypical breathing patterns have been documented in [157].

Many aspects should be considered in system and signal design for abnormal driver and passenger behavior detection. For more information about ground truth, radar brand and/or package size, and some related works in breathing rate estimation, refer to Appendix B, Appendix C, and Appendix D, respectively.

2.1.2 Occupancy Detection

The importance of occupancy detection by radar is further accentuated within the context of a vehicle. The detection of occupants is a crucial step as it enables other applications, such as status monitoring, to be activated [6]. This is due to the high computational cost associated with vital sign estimation. Therefore, when a seat is unoccupied within a vehicle, it is unnecessary to apply vital sign estimation, reducing computational cost and increasing system efficiency.

Researchers have proposed some assumptions for occupancy counting by radars. Most in-use systems have been evaluated with groups of individuals that were well-spaced apart from one another in a wide area. Additionally, the locations of the individuals were not determined, and some systems could only estimate the number of people. Hence, most existing approaches for estimating the population in a large space using radars need quite complicated signal processing techniques that result in high computational costs [6].

A simple approach by radar for occupancy detection is to count Individuals entering and leaving at the entrance. In [163], [164], [165], it is demonstrated how to count several people moving through a broad entrance or passageway at once. Their suggested approaches relied on patterns of received signals according to the population while the radar was mounted at a height of 2.3 meters on the roof to cover a large area. This methodology employs a simpler approach to counting occupants.

There are three main approaches by radar inside a vehicle cabin for occupancy detection. In the most common approach, researchers rely on the extracted features from micro-doppler signatures [6], [7], [70], [71], [72], [73], [74], [75], [76], [77], [78], [79]. This approach employs AI to detect and classify occupied seats after feature extraction. In fact, these features are fed to AI to be used in classification. These signatures can also appear in different other types of data like time–frequency [71], [72], [73], [77], [79].

On the other hand, other researchers employed the reflected energy to detect occupancy. The most common usage for this approach is the left-behind children detection to save children and pets and avoid death in excessively hot or cold conditions [11], [73], [96], [97], [98], [99], [100], [101], [102], [103], [104]. Some studies have used this approach to detect a single occupied seat [25]. These studies focused on driver detection before vital signal monitoring. Finally, in the third approach, researchers proposed to use

vital sign signals to count occupied seats [77], [112]. This approach presents the most reliable solution for the left-behind problem.

In [166], an occupancy detection approach based on occupied space is introduced. While this method is less reliant on the distance from the radar, the radar setup lacks symmetry inside the vehicle. Consequently, it was imperative to collect data from each seat individually for machine learning. Furthermore, when the first row is occupied, multipath reflections may create false targets in the second row.

There are some factors for sensor selection in occupancy detection by radars inside a vehicle. One of the most important factors is frequency selection. Most in-cabin sensing investigations by radar for occupancy detection have used millimeter wave radar (60 GHz and over). As we discussed earlier, millimeter wave radar has several benefits over centimeter wave radars and low carrier frequency radars. Regarding sensor placement, because the radar should be placed under the car roof in occupancy detection applications, the dimensions of the radar package are less important in comparison to vital sign monitoring applications. For more information, refer to Appendix D.

2.1.3 Gesture Recognition to Assist Drivers.

Potential distracting factors for drivers have increased due to crowded roads in addition to the enhanced infotainment functionality and vehicle's ability to interact with its driver. Visual, cognitive, physical, and auditory factors are among the main causes of driving distraction. Visual and physical distractions, when combined, have the biggest impact on driving performance [116]. Researchers have conducted extensive studies to address the aforementioned issues. Non-contact human-computer interaction has been proposed and developed recently, and the topic of contactless human-computer interaction using hand-based gesture recognition has been extensively explored recently.

Several sensors can be employed in hand-based gesture recognition. Camera-based sensors raise privacy concerns and have high computing costs due to considerable signal processing, and are sensitive to changes in background color, and light intensity [167], [168]. In very dim light conditions, the accuracy rate decreases by 30% [169][117]. IR sensors can also be employed to detect hand gestures inside the vehicle. However, they do not preserve privacy and are sensitive to illumination levels [170]. Depth-based sensors are excellent at sensing location changes, but they are unable to identify hand forms or orientations [171]. Wearable technology restricts system input to the person who is wearing the device [116]. Alternatively, radars can identify particular hand and finger movements and are unaffected by illumination variations while effectively ensuring in-cabin privacy [121]. Recent radar-based gesture recognition investigations

have relied on micro-doppler signatures. These investigations employed either range-doppler [116], [117] or time-frequency [115], [118], [119], [120], [121], [122].

Despite the benefits of radars, the fundamental issue with radar-based gesture detection systems is their dependence on distance and direction [121]. In [121], the time of arrival information has been fed to a learning approach to address this issue, while in [115], different angles and ranges have been examined. The maximum tilt from the perpendicular angle and maximum range to have reliable results are 15 degrees and 100 centimeters, respectively.

The choice of a particular radar system has a direct impact on the efficiency of radar for hand-based gesture recognition. For example, the number of receivers in the radar system determines the angular resolution of the radar. More receiver channels will result in better angular resolution. In [70], [78], [79], the authors could use more channels to have better angular resolution and reliable results. However, they have employed a radar sensor with only one receiver to collect data. By one receiver, the FMCW radar cannot discriminate targets located in the same range, even at different angles accurately [124]. Another important parameter is the carrier frequency. Recent papers have mostly used mm-wave radar to achieve accurate detections. Higher frequencies are more sensitive to small radar cross-section changes and would have better results [115]. The range resolution of radar is also one of the key factors since better range resolution will result in better discrimination [143]. For more information, refer to Appendix D.

2.2 Important Case Studies for Vital Sign Monitoring

Vital sign monitoring is the most important case study for in-cabin monitoring by radar. Monitoring a driver's vital signs can alert them to stress or drowsiness, reducing the risk of accidents. Another addressed issue by vital sign monitoring is left-behind child detection. The breathing monitoring of passengers can be used to avoid these problems[25].

Table B.1 compares different recent works according to their setup for in-cabin radar applications to monitor vital signs. These studies are compared based on the following criteria: sensor placement, frequencies, ground truth data, and radar brand or package size. As is apparent from the table, the rearview mirror is the most common location in which to attach the radar in recent studies. In [43], there is also a deep investigation into sensor placement. The findings indicate that the rearview mirror is identified as the optimal location for monitoring the driver's BR, as shown in Figure 2.2.

Frequency selection is also a crucial task in achieving accurate BR and HR estimations. One of the most significant factors in frequency selection is body surface reflection. Less penetration can provide more

accurate vital sign monitoring by radar. In [43], [168], it was demonstrated that higher frequencies can penetrate less into the human body. Various experiments were conducted, demonstrating that body motion at higher frequencies has a greater impact on signal reflection than changes in skin surface impedance [133].

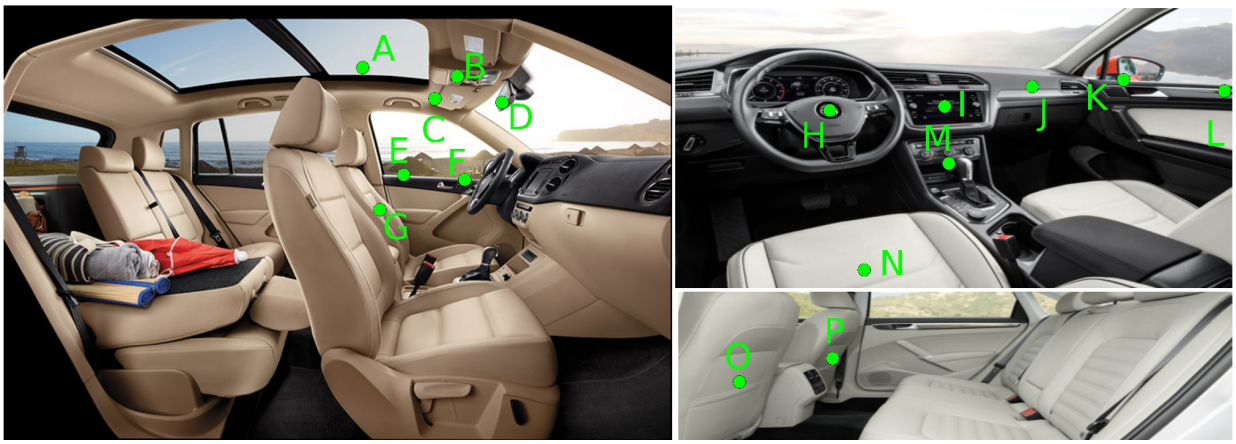

Figure 2.2: Different radar placements inside a vehicle for driver BR estimation [43]. The rear-view mirror (D) has the best results.

Additionally, the higher the carrier frequency, the higher the sensitivity of radar on small movements [135]. Hence, radar can estimate human body vibration accurately. However, phase wrapping is more possible in higher frequencies, resulting in a more complicated signal processing chain. When the phase of the slow-time signal exceeds the phase range ($-\pi$, π), phase wrapping occurs. Since the chest wall displacement can reach 12 mm and the wavelength of the most commonly used carrier frequency, 60 GHz, is almost 5 mm, this problem can occur frequently [124].

Figure 2.3 illustrates the distribution of recent studies on frequency selection for vital sign monitoring inside vehicles using radar, indexed on Google Scholar over the years. Recent studies have predominantly utilized mm-wave radar, specifically frequencies of 60 GHz and higher, for monitoring vital signs inside vehicles. It is noteworthy that the Federal Communications Commission (FCC) currently prioritizes the 60 GHz band for use in health applications [172].

Another critical factor in sensor selection is package size. The compact dimensions of radar systems for in-cabin applications are crucial due to limited space within vehicles. Hardware integration plays a significant role in reducing package dimensions. Higher carrier frequencies enable the creation of smaller devices and circuit components, facilitating hardware integration [173]. Recent studies have utilized small-package radar systems with dimensions less than 50×70 mm[20].

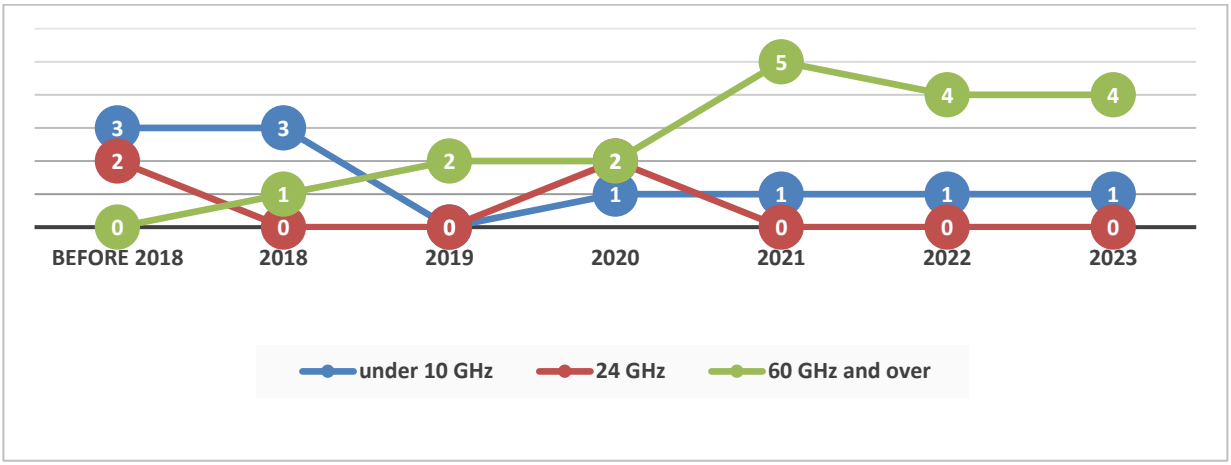

Figure 2.3: Distribution of recent studies in frequency selection for vital sign monitoring inside a vehicle by radar over the years.

There are several considerations to bear in mind when aiming to enhance vital sign monitoring accuracy. These include the signal processing chain, cancellation of human body motion and vehicle vibration, clutter removal, multipath removal, beam steering, phase unwrapping, and harmonic analysis. Table 2-1 compares various published papers on in-cabin vital sign monitoring, focusing on their signal processing chains.

To improve the quality of vital sign signals inside a vehicle, random human body cancellation has been studied [25], [45], [57]. A slow-time envelope modulation results from the breathing-related vibrations of the chest and the random human body motion. The breathing signal can be filtered to prevent significant frequency interferences, but if there are a lot of random human body motions, the interferences will appear in the breathing frequency range. Intermodulation distortions can also occur in this frequency range [174]. In [57], the driver's motions are calculated from the Doppler-time map and used to develop a signal distortion compensation. This measure helps to remove the signal distortion that the driver's motions make while driving. In recent studies, the human body motion, whether by simple filtering [43], [112] or a specific filter design [25], [45], [47], [54], [55], [57], cannot be removed reliably when the human body motion is within the breathing spectrum which is less than 0.5 Hz [175]. In [176], the use of a camera system combined with a microwave sensor has been investigated to develop an approach for canceling random body movements. The phase shift in the radar sensor was compensated for using the random body motions captured by the camera.

The main cause of car body vibrations in a moving vehicle is the changes in the road surface. Depending on the type of vehicle, the power spectrum density has a significant amount of content in the range between

1 Hz and 100 Hz [177]. A mathematical framework was proposed in [54], [55] whereby an accelerometer was attached to a radar-based sensor, allowing for the recording of acceleration. By reconstructing the movement of the seat and the passenger using this data, the corresponding Doppler was calculated. The signal received by radar was then denoised using the Doppler, which resulted from the unwanted vibrational motion.

The clutter Inside a vehicle reflects signals similar to those of a human, but it remains stationary over time. Therefore, clutter cancellation for ultra-wideband (UWB) radars is crucial as these radars measure human body displacements based on the amplitude of signals. Strong clutter reflections can affect human body displacements in UWB signals. Clutters are typically suppressed using filtering techniques such as motion filter [14], IIR moving average filter [47], [178], and Pseudo-Bi-Dimensional Ensemble Empirical-Mode Decomposition [34].

Due to the confined space inside a vehicle, there are multipath signals. This issue is rarely addressed because most studies focus on the vital sign monitoring of drivers. As radars can be installed close to the driver, the multipath effect is insignificant. Few studies on multiple target monitoring have mentioned this issue. In [53], the correlation coefficients between obtained vital signals in various locations are analyzed to choose the corresponding vital signs. In [179], the proposed method was able to distinguish the respiration signals of five participants seated close to one another [53]. In this approach, each seat has a specific distance from the radar, which is different from other seats. Hence, the radar should not be placed on the line of symmetry of the car. In [43], the authors conducted extensive research on sensor placement to improve the accuracy of vital sign monitoring for a driver.

HR estimation by radar suffers from multiple challenges. The most important one is the higher harmonics of breathing vibrations. This issue becomes prevalent as this indicator interferes with the heartbeat signal. One solution to recognize HR from higher harmonics of breathing is harmonic analysis. It is based on the pulse train theory [135]. Estimating HR without harmonic analysis produces inaccurate and unreliable results because breathing harmonics can have stronger amplitudes than the HR peak in the frequency domain [135]. It has also been demonstrated that the heart vibrations in the frequency domain can be between two sequential harmonics of breathing vibration and have less amplitude. This creates difficulty in HR estimation. Some studies have used simple filtering to remove breathing harmonics [44], [45], [47], [48], [52], [53], [112], [160], [180].

Some studies developed approaches to detecting abnormal breathing. In [175], the human vibration signal has been filtered up to 0.5 Hz, or 30 breaths per minute, to estimate the breathing signal. This indicates that

the estimation technique only considers the primary peak. As a result, higher frequency information is omitted in the reconstructed breathing signal after filtering, and the breathing signal resulting from abnormal breathing with sharp peaks will be smoothed. Consequently, this adds a level of complexity to the detection of abnormal breathing.

The suppression of breathing vibrations, in service of garnering accurate HR estimation, has been studied extensively. In [173], the authors employed ensemble empirical mode decomposition (EEMD) and principal component analysis (PCA) to reduce the effect of breathing vibrations on heart vibrations. An iterative notch filter has also been employed to suppress breathing harmonics [135], [181].

Table 2-1: Comparison between the different in-cabin published papers for vital sign monitoring in the signal processing chain.

Reference	HBMC[1]	VVC[2]	Clutter removal	Multipath removal	Beam steering	Phase unwrapping	Harmonic analysis	Estimation method
[25]	Yes	Yes	Yes	No	No	No	No	PFTV[3]
[34]	Yes	No	Yes	No	No	No	No	PFTV
[43]	Yes	Yes	Yes	No	No	No	No	PFTV
[53]	No	No	Yes	Yes	No	No	No	Correlation coefficients
[52]	No	No	Yes	No	No	Yes	No	PFTV
[47]	Yes	No	Yes	No	No	No	No	PFTV
[20]	No	No	Yes	No	No	No	No	PCTD[4]
[48]	No	No	Yes	No	No	No	No	PCTD
[57]	Yes	No	Yes	No	No	No	No	PFTV
[45]	Yes	Yes	Yes	No	Yes	Yes	No	PFTV
[54], [55]	Yes	Yes	Yes	No	Yes	No	No	PFTV
[44]	No	No	Yes	No	Yes	No	No	PCTD
[51]	No	No	Yes	No	No	No	No	PFTV
[112]	Yes	No	Yes	No	No	No	No	PFTV

[1] Human body motion cancellation
[2] Vehicle vibration cancellation
[3] Peak of FFT of target's vibration
[4] Peak counting in the time domain

The fast Fourier transform (FFT) and continuous wavelet transform (CWT) are regarded as highly fundamental techniques for obtaining the BR [182], [183], [184], [185], [186], [187], [188], [189], [190]. With respect to the peak of the spectrum in a certain frequency band, these techniques can estimate the BR. For vital sign monitoring inside a vehicle, the most common estimation technique is the peak of the FFT of the target's vibration. The HR can also be estimated from its peak after taking FFT [133]. As discussed before, due to the presence of breathing harmonics close to the HR peak and other interferers, harmonic analysis is required for in-cabin applications [135]. Other estimation techniques, like the maximum likelihood estimator (MLE), can be employed to estimate BR [191]. Cyclostationary analysis is another method to improve the radar sensor's ability to detect vital signs [187], [192].

Another potential application of radar technology is in the estimation of heart waveforms to detect heart conditions. Despite operating at millimeter wavelengths with limited skin penetration [43], FMCW radar systems are capable of detecting skin movements caused by heartbeats. By correlating these movements with the ECG signal, which associates specific heart motions with P, Q, R, S, and T waves, it becomes feasible to leverage cardiological insights in conjunction with radar sensors. However, recent studies have predominantly focused on HR estimations rather than exploring the broader potential of radar technology in analyzing heart waveforms [133], [134], [135], [136], [137].

Recently, several studies have delved into the estimation of heart waveforms using radar signals, which can be instrumental in HR and HRV estimation. Some of these investigations have employed neural networks and machine learning techniques to derive ECG patterns from radar data [131], [193], [194], [195], [196], [197], [198], [199]. However, these methodologies are trained on data from individuals without cardiovascular conditions.

Prolonged QTc intervals have been identified as a risk factor contributing to sudden cardiac deaths in the general population. The QT interval on an ECG measures the time from the beginning of the Q wave to the end of the T wave. This duration represents the full cycle of electrical activity during ventricular contraction and relaxation in the heart [200]. Therefore, monitoring individuals with this heart condition becomes increasingly valuable. Recent studies mostly investigated their algorithms in healthy subjects for HR and HRV estimation [149], [150], [151], [152], [155], [156], [193], [194], [195], [201]. However, individuals with prolonged QTc may exhibit normal HR and HRV levels [200].

Table 2-2 compares in-cabin published papers for vital sign monitoring across four important factors, including the selected vital signs, accuracy or advantages, limitations, and the number of subjects. The results of different papers demonstrated that up to two breaths error was acceptable.

Table 2-2: Comparison between the different in-cabin published papers for vital sign monitoring based on four important factors, namely, the selected vital signs, accuracy or advantages, limitations, and the number of subjects.

Reference	The vital sign	Accuracy or advantages	Limitations	Number of subjects being monitored simultaneously
[16]	BR	• A metasurface lens antenna is designed to accurately steer beams towards human targets while considering their relative positions within the vehicle. • The proposed tags exhibit both retroreflection and polarization selection characteristics to mitigate the impact of strong clutter and multipath reflections in the in-vehicle environment.	• Lack of accuracy analysis • Improper frequency selection • Lack of addressing body movement and vehicle vibrations in the signal processing chain.	2
[79]	BR	• The maximum BR error: ±2 breaths • Proposing two applications, including occupancy detection and BR estimation • In-cabin measurements and considering real situations like Including a car seat for infants	• The accuracy of the amplitude approach in UWB radars is dependent on the range since amplitude drops by range to the power of four based on the radar equation.	1
[43]	BR	• Maximum BR error: ±2 breaths • A deep investigation of sensor placement in 16 radar positions • Decent research on frequency selection based on reflected power from human skin. • Two different signal processing approaches for online and offline analysis	• Lack of real-time processing	1

		• Investigate the impact of the time window length on BR estimation		
[53]	BR and HR	• The HR error: 12.5%, Multiple targets. • Proposes a location-based Variational Mode Decomposition to identify the vital signs of different subjects. • Background removal by filtering	• Harmonic analysis might be applied to increase the accuracy of HR estimations.	2
[52]	BR and HR	• The BR and HR errors: 7% and 5% respectively. • Multi-subject vital sign monitoring • Using w-band for automotive radars	• Lack of practical measures within the vehicle • The accuracy of the amplitude approach in UWB radars is dependent on the range since amplitude drops by range to the power of four based on the radar equation. • Harmonic analysis might be applied to increase HR estimations.	2
[47]	BR and HR	• The maximum BR and HR error: ±1.2 breaths and ±2.5 beats. • Identifying the key factors that cause car crashes, such as distracted driving and phone use. • Proposing an accurate fitting approach using the R-square value	• Harmonic analysis might be applied to increase HR estimations	1
[20]	BR	• The maximum BR error: ±1 breath • Accuracy of drowsiness detection: 87% • Comparing various machine learning classifiers	• Lack of collected data in real driving environments	1
[48]	BR and HR	• The accuracy of drowsiness: 71% • A significant amount of collected data	• Harmonic analysis might be applied to increase HR estimations. • Estimating breathing signals without appropriate ground truth • Insufficient diversity among volunteers	1

[57]	BR	• The maximum BR error: ±2.96 breaths • Adaptive driver's movement compensation by a motion quantification index	• Lack of collected data in real driving environments. • Phase wrapping issue for high chest wall displacement	1
[45]	BR and HR	• The median BR and HR error: 0.16 breaths and 0.82 beats, respectively.	• Phase wrapping issue for high chest wall displacement	1
[44]	BR and HR	• The maximum HR error: ±2 beats • A novel driver's motion compensation • Investigate the impact of the window length on HRV. • Examine the effects of many factors, such as the device locations, the pavement conditions, and the motion types	• No harmonic analysis to estimate HR	1
[30]	HR	• The maximum HR error: ±4 beats • A comprehensive study of processing window size	• Harmonic analysis might be applied to increase HR estimations. • No ground truth for the BR • The HR is assumed to be 60 to 120. But it could be more than 120 [72].	
[51]	BR and HR	• Anger prediction accuracy: 92.83% • Unique hardware design for online monitoring of driver • Collecting data from 100 people • PCA to feature selection	• Lack of diversity in collected data (data collected based on only two states, such as the calm state and the angry state)	1
[112]	BR and HR	• Age classification accuracy: 96.25% • Collecting a valuable database	• Lack of collected data in real driving environments	1

Chapter 3
Multi-Bin Breathing Pattern Estimation by Radar Fusion for Enhanced Driver Monitoring

Monitoring the status of the driver is a crucial aspect of health monitoring inside vehicles as it helps to identify potential health or safety risks that could affect a driver's ability to operate a vehicle safely. This includes monitoring for fatigue, distraction, or impairment, among other things, which can potentially cause car crashes. Among many possible radar configurations, mm-wave FMCW radars can accurately detect range and monitor displacements that are essential in breathing pattern monitoring. Breathing pattern monitoring is one of the key signatures of the driver's health. An accurate estimation of the breathing pattern enables the detection of breathing abnormalities, including Tachypnea, Bradypnea, Biot, Cheyne–stokes, and Apnea. The breathing pattern can be estimated from both the chest and abdomen. For this purpose, two 60 GHz FMCW radars are employed in this study. The proposed algorithm is capable of detecting the mentioned breathing abnormalities through BR estimation and breath-hold period detection. In addition, the proposed method in this thesis estimates BR based on the multiple range bins. To determine the accurate number of range bins for BR estimation, a study on the human radar geometry problem inside a vehicle is conducted. In this chapter, the details of multi-bin breathing pattern monitoring by a dual radar system inside the vehicle are discussed.

3.1 Relevance

Estimating breathing patterns by mm-wave FMCW radars encounter some challenges for in-cabin applications. Firstly, breathing patterns can be estimated from the chest and abdomen displacements. However, due to the low amplitude of chest wall displacements during abdominal breathing, both the chest and abdomen should be monitored by a dual radar to prevent false detections. Nevertheless, recent in-cabin investigations employed a single radar for estimating breathing patterns [202].

Secondly, due to the confined space inside a vehicle, the passengers' reflections can interfere with the driver's reflections. These interferer reflections pose a challenge in the detection of abnormal breathing patterns that involve a breath-hold period [25]. Since the driver is non-vibrant during a breath-hold period, an interfering reflection from a vibrant passenger can be misinterpreted as a driver's reflection.

Thirdly, normal driving activities like turning the wheel around and shoulder checking can distort the breathing pattern even when they are not periodic [57]. Some of the studies employed an expensive and intricate system to mitigate the effect of these movements [145], [146]. These studies used a less practical

package size for this purpose, which adds discomfort for the drivers. Off-the-shelf mm-wave radars offer a compact size radar that is capable of sweeping a high-frequency bandwidth. Consequently, this high-frequency bandwidth leads to improved range resolution [141], [142], [143], [144]. As the human body captures more than one range bin in these radars inside the vehicle, multiple range bins can be used for breathing pattern estimation. The proposed multi-bin approach estimates breathing patterns from different human body parts, which can be used for body motion detection.

3.2 Multi-bin BR Estimation

In this chapter, the proposed signal processing chain for BR estimation is presented and compared with the conventional one. The main idea behind the proposed method came from the capability of radar to produce a high-range resolution signal caused by high-frequency bandwidth.

FMCW radar divides the range into smaller units by range resolution. Each unit is called a bin. The human body in front of a high-range resolution radar captures more than one range bin, especially when a human is close to the radar. In the proposed method, several range bins around the main range bin of the target are employed to have accurate estimations. If the radar is in front of the subject's chest, the main range bin is the range of the middle of the chest from the radar, which is the closest part of the body to the radar. Other organs of the human body capture further range bins. If the estimated BR from one of the range bins is incorrect, it may be removed from estimations by outlier removal in the final step. This wrong estimation can be caused by random body movement, noise, and the absence of a fully recovered wrapped phase. As a result, this multi-bin approach addresses these issues. Another multi-bin approach is also explored in [45], where the multiple bins are selected from the rang-azimuth map. However, in this thesis, due to the limitations of the selected off-the-shelf radar, which lacks high azimuth resolution, only range bins are utilized for breathing pattern estimation. High azimuth resolution radars, such as the TI cascade radar [203], are not cost-effective due to their requirement for multiple receivers.

The rest of this section discusses the analog and digital signal processing chains for breathing pattern estimation by dual radar.

3.2.1 Signal Processing Chain Before ADC

Figure 3.1 shows a simplified homodyne block diagram of the FMCW radar prior to the ADC [133]. The receiver amplifies received signals from objects in the environment. These reflected signals are influenced by the properties of the objects, like range and radar cross-section. Then, a mixer correlates the transmitted and received signals. This mixer produces both low-frequency and high-frequency components. A low-pass

filter is applied to select the low-frequency components in the next step. Finally, an ADC converts analog signals to discrete signals.

This study uses the BGT60TR13C FMCW radar from Infineon Technologies. This sensor can generate an FMCW signal from 58 GHz to 63.5 GHz modulated by the sawtooth wave. The employed analog-to-digital converter (ADC) has a 12-bit resolution, providing a 74 dB dynamic range, and its sampling rate can reach up to 4 Mega samples per second [204].

3

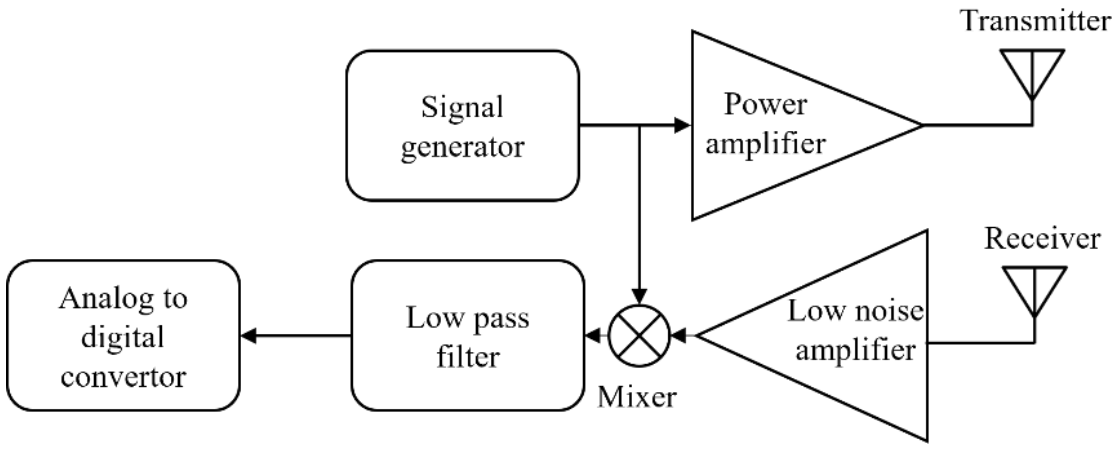

Figure 3.1: The simple block diagram of an FMCW radar before ADC.

3.2.2 Geometry of Multi-bin BR Estimation

The human body in front of a high-range resolution radar captures more than one range bin, especially when it is close to the radar [45]. Therefore, several range bins around the main range bin of the target can be employed to improve breathing pattern estimation accuracy. If the radar is in front of the subject's chest, the main range bin is the range of the middle of the chest from the radar, which is the closest part of the body to the radar. Other organs of the human body capture additional range bins. If the estimated BR from one of the range bins is incorrect due to the random body movement and noise, it can be removed from estimations.

Figure 3.2 represents a radar in front of the subject's chest. The farthest part of the human body which is influenced by lung movements in the chest radar, is the shoulder. Assuming that the radar is positioned at r_1 from the middle of the chest and that the distance from the middle of the chest to the shoulder is b_1, the Pythagorean theorem can be used to calculate the distance between the radar and the shoulder as follows:

$$R_1 = \sqrt{r_1^2 + b_1^2}. \tag{3.1}$$

The human body captures the radar range profile from r_1 to R_1. Consequently, the number of range bins that can be employed for breathing pattern estimation is as follows:

$$n = \left\lceil \frac{R_1 - r_1}{\Delta R} \right\rceil, \tag{3.2}$$

where ΔR is the range resolution of radar and $\lceil . \rceil$ is the sign of the ceiling function. Assuming that r_1, b_1, and ΔR are 20 cm, 26 cm, and 3 cm, respectively, n equals 4.

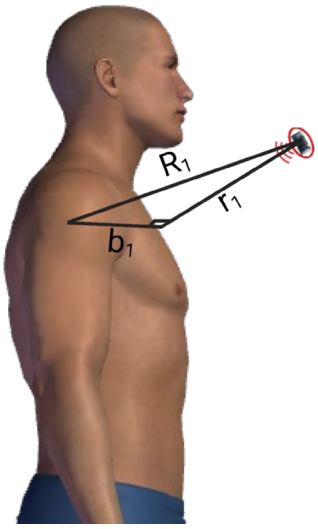

Figure 3.2: Chest radar geometry for multi-bin approach.

3.2.3 Dual Radar Placement

Abdominal breathing causes low chest wall displacement, which can lead to false estimations of the breath-hold period. Therefore, abdomen and chest displacements should be monitored separately by two distinct radars to eliminate these false detections. Figure **3.3** displays dual radar placement in front of the chest and abdomen to separate them based on the covered area. The a_1 and a_2 spots should not overlap to accomplish this separation. As a result, the inequality between a_1, a_2, and torso length is given by:

$$a_1 + a_2 > H, \tag{3.3}$$

where H is the human torso length. The torso length is greater than 40 cm for adults [205]. Then, a_1 and a_2 can be calculated as follows:

$$a_1 = r_1 \cdot \tan\left(\frac{\theta}{2}\right), \tag{3.4}$$

$$a_2 = r_2 \cdot \tan\left(\frac{\theta}{2}\right),$$

where θ is half power beamwidth in the H-plane (HPBW-H) of the antenna. The HPBW-H of BGT60TR13C is 35° [141]. The chest radar distance from the middle of the chest (r_1 in Figure **3.3**) is 20 cm, and the abdominal radar distance from the abdomen (r_2 in Figure 3.3) is 40 cm. a_1 and a_2 are 6.4 and 12.8 cm based on (4), respectively. The summation of a_1 and a_2 is less than the torso length. Therefore, this design satisfies (3), and the chest radar and abdominal radar are separated based on the covered area. Nevertheless, since both radars are at the same frequency and close together, cross-interference appears in their receivers if they operate simultaneously.

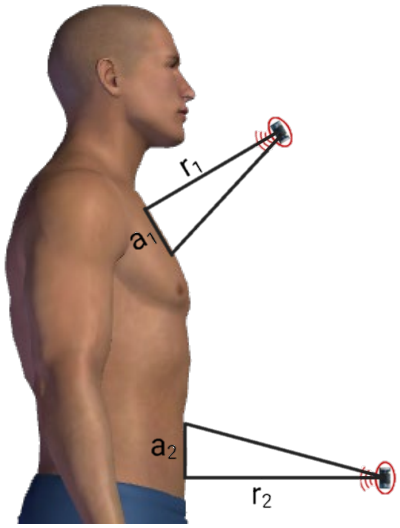

Figure 3.3: Dual radar placement in front of chest and abdomen.

3.2.4 Dual Radar Signal Design

There are two approaches to fusing two FMCW radars. The first approach involves selecting separate carrier frequencies without frequency overlap. Since the employed radars are identical, the operational frequency bandwidth can be divided between them. However, the drawback of this division is the loss of range resolution by at least 50%. The second approach entails applying time division multiplexing, where

one radar is switched off while the other is switched on, and vice versa. However, this approach introduces a time delay between the radars, which should be minimized as the goal is to use both radars to make decisions. Therefore, by calculating and minimizing the time delay in the system, both radars can benefit from high-range resolution signals without interference.

Both pulse repetition frequency (PRF) and pulse duration should be considered to calculate the minimum delay between radars. The maximum frequency of breathing is almost 0.6 Hz [124]. Hence, the sampling frequency should be greater than 1.2 Hz based on the Nyquist theorem. Because only one chirp signal, which is the average of all received chirps, is employed from each pulse, the sampling of the breathing vibration is equal to pulse repetition frequency. As a result, the pulse repetition frequency should be greater than 1.2 Hz. Higher PRF provides more samples from breathing vibration, which enhances breathing pattern estimation and can be beneficial in phase unwrapping [133]. However, higher PRF reduces inter-pulse repetition time, and the hardware should be able to generate that PRF. Because two radars are employed in this study, the inter-pulse repetition should be longer than the pulse duration. The pulse repetition frequency is set to 20 in this thesis.

The pulse duration can be determined according to several parameters of the target. The first parameter is the range resolution as follows:

$$\Delta R = \frac{c}{2B}, \tag{3.5}$$

where c is the light velocity in free space, and B is frequency bandwidth [144]. The maximum frequency bandwidth should be employed to have accurate results. The maximum frequency bandwidth of BGT60TR13C is almost 5 GHz [141] which results in a 3 cm range resolution. Another parameter to determine chirp time is the number of samples per chirp, which depends on the maximum range and range resolution as follows:

$$N = \frac{2.R_{max}}{\Delta R}. \tag{3.6}$$

R_{max} is the maximum range of the target (96 cm in this thesis). The linear chirp slope is defined as follows:

$$k = \frac{B}{T}, \tag{3.7}$$

where T is active chirp time. In this thesis, the chirp slope is set to 78.128 MHz/μs, with 64 samples per chirp. Hence, the ADC sample rate is 1 MHz, and the active chirp time is 64 μs. Because breathing is a slow activity, the reflected chirps in a pulse are very similar to each other. Eight chirps for each pulse are considered. The minimum delay between radars based on all the discussed parameters is as follows:

$$\tau_{min} = N_c.\left(\frac{2.R_{max}}{\Delta R.f_s} + T_{idle}\right), \tag{3.8}$$

where N_c is the number of chirps per pulse, f_s is the ADC sample rate, and T_{idle} is the idle time. The minimum delay based on (3.8) is 0.552 ms with an inter-pulse repetition time of 49.5 ms. Table 3-1 summarizes the designed signal parameters to achieve minimum delay. In conclusion, fusing multiple radars can achieve finer range resolution without interference by designing a tailored signal. This provides significant benefits in precision-critical applications such as remote sensing and target tracking. However, optimization is crucial for optimal performance.

Table 3-1: Designed signal parameters.

Parameter	Value
PRF	20 Hz
B	5 GHz
ΔR	3 cm
R_{max}	96 cm
N	64
f_s	1 MHz
chirp slope	78.128 MHz/μs
T_{idle}	5 μs

3.2.5 Signal Processing Chain After ADC

The FMCW radar is capable of generating periodic signals to scan the surrounding environment. In doing so, the radar produces a chirp signal that sweeps from a low frequency to a high frequency. A group of chirps generated periodically with an idle time between two sequential chirps is called a frame. The radar

sensor can generate several frames per second. As a result, the received signals transmitted back from the environment are three-dimensional, comprising information on range, slow time, and frame.

Figure 4.1 depicts the conventional and proposed signal processing chains after ADC. First, the DC value of the signal needs to be removed; otherwise, the phase quality is affected [133]. Second, the first FFT, which is called fast-time FFT, is applied to a chirp signal to generate a range profile map. The range profile map is discretized by the range resolution of the FMCW radar. Then, a 3D cube of chirps is reconstructed, and all the information captured is in different ranges.

In the proposed method for multiple range bin BR estimation, four range bins, including the main range bin and those around it, are employed to ensure accurate estimations in the chest radar. The reflected signal from the middle of the chest, which is the first reflection in the chest radar, may appear one range bin before the detected peak. Other organs of the human body capture further range bins. To avoid unnecessary computations for empty range bins, The range bins captured by the human body can be determined.

After fast time FFT or range FFT, the range of the target can be determined to avoid unnecessary computations. In [133], the range bin of the target was selected after phase unwrapping and vibration FFT. These calculations are unnecessary since a target captures few range bins in a fast time signal. As a result, it is not necessary to monitor all the range bins.

A robust novel algorithm is presented in this thesis to detect the main range bin of the target. First, clutter cancellation is applied to remove zero-doppler reflections [133]. Since the human body is generally less dynamic, clutter cancellation is applied to the chirps across frames in a processing window. If the clutter cancellation was applied through the slow time on the chirps in a frame, the target's signals would be suppressed since the time difference between the chirps within a frame is small.

Finally, outlier removal is applied to the detected main range bins from multiple chirps. In terms of outlier removal, if an estimated range bin falls outside the following interval, it is considered an outlier.

$$\left(\overline{R} - \sigma_R , \overline{R} + \sigma_R\right), \tag{3.9}$$

where $\overline{R}$ is the mean of all detected range bins and σ_R is their standard deviation. After removing outliers, the mean of all range bins after outlier removal is selected as the main range bin of the target for breathing pattern estimation.

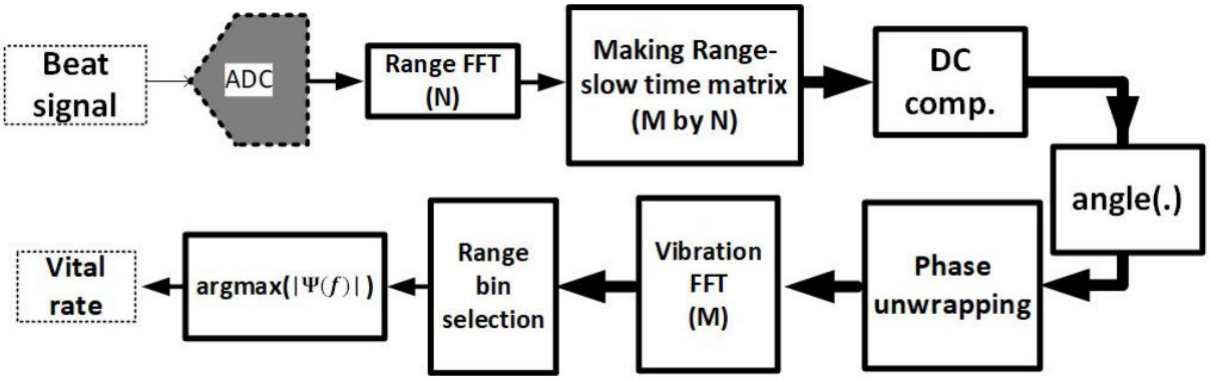

(a)

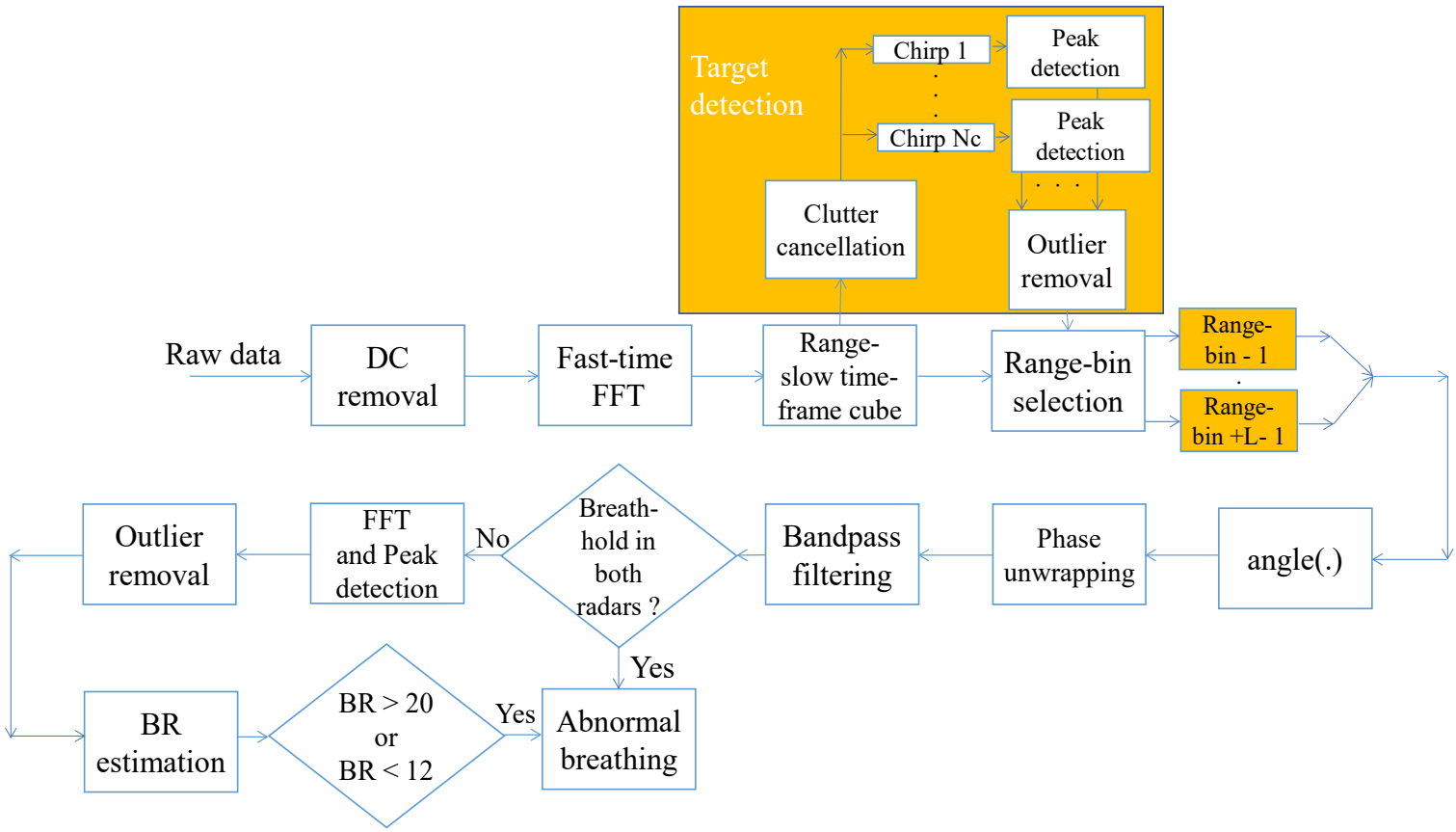

(b)

Figure 3.4: The signal processing chains after ADC (a) the conventional signal processing chain [133] and (b) the proposed signal processing chain.

The breathing pattern, which corresponds to displacement, is the phase of the beat signal in a specific range bin. The phase can wrap when the displacements are large. If the target's phase changes between -π

and +π, there is no phase wrapping. Phase wrapping occurs when the target's displacement exceeds half of the wavelength. It can be calculated using the following formula:

$$-\pi < \frac{4\pi}{\lambda}(R_0 + R(t)) < \pi \Rightarrow -\frac{\lambda}{4} - R_0 < R(t) < \frac{\lambda}{4} - R_0 \Rightarrow \Delta R_{min} = \frac{\lambda}{2}. \quad (3.10)$$

Since a human's chest wall displacement can reach 12 mm [124], the phase wrapping can usually occur at 60 GHz.

The obtained signal after phase unwrapping is called the vibration signal, which contains all the vibrations in the selected range bin. The constant range of the target adds a constant phase in the breathing signal, which can be removed by mean subtraction. The breathing signal can be achieved by canceling undesired vibrations like heartbeat and random body motion. A 4^{th}-order Butterworth bandpass filter with cutoff frequencies of 0.1 Hz to 0.7 Hz is applied to remove the unwanted vibrations in this thesis. The detected peak from the FFT of the breathing signal determines the BR.

The amplitude of the displacement is a criterion that can determine if there is a breath hold. The bandpass filter suppresses vibrations outside of the desired band in the vibration signal. Therefore, the estimated frequency by peak detection is often in the breathing frequency band. Since peak detection determines a peak in the breathing band in the frequency domain, there is a detected peak even when the input signal is noise. As a result, the amplitude of this detected peak should be compared with a threshold. This threshold discriminates between breathing periods and breath-hold periods.

The threshold level determination needs to be done statistically by collecting data from different participants. These participants were asked to hold their breath while there were no other body movements. The amplitude of the detected peak from the filtered vibration signal obtained for 20 seconds is considered indicative of a breath-hold period. Approximately 300 measurements were collected from each of the 8 participants to estimate statistical parameters.

Since the amplitude of the detected peak in a breath-hold scenario is non-negative, its distribution is log-normal [206]. The mean and standard deviation of data on a millimeter scale after taking natural logarithm are -4.6 and 0.9, respectively. The threshold level can be determined using the empirical rule. Since missing a breath-hold period has more cost than having some false detections, the threshold level should be higher than almost all the amplitudes. According to the empirical rule, 99.7% of the amplitudes fall within three standard deviations of the mean [207]. The threshold based on the three-sigma rule of thumb is -1.89, which is approximately equivalent to 0.15 after applying the exponential function to the mean log-normal value.

Therefore, if the amplitude of the detected peak is less than 0.15 millimeters, this period is considered a breath-hold.

The estimated BRs from multiple range bins are compared with each other to determine an accurate estimation in the next step. An outlier removal, which can remove the corrupted range bin by random body motions is applied to the estimated BRs. Finally, the mean of all the remaining estimations determines the BR. If the estimated BR is below 12 bpm or above 20 bpm, the breathing patterns are classified as abnormal according to predefined thresholds. For further discussion, refer to Appendix G.

3.3 Experiments

The experimental setup, experimental protocols, and the abnormal breathing algorithm are discussed in this section.

3.3.1 Experimental Setup

The sensor selection is based on two factors, including the carrier frequency and the size of the radar's package. First, higher carrier frequencies have a better signal-to-noise ratio (SNR) due to the noise power reduction by increasing the carrier frequency. The FCC also supports the 60 GHz band to be used in in-cabin applications [172]. As a result, the 60 GHz band is selected for proof-of-concept. Second, BGT60TR13C from Infineon is employed in this thesis. The dimensions of the whole package of this radar are 64 mm x 25.4 mm [141]. Due to its compact dimensions, it can be placed inside the vehicle without causing discomfort to drivers.

The sensor placement has a direct effect on the measured displacements by radar. Three factors should be considered, including the angle between the radar and the human body, the distance between the radar and the human body, and signal blockage by other objects inside the vehicle. First, if the radar is placed in front of the displacement, it can estimate displacement accurately since the radar measures radial displacements. A displacement with a high amplitude may be less affected by noise. Second, the reflected power in the radar equation is related to distance by a power of four. Therefore, radar measurement can be less affected by noise at low distances. Third, if a portion of radar signals, before reflecting from the human body, is blocked by objects, especially metallic ones, the SNR of the signal from the human body decreases over a longer range. As a result, a radar placed in front of the displacement at the closest range without being blocked by any objects can estimate displacements more accurately.

Figure 3.5 depicts the displacements of the chest and abdomen walls of a sitting human while breathing in and out. Due to the angle between chest displacements and the horizontal axis, the chest radar should be

attached to the ceiling while tilted toward the chest. This area is almost unused inside the vehicle. However, the abdomen radar cannot be placed properly since the best placement is under the wheel, which can block most radiated signals. Figure 3.6(a) shows the chest and abdomen radar placements in this thesis. The abdomen radar is tilted toward the middle of the abdomen as can be seen in Figure 3.6(b). The distance between the chest radar and the central point of the chest equates to approximately 20 centimeters, while the distance between the abdominal radar and the midpoint of the abdomen measures approximately 40 centimeters. The chest radar is affixed to the ceiling via adhesive tape, while the abdominal radar is securely fastened to a holder, allowing for adjustable angulation towards the abdominal center.

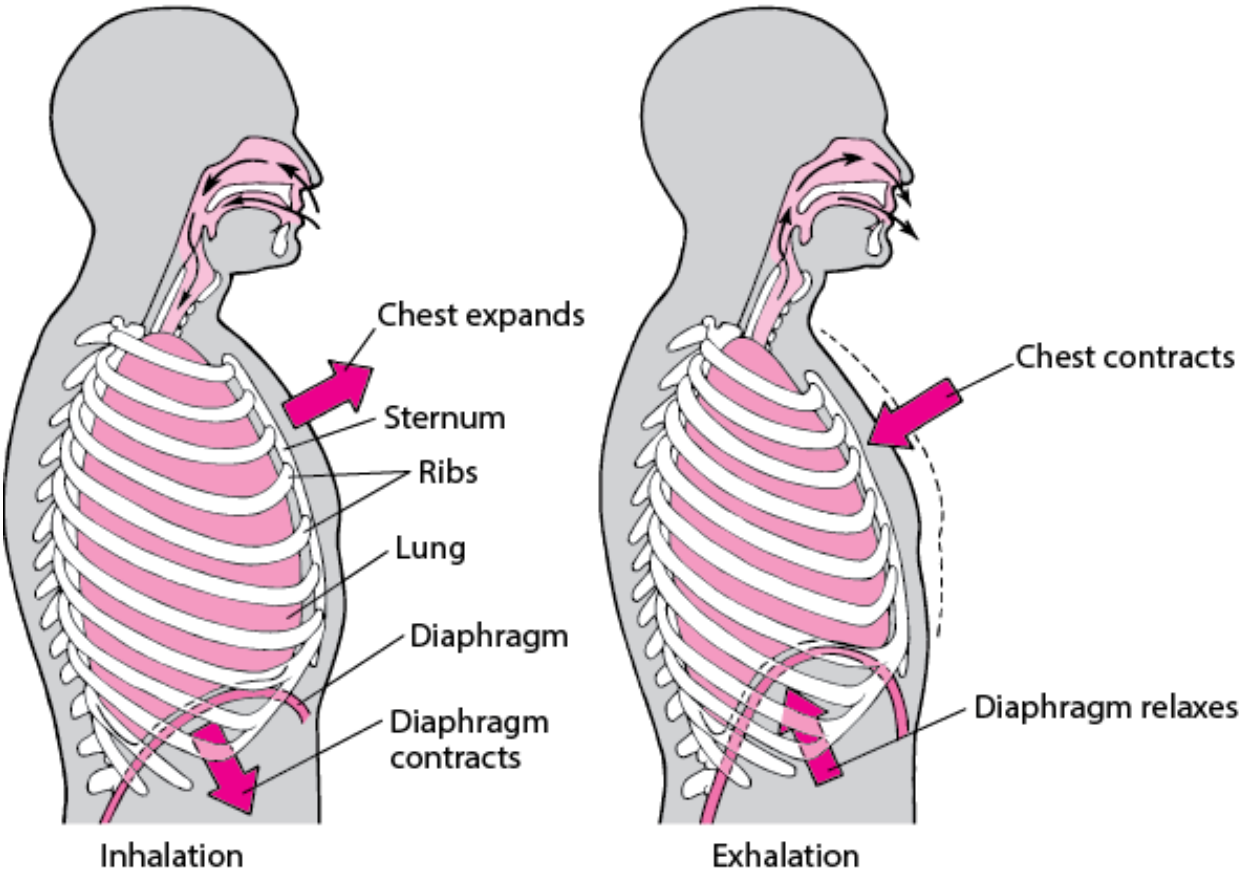

Figure 3.5: The displacements of the chest and abdomen walls of a sitting human during breathing in and out [208].

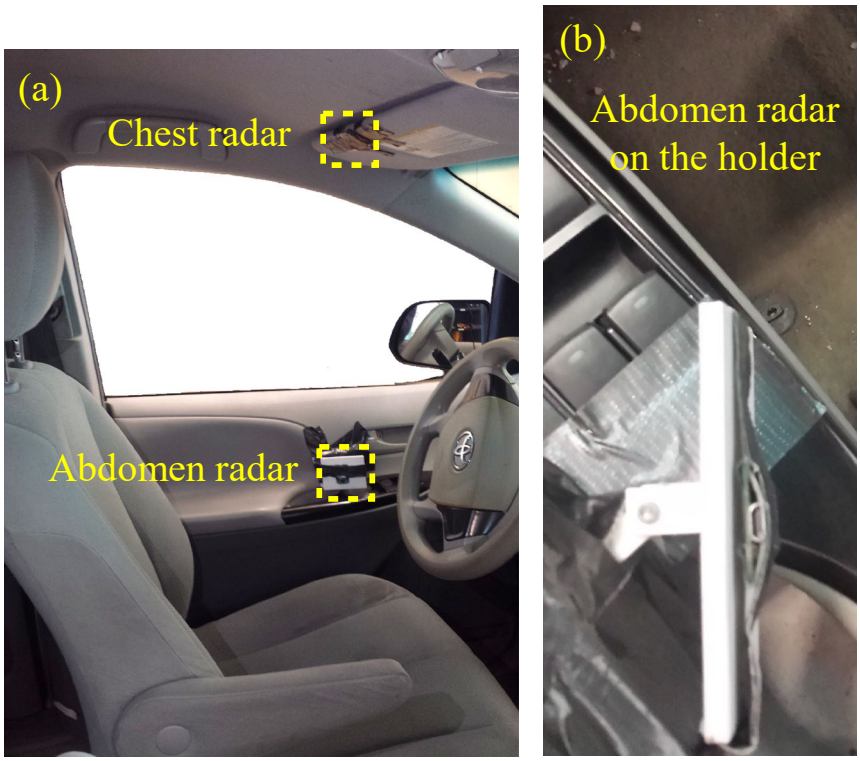

Figure 3.6: Radar placement: (a) The chest and abdomen radars placements in experimental studies and (b) abdomen radar tilted toward participants' abdomen.

3.3.2 Experimental Protocol

Eight subjects (four females and four males; age: 30 ± 6 years; weight: 75 ± 20 kg; height: 172 ± 13 cm; BR: 17 ± 8 bpm) without having any respiratory disease participated in these experiments. The participants were asked to sit behind the wheel as a driver and mimic different breath patterns using an online metronome [209] in a single-subject or dual-subject scenario while wearing a heavy jacket or shirt. In addition, various driving scenarios, including shoulder check (left then right), turning the wheel 90 degrees, and drinking a can, are examined in this study. The participants were asked to do these activities every 30 seconds. In the shoulder check scenario, the participants checked the left shoulder first. After 30 seconds, they did a right shoulder check. In the drinking a can scenario, the participants first picked a can from the drink holder inside the vehicle, mimicked drinking, and then returned the can to the drink holder. The entire scenario lasted approximately 4-5 seconds.

The estimated BR is compared with the actual BR based on the root mean square error (RMSE). The RMSE can be calculated as follows:

$$\mathrm{RMSE} = \sqrt{\frac{\sum_{n=1}^{N} \|y(n) - \hat{y}(n)\|^2}{N}}, \tag{3.11}$$

where N is the number of data, y(n) is the n^{th} measurement, and $\hat{y}(n)$ is its corresponding prediction.

3.3.3 The Recognition of Abnormal Breathing Patterns

Five abnormal breathing patterns, including Tachypnea, Bradypnea, Biot, Cheyne–stokes, and Apnea are investigated in the driving scenario in this study. Tachypnea is characterized by a BR of more than 20 bpm. On the other hand, Bradypnea is low BR, which is characterized by less than 12 bpm. Biot is characterized by some shallow breath patterns followed by some periods of Apnea. Cheyne–stokes is characterized by two stages. First, there is a progressive increment in both deepness and rate. Then, both the deepness and rate reduce gradually, which results in Apnea at the end [210].

Figure 3.7 illustrates two straightforward approaches for detecting different abnormal breathing patterns: BR estimation and breath-hold detection. BR estimation can be used to detect both Tachypnea and Bradypnea, characterized by BRs of more than 20 bpm and less than 12 bpm, respectively. Breath-hold detection can be employed to diagnose three different abnormalities: Biot, Cheyne–Stokes, and Apnea. Both Biot and Cheyne–Stokes include an Apnea period. Therefore, all three of these abnormalities can be diagnosed by breath-hold detection. It is worth noting that this study focuses on detecting these abnormalities in various driving scenarios.

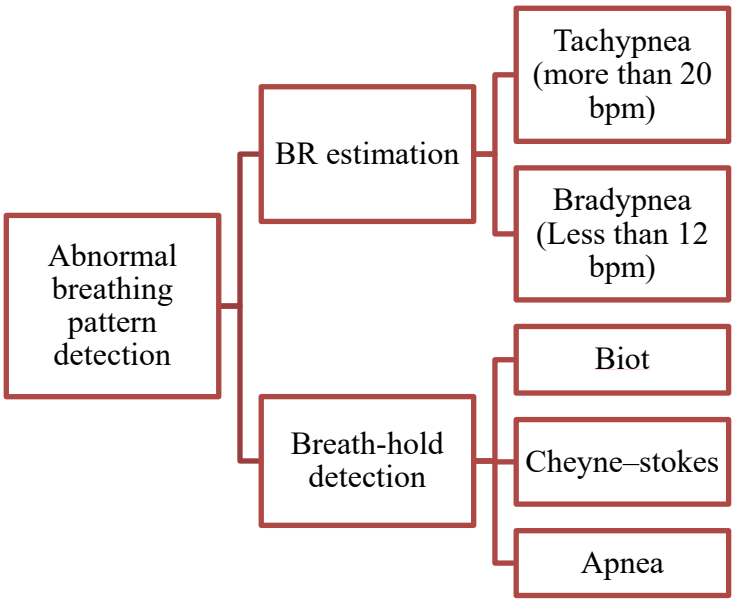

Figure 3.7: Approaches to detect different abnormal breathing patterns in this thesis.

3.4 Results and Discussion

3.4.1 Validation of the Proposed Algorithm

Figure 3.8 compares the effect of two different clutter cancellations, including clutter cancellation on chirps through all the frames and clutter cancellation on a frame on target detection in the chest radar. The target cannot be detected if the clutter is canceled in a frame because target reflections are also suppressed by clutter cancellation. However, if the clutter is suppressed through all the frames, it can detect the target in a true range after suppressing clutter reflections. Clutter cancellation applied on the range profile is only deployed for accurate range detection. However, clutter cancellation can affect the estimated breathing pattern. Figure 3.9 evaluates the effect of clutter cancellation applied on range profile in breathing pattern estimation. Although the measurement has a breath-hold period, the processed signals by clutter cancellation cannot represent any breath-hold period. However, while the chest wall displacement is low, unprocessed signals accurately represent the breath-hold period.

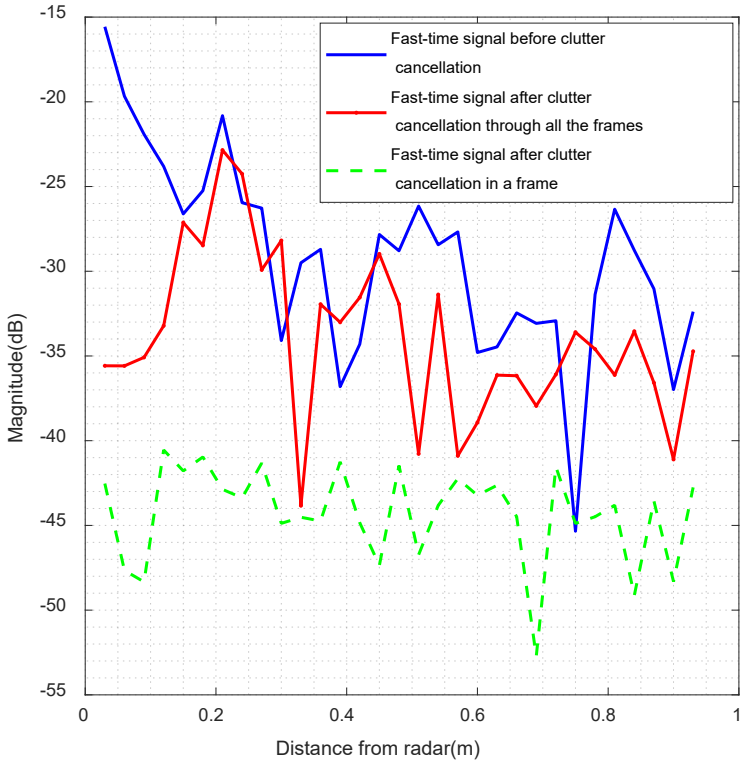

Figure 3.8: The comparison between different clutter cancellation approaches on the target detection in chest radar.

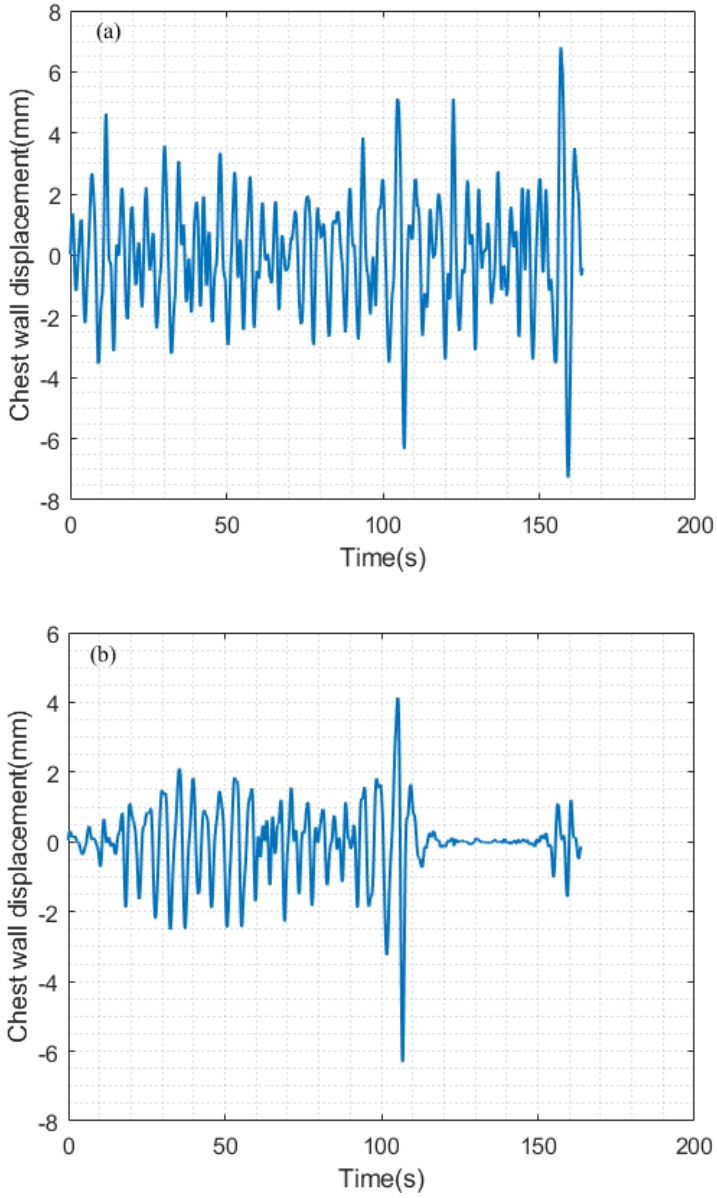

Figure 3.9: The effect of clutter cancellation on breathing pattern estimation while there is a breath-hold in the scenario: (a) The estimated breathing pattern with clutter cancellation and (b) The estimated breathing pattern without clutter cancellation.

Figure 3.10 depicts the various reflections in different ranges in both the chest and abdomen radars over time. There is a breath-hold in this scenario, which is accurately specified in both radars. First, both radars represent the target in the correct range as they are at 20 cm and 40 cm, respectively. Second, radar detects

multiple range bins for a subject as it is close to the subject. The chest radar can detect 4 range bins for a subject in this study. Third, both radars are not impacted by interference like other subjects' reflections since they are out of maximum range. Fourth, the chest radar is less affected by multiple reflections than the abdomen radar. As a result, the chest radar is reliable for multi-bin breathing pattern estimation, and the abdomen radar can complement the chest radar in detecting breath-hold periods.

An intuitive way to improve frequency resolution is to increase the processing window length. A longer processing window is also less susceptible to interference, such as body motions. Although a longer processing window is more robust to interference, it is less adaptive to BR changes. Given that the minimum normal BR is 12 bpm, the duration of one breath is 5 seconds. The minimum window length is 20 seconds by considering 4 cycles of this breathing pattern. Figure 3.11 illustrates the consistency of BR estimation over 35 seconds with a BR of 16 for various processing window lengths, including 20 seconds, 30 seconds, 40 seconds, and 50 seconds. The BR is estimated every second for these window lengths. A participant was asked to turn the wheel every 30 seconds in this measurement while mimicking different BRs. The results indicate that a window length of 40 seconds can estimate BR by approximately a maximum error of less than 1 breath per minute. For longer windows, the accuracy would be slightly higher than 40 seconds. However, longer windows are unable to detect breath-hold periods accurately. If the minimum duration of breath-hold is assumed to be 20 seconds, a window length of 40 seconds covers 50% of this period. Consequently, longer windows may lead to missing breath-hold periods.

To examine the interference effect in a dual radar system depicted in Figure 3.6(a), three disparate measurements are performed. First, the radars started to radiate signals simultaneously, but there was no metallic surface in front of the abdomen radar. Therefore, the radars interfered with each other, and the power level of interference in the chest radar obtained from the range-doppler map after zero-doppler cancellation exceeds -30 dB in the chest range, as shown in Figure 3.12(a). Second, the metallic surface was placed in front of the abdomen radar to avoid interference while the time delay was still zero. Figure 3.12(b) illustrates the suppression of the interference level by almost 3.5 dB. Finally, the metallic surface was removed, and a time delay of 5 μs was set between two radars. Figure 3.12(c) demonstrates a 3 dB suppression in the power level of interference after considering this time delay.

Table 3-2 compares the single-bin and multi-bin approaches based on the average RMSE in different BRs inside the vehicle while the subject had a slight body movement. Four subjects participated in the data collection for each BR. The length of measurement for each BR was 3 minutes. The multi-bin approach exhibits lower RMSE in most cases, especially in high BRs. However, the proposed multi-bin approach exhibits a slight degradation in BR estimation when BR values are 14 or 16. Nevertheless, the introduced

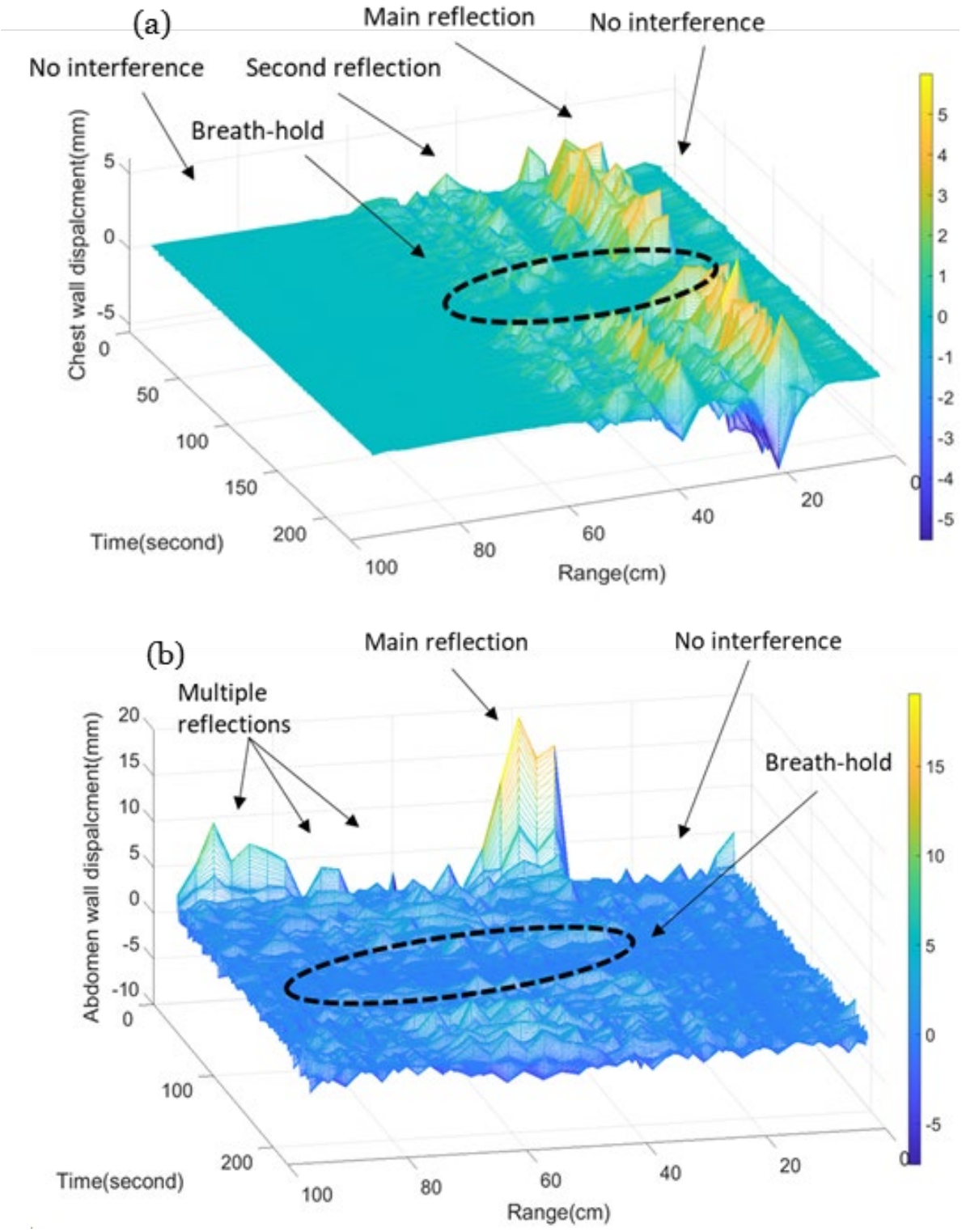

Figure 3.10: Reflection analysis in dual radar fusion over time: (a) chest radar and (b) abdomen radar.

error is negligible. The maximum error in the multi-bin approach reaches 1.2 bpm. However, the RMSE of the single-bin approach exceeds 2 bpm when BR is high.

Table 3-4 represents the average RMSE of various BRs in driving scenarios obtained from the chest radar. Four different scenarios are examined in this study, including turning the wheel, shoulder check, shoulder check while wearing a thick jacket, and drinking a can. Eight subjects participated in this measurement for 3 minutes for each BR. The participants were asked to do these activities every 30 seconds. Among the examined scenarios, turning the wheel is the most challenging one, especially in high BRs. In addition, wearing a thick jacket does not affect vibration signals since electromagnetic waves can penetrate through the clothes.

Figure 3.13 depicts the amplitude of the detected peak in the breathing pattern in the frequency domain over time while there were 5 breath-hold periods in this measurement from chest and abdomen radars, respectively. Both chest and abdomen radars can detect these breath-hold periods. However, two false detections with low displacements were detected in only one of the radars. As a result, reliable breath-hold detection can be achieved by a dual radar fusion system. Radar signals are sensitive to movements and can detect all breath-hold periods accurately. They tend to overestimate breath-hold periods, but the use of dual radar improves accuracy.

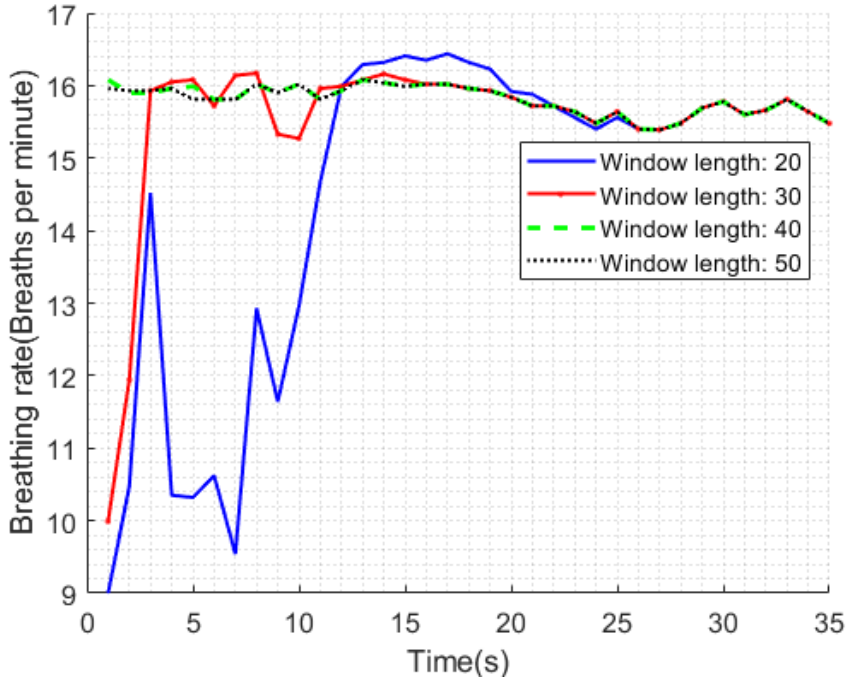

Figure 3.11: The consistency of BR estimation in 35 seconds while BR is 16 for various processing window lengths, including 20 seconds, 30 seconds, 40 seconds, and 50 seconds.

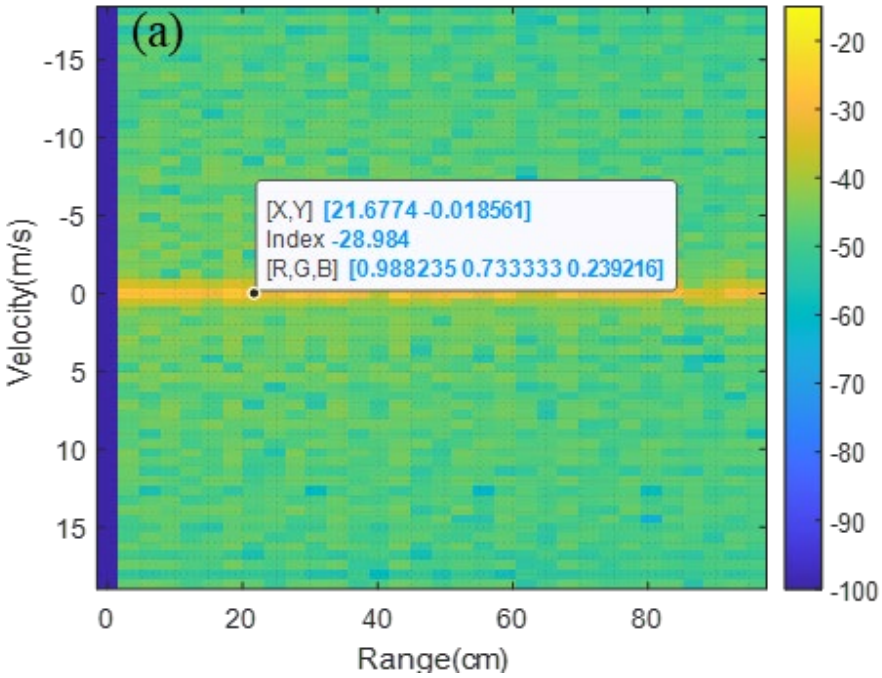
(a)
[X,Y] [21.6774 -0.018561]
Index -28.984
[R,G,B] [0.988235 0.733333 0.239216]
Velocity(m/s)
Range(cm)
-15
-10
-5
0
5
10
15
0
20
40
60
80
-20
-30
-40
-50
-60
-70
-80
-90
-100

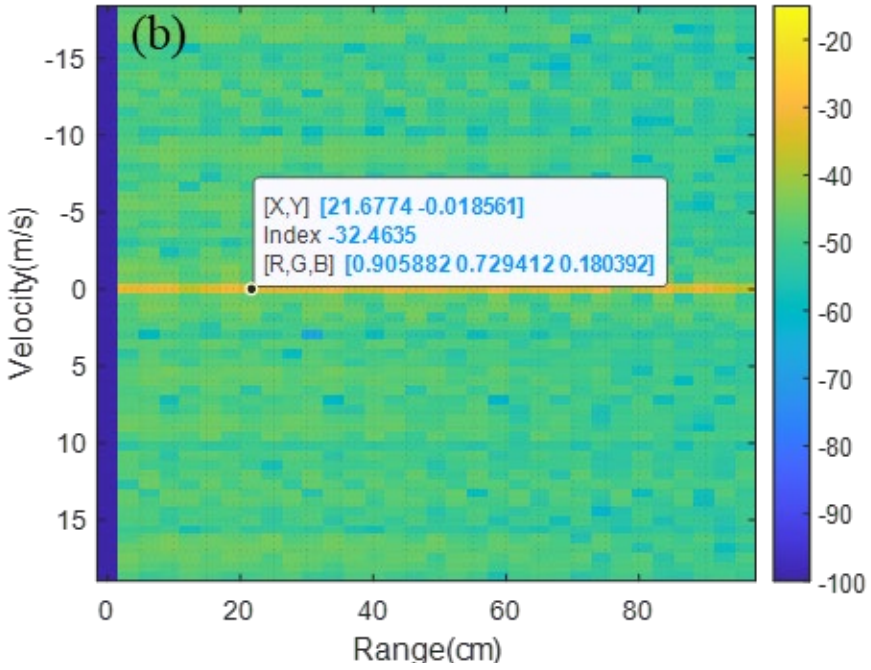
(b)
[X,Y] [21.6774 -0.018561]
Index -32.4635
[R,G,B] [0.905882 0.729412 0.180392]
Velocity(m/s)
Range(cm)
-15
-10
-5
0
5
10
15
0
20
40
60
80
-20
-30
-40
-50
-60
-70
-80
-90
-100

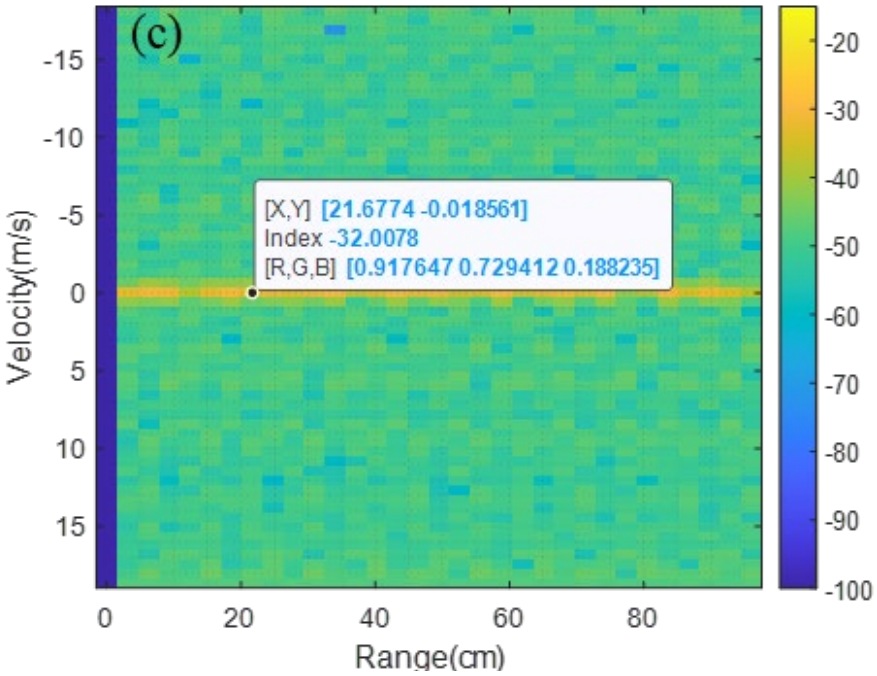

Figure 3.12: The power level of interference on the range-velocity map in different measurements: (a) no time delay and no metallic surface, (b) no time delay and a metallic surface, and (c) a proper time delay and no cupper surface.

Table 3-2: Comparison between single-bin and multi-bin approaches based on average RMSE(bpm) in various BRs inside the vehicle.

BR	Single-bin approach	Multi-bin approach
9	1.7	0.6
11	0.8	0.23
14	0.77	0.32
16	0.48	0.54
18	0.25	0.4
22	1.74	0.7
24	2.21	1.2
26	2.65	0.88

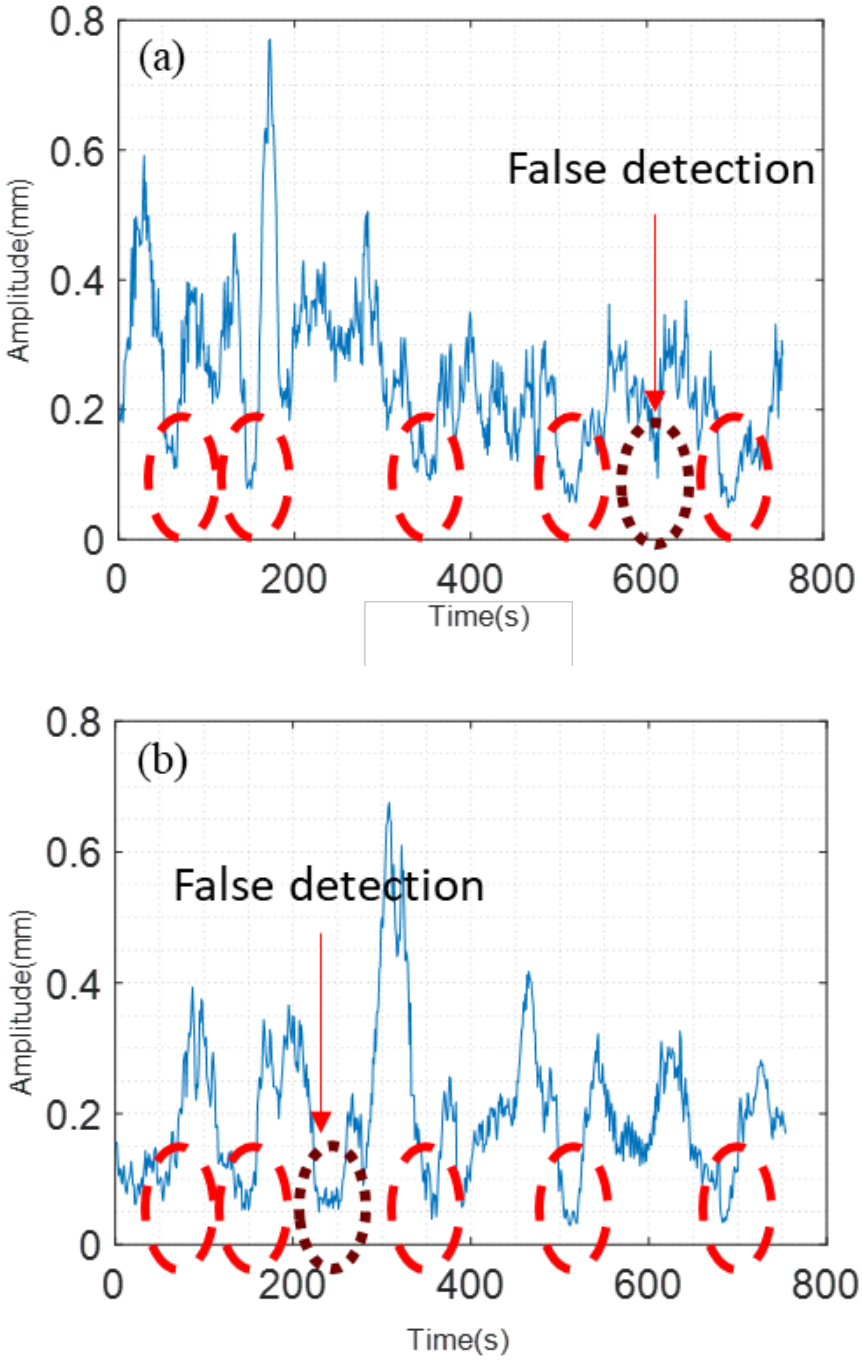

Figure 3.13: The amplitude of the detected peak in the breathing pattern in the frequency domain over time while there were five breath-hold periods in this measurement: (a) chest radar and (b) abdomen radar.

Table 3-3: Average RMSE(bpm) of chest radar in different BRs in driving scenarios.

BR	Turning the wheel	Shoulder check	Shoulder check while wearing a thick jacket	Drinking a can
9	0.91	0.7	0.28	0.36
11	0.88	0.47	0.35	0.67
14	0.79	1.18	0.92	0.65
16	0.87	0.8	0.56	0.49
18	0.64	1.02	0.43	0.77
22	1.61	0.58	1.3	0.94
24	1.42	1.1	0.69	0.86
26	1.23	0.52	0.36	0.83

3.4.2 Discussion

Table 3-4 presents a comparison between the approaches utilized in this thesis and those described in recently published papers. Firstly, it is noteworthy that most papers report a maximum estimation error for BR of less than 2 breaths per minute. Similarly, the multi-bin approach proposed in this thesis also demonstrates an error within this range. Secondly, the processing window length is another important criterion addressed in this study. While many recent papers suggest a window length of 60 seconds, a window length of 40 seconds is proposed. This choice is motivated by the fact that a longer window fails to accurately detect breath-hold periods. Additionally, it is worth mentioning that the analysis of driving scenarios, such as steering wheel movements, is a focus in recent studies.

Table 3-4: Comparison between the employed approaches in this thesis and recently published papers.

Reference	Maximum BR error (breaths)	Processing window length	Driving scenarios	Breathing abnormality detection
[45]	±2	60 s	Yes	No
[43]	±2	Not specified	Yes	Yes
[47]	±1.2	5 s	Yes	No
[25]	±2	30 s	Yes	No
[57]	±2.96	60 s	Yes	No
Single- bin	±4.36	40 s	Yes	Yes
Multi-bin	±1.9	40 s	Yes	Yes

Furthermore, previous studies mainly focused on accurately estimating BR rather than on detecting abnormalities. Similar to the proposed approach in this study, many of these studies achieved an RMSE of less than 2 bpm in BR estimation. The proposed approach achieved a maximum estimation error of 1.9 bpm

in BR. It is worth noting that BR estimation without considering the chest wall and abdomen wall displacements cannot detect breath-hold periods and breathing abnormalities. The chest radar incorrectly identified 37 periods as breath-hold, while the abdomen radar incorrectly identified 26 periods as breath-hold periods. However, no false breath-hold periods were detected by the proposed dual radar approach.

The proposed approach in this thesis has limitations in handling high random body motions within a processing window. One of the challenging body motions inside the vehicle is turning the wheel, which is a periodic movement [43]. If this activity lasts more than 10 seconds, the BR estimation is challenging, especially when the actual BR is more than 20. Although the BR usually drops to less than 10 bpm and RMSE is high, the abnormality is detected even if mislabeled. This phenomenon commonly occurs when the driver is stressed and steers the wheel sharply.

This study focused on the detection of abnormal breathing by dual radar. However, the application of dual radar is not limited to the detection of breathing pattern estimation. The abdomen radar in the proposed setup in this thesis can be employed for drowsy driver detection. Since normal breathing is a non-stop activity, the detection of drowsy drivers based solely on BR is less reliable. Because people are less active during sleep, the second radar can be employed for activity recognition. As a result, if the driver is less active than normal and the BR is also low, it can be considered indicative of a drowsy driver.

3.5 Conclusion

Radar, as a contactless sensor, offers the benefit of operating in various environmental conditions while preserving privacy. This study employed a dual 60 GHz radar fusion system to monitor the respiratory patterns of drivers. This system can detect five breathing abnormalities that can occur in drivers, including Tachypnea, Bradypnea, Biot, Cheyne–Stokes, and Apnea. Two features extracted from breathing patterns to detect these abnormalities are BR and displacement amplitude. The maximum error of BR estimation in this thesis by the multi-bin method reached 1.9 breaths in the driving scenarios. However, the error for a single-bin approach was 4.36 breaths. The proposed dual radar system can recognize the breath-hold period without false detections. These fused radars have less interference with each other, benefiting from the finest range resolution. Furthermore, proper signal design can mitigate the effect of passengers' reflections, which could otherwise interfere with the driver's reflections. Although the dual radar system demonstrated promising results, its cost remains a drawback. Alternatively, employing a single MIMO radar offers a more cost-effective solution for monitoring individuals.

Chapter 4
Multiple People Monitoring by a MIMO Radar

4.1 Relevance

Although employing multiple radars to monitor an individual offers several advantages, certain challenges persist. Firstly, installing multiple radars within a vehicle may lead to distractions for drivers, potentially increasing the risk of car accidents. Secondly, the intricate wiring required presents a challenge and adds complexity to cabin design. Lastly, the overall cost is substantially higher than that of using a single MIMO radar.

This chapter explores the monitoring of multiple individuals using a MIMO radar. Initially, the algorithm is validated using a corner reflector and a protractor mat at various angles. Subsequently, the beamforming algorithm is applied to radar data with known angles and ranges, extracting breathing waveforms within the vehicle. The aim is to monitor multiple individuals inside the vehicle at different distances or the same distance with varying angles from the radar. Additionally, occupancy detection inside the vehicle by a MIMO radar focusing on left-behind child detection is explored.

4.2 Radar Sensor.

For data collection in this chapter, the Texas Instrument (TI) mm-wave MIMO FMCW radar sensors are used (IWR6843ISK and AWR6843AOP) [211], operating within the 60 GHz to 64 GHz frequency range. These radars, designed for mm-wave MIMO FMCW operations, offer both range-azimuth details of subjects and capture their vibrations. Given their capabilities, these radars prove to be an ideal choice for in-cabin applications [211].

The considerations for choosing the appropriate radar sensor were:

- The MIMO FMCW radar stands out among radar systems due to its distinctive features. This type of radar enables simultaneous detection of range, angle, and vibrations, making it well-suited for diverse applications.
- The notable benefits of the latest generation of these radars include being cost-effective, budget-friendly, and scalable.
- The radar sensor operates at low power levels, with transmitted signals having a power level of less than 10 dBm. This contrasts with Wi-Fi signals, which exceed 20 dBm, and cellphones typically

operating around 30 dBm. In terms of power consumption, this system is considerably more energy-efficient than other wireless devices, minimizing potential negative health effects and making it suitable for long-term use. Operating at 60 GHz, this mm-wave radar utilizes non-ionizing radiation, unlike X-rays that ionize body molecules. Additionally, mm-waves, absorbed by water and not penetrating the body, result in electromagnetic absorption at frequencies over 10 times less than those used in cellular bands and Wi-Fi, further enhancing its health-safety profile.

4.3 Beamforming for Multiple People Monitoring.

For multiple people's breathing monitoring, it is crucial to employ a digital beamforming approach, especially if there is a symmetric scenario like inside a vehicle. By using digital beamforming and knowing the subject's angles and ranges, the antenna beam can be steered toward the subject. Therefore, it is crucial to make sure that the beamforming algorithm works accurately.

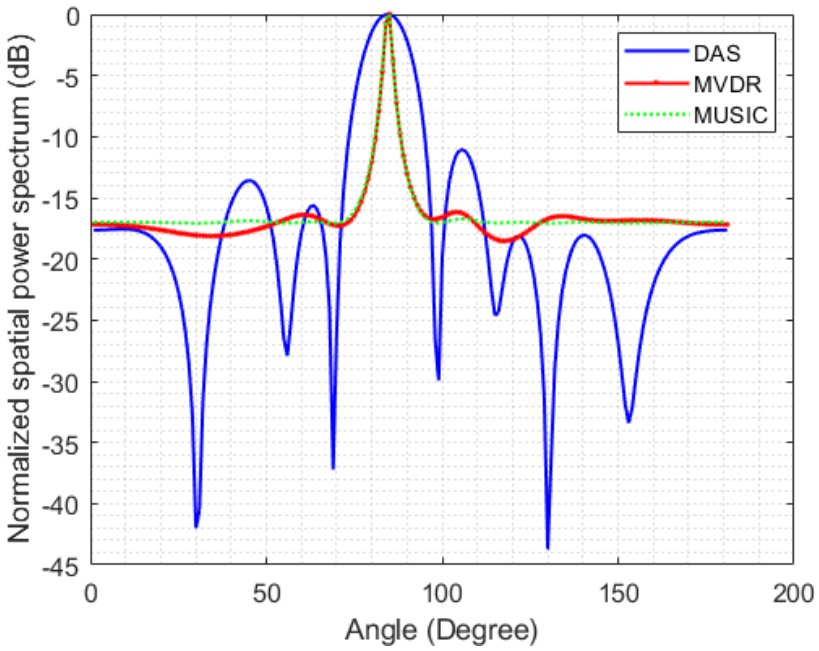

Figure 4.1: The compassion between different beamforming approaches, including DAS, MVDR, and MUSIC, while there is a target in front of radar.

There are various digital beamforming algorithms for the receiver side in the literature. In this study, three common algorithms are discussed, including delay and sum (DAS), minimum variance distortionless response (MVDR), and multiple signal classification (MUSIC). As can be seen in Figure 4.1, MUSIC and

MVDR approaches have 5 dB and 5.5 dB better main lobe to side lobe ratio than DAS, respectively. However, the MVDR approach has less computational cost than MUSIC. As a result, the MVDR approach is used for beamforming in this thesis.

4.3.1 Beamforming Algorithm Verification

To verify the beamforming algorithm, a corner reflector on a protractor mat at different angles can be used. Figure 4.2 depicts an IWR6843ISK radar in the center of the protractor mat while the corner reflector is at an angle of 40 degrees. Both radar and corner reflector have the same height from the ground surface. In addition, the distance between the radar and the corner reflector is almost 80cm. In this study, most angles are examined to verify algorithm accuracy.

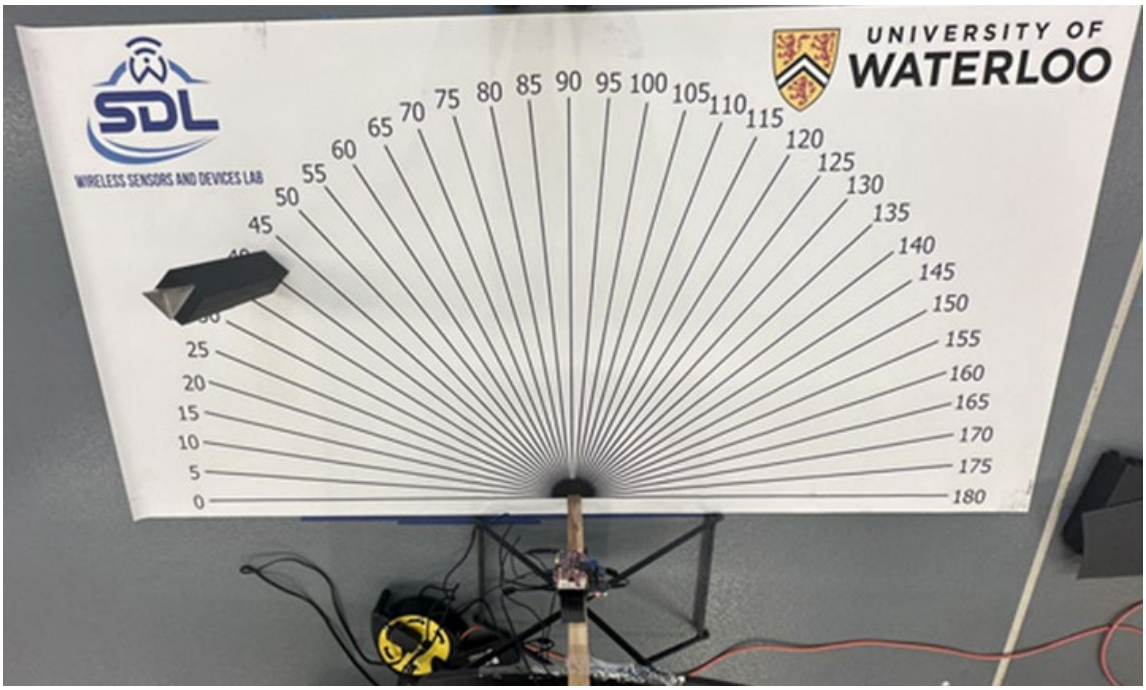

Figure 4.2: A corner reflector on a protractor mat to examine the digital beamforming algorithm.

4.3.1.1 Single Reflector with Various Virtual Channels

Figure 4.3 and Figure 4.4 display the beamforming results for a corner reflector at 90 degrees and 125 degrees, respectively, with the radar situated roughly 80 cm away from the target while different virtual channels have been used for beamforming. The estimated angles exhibit considerable accuracy with 4 and 8 virtual channels. However, the estimated peak in 8 virtual channel beamforming exhibits a narrower and stronger peak than 4 virtual channel beamforming. In addition, the reflected signal's amplitude from the 90-

degree angle is 1.74 dB higher than that from the 125-degree angle. This variation can be attributed to the antenna gain pattern, which is weaker on side angles. As a result, by using more virtual channels, the system is enabled to detect and discriminate targets.

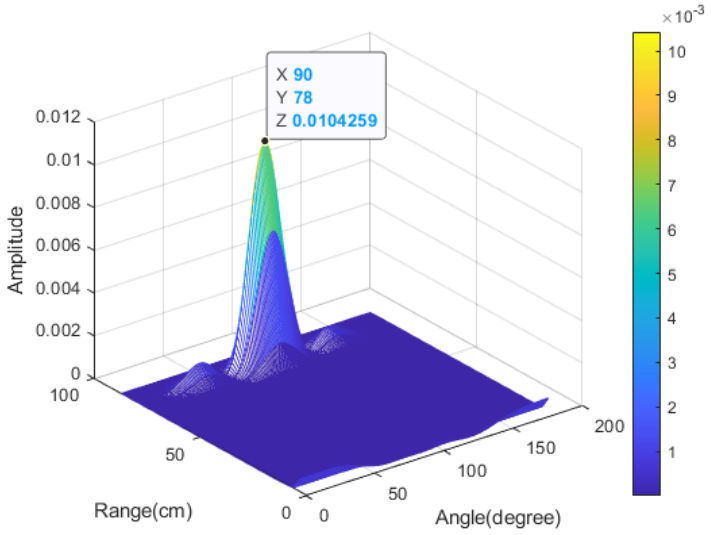

(a)

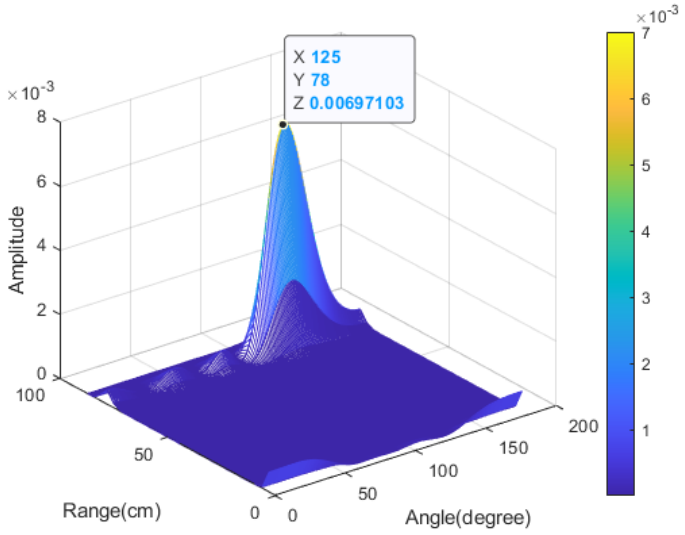

(b)

Figure 4.3: The result of MVDR beamforming for a corner reflector by 4 virtual channels: (a) 90 degrees and (b) 125 degrees.

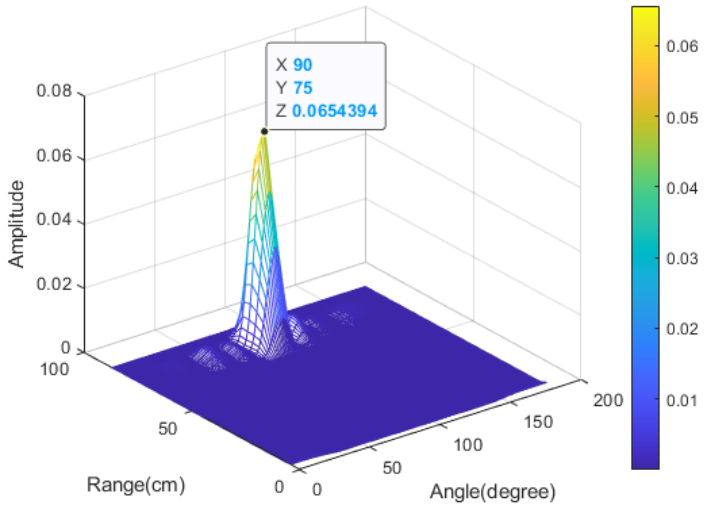

(a)

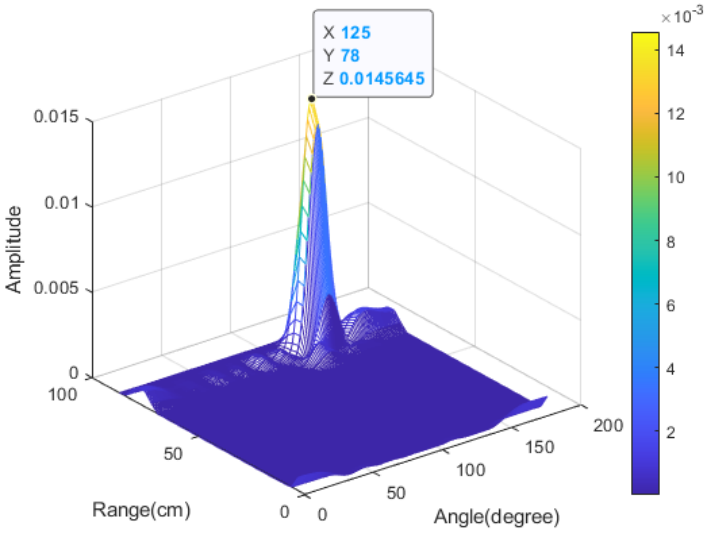

(b)

Figure 4.4: The result of MVDR beamforming for a corner reflector by 8 virtual channels: (a) 90 degrees and (b) 125 degrees.

4.3.1.2 Dual Reflector Separation

Figure 4.5 displays the beamforming results for two corner reflectors at different angles, with the radar situated roughly 25 cm away from the target while 8 virtual channels have been used for beamforming. The results indicate that when the angle difference between targets is more than the angle resolution of a system, which is 14 degrees, the corner reflectors can be separated, as can be seen in Figure 4.5(a) and Figure 4.5(b). In addition, the estimated angles have a 1-to-2-degree error, which is negligible for this study. However, when the angle difference between corner reflectors is less than the angle resolution of the system, the system cannot separate these two targets. As can be seen in Figure 4.5(c), the system is not able to separate two targets with an angle difference of 10 degrees. Instead, it displays a single target in the middle of these two targets. It seems that the reflections of these two targets are positively summed up and made a fake target.

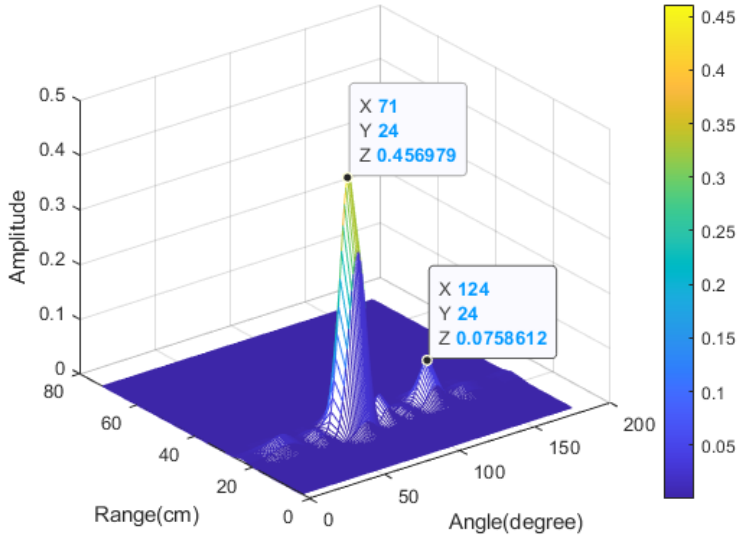

(a)

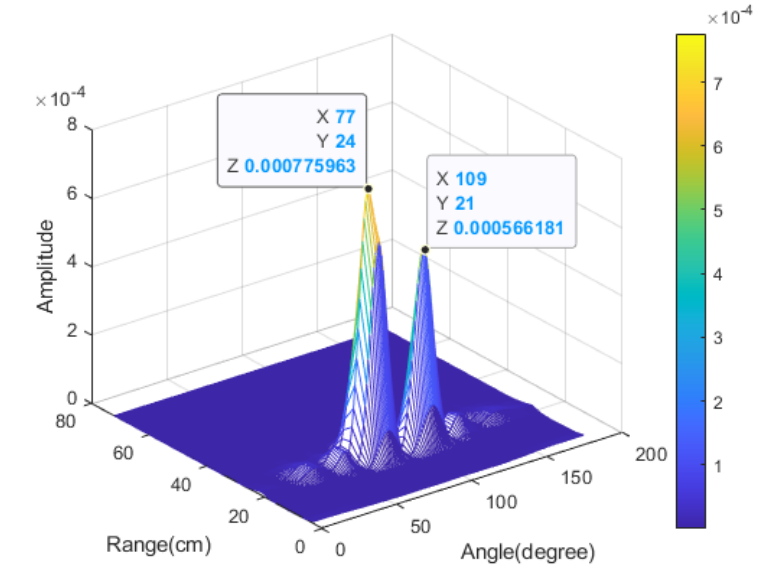

(b)

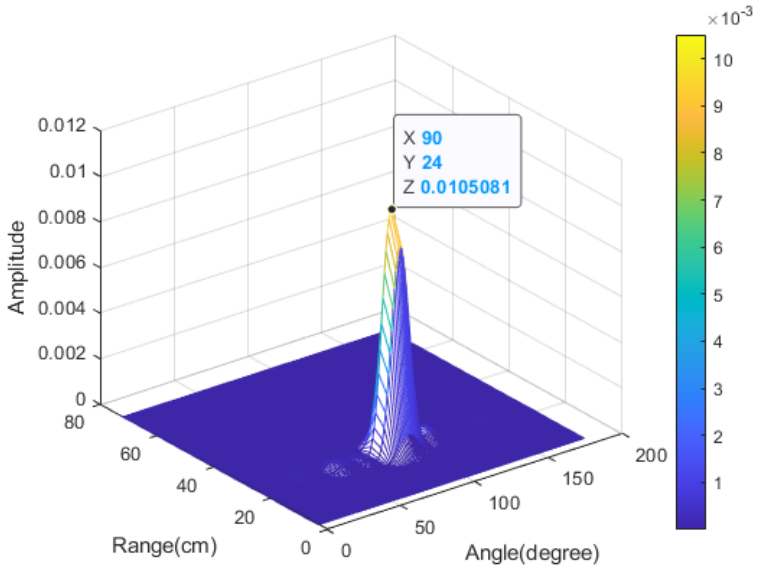

(c)

Figure 4.5: The result of MVDR beamforming for two corner reflectors by 8 virtual channels: (a) the angles of corner reflectors are 70 and 120, (b) the angles of corner reflectors are 75 and 110, and (c) The angles of corner reflectors are 85 and 95.

4.4 In-vehicle Applications of MIMO Radars

4.4.1 In-Vehicle Multiple People Breathing Monitoring

Figure 4.6 depicts the in-vehicle radar setup for breathing monitoring. The employed off-the-shelf radar is IWR6843ISK from TI which has 3 transmitters and 4 receivers at 60 to 64 GHz. However, since the second transmitter covers elevation angles, only two transmitters have been used. Therefore, there are 8 virtual channels for beamforming [211]. In addition, radar is installed on the rear-view mirror which is the best place to monitor vital signs [127]. To evaluate the algorithm, single and multiple-people scenarios inside the vehicle were considered. The length of the processing window is 40 seconds, and the multi-bin approach is employed. The data has been collected from different scenarios, which are described below.

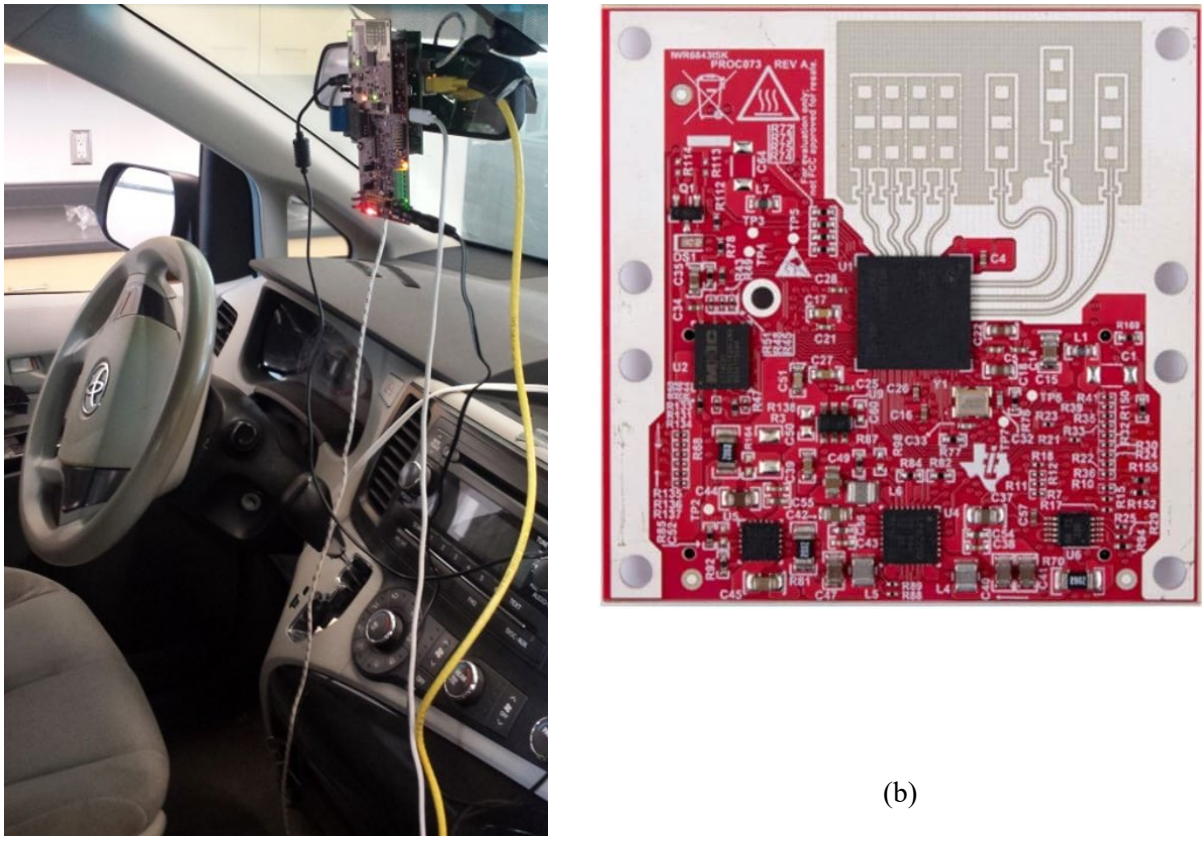

(a) (b)

Figure 4.6: The In-cabin monitoring setup: (a) the installed system on the rear-view mirror in-vehicle for breathing monitoring and (b) IWR6843ISK [211].

4.4.1.1 Single Person Scenarios

In this subsection, the single-person scenarios are examined for left-behind human applications. Two different scenarios are examined in this section, including left-behind adults and babies. Figure 4.7 depicts the scenario of the left-behind adult in which seat number 4 is occupied. As can be seen in the beamforming results, the detected peak for the adult appears at 70 degrees at 176 cm from radar. There is also another peak which is reflected from the car body as the angle of the peak is 164 degrees. Table 4-1 represents the average RMSE in various BRs inside the vehicle for this scenario. The maximum average RMSE is 0.9 breaths per minute in this table.

Table 4-1: Average RMSE in various BRs inside the vehicle for Figure 4.7.

BR	Multi-bin approach
9	0.8
12	0.54
15	0.64
18	0.74
21	0.9

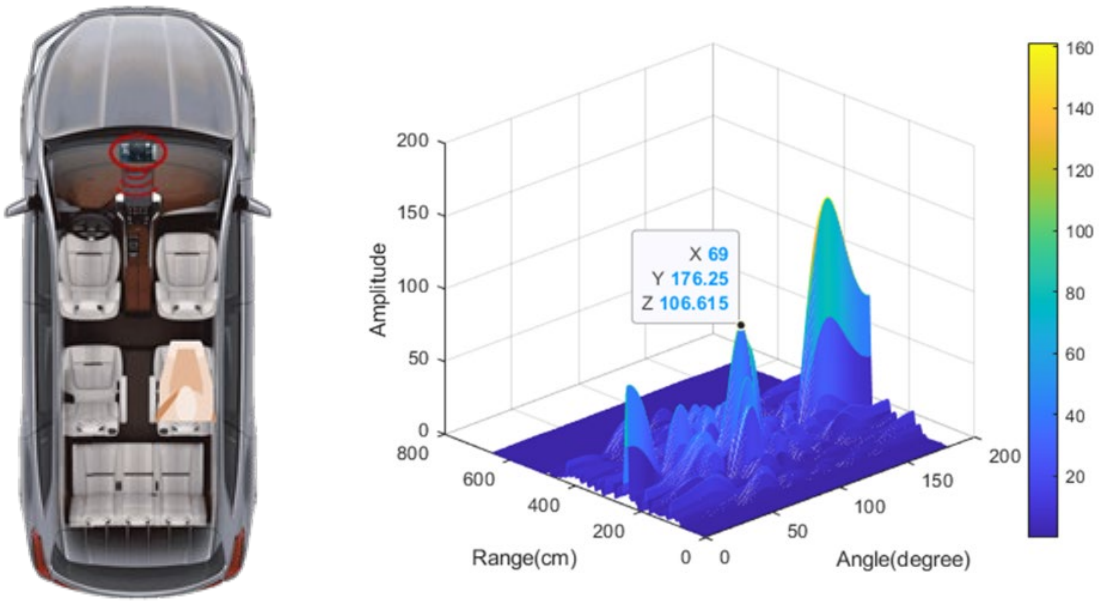

(a) (b)

Figure 4.7: The left adult scenario in the back seat: (a) the scenario and the occupied seat and (b) beamforming results.

Figure 4.8 depicts a left-behind baby scenario in which seat number 4 is occupied by a doll. There is also another peak which is reflected from the car body as the angle of the peak is 164 degrees. As can be seen in the beamforming results, the detected peak for the baby appears at 59 degrees at 184 cm from the radar. The BR of the doll is set at 20 breaths per minute. The average RMSE for this BR is 0.65 breaths per minute.

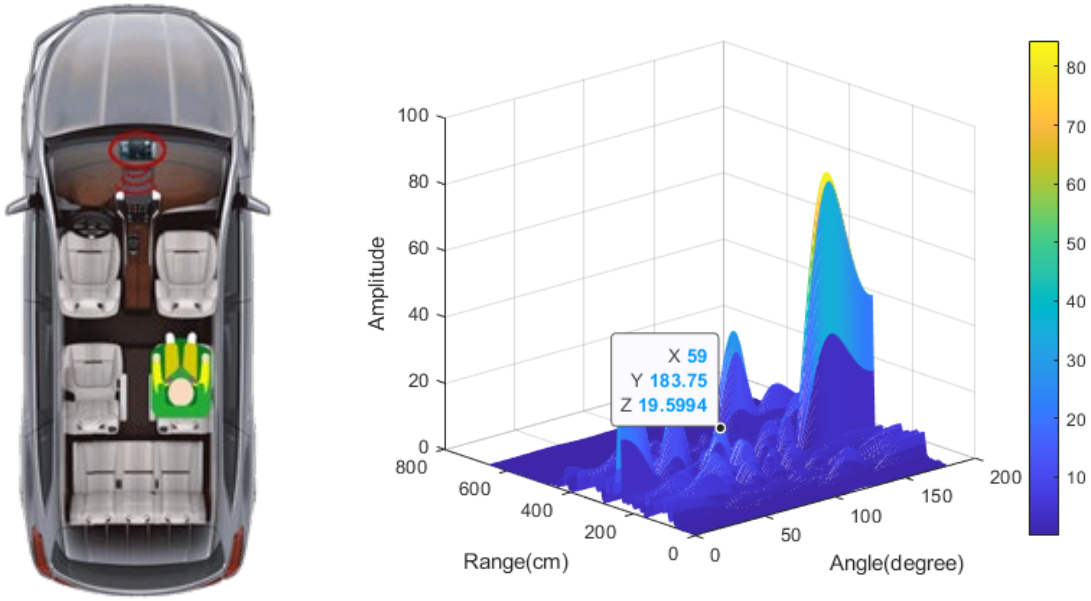

(a) (b)

Figure 4.8: The left baby scenario in the back seat: (a) the scenario and the occupied seat and (b) beamforming results.

4.4.1.2 Multiple People Scenarios

In this subsection, five different scenarios in which multiple people are examined. Figure 4.9 depicts the first scenario in which the first row is occupied by two adults. As can be seen in the beamforming results, the detected peak for the driver appears at 125 degrees at 75 cm from radar, and the adult in the second seat also appears at 55 degrees and 56 cm from radar. Table 4-2 represents the average RMSE in various BRs inside the vehicle for the driver. The maximum average RMSE is 1.3 breaths per minute in this scenario. For the second seat, the BR of the adult is set at 15 breaths per minute in the whole scenario. The average RMSE is 1.8 breaths per minute for this scenario.

Figure 4.10 depicts the second scenario in which the first and third seats are occupied by two adults. As can be seen in the beamforming results, the detected peak for the driver appears at 129 degrees at 78 cm

from radar, and the adult in the second seat also appears at 118 degrees and 191 cm from radar. However, there are multiple reflections from the first seat, which are combined with the second subject's signals; as can be seen, the second subject's reflections are stronger than the first subject ones, although the driver is closer to the radar, and has a larger body mass.

Table 4-3 represents the average RMSE in various BRs inside the vehicle for the driver in the scenario shown in Figure 4.10. The maximum average RMSE is 1.4 breaths per minute. For the Third seat, the BR of the adult was set at 15 breaths per minute in the whole scenario. However, the average RMSE is 3.4 breaths per minute for this scenario. It seems that the driver's multipath reflections are sometimes dominant when combined with the second subject's reflections.

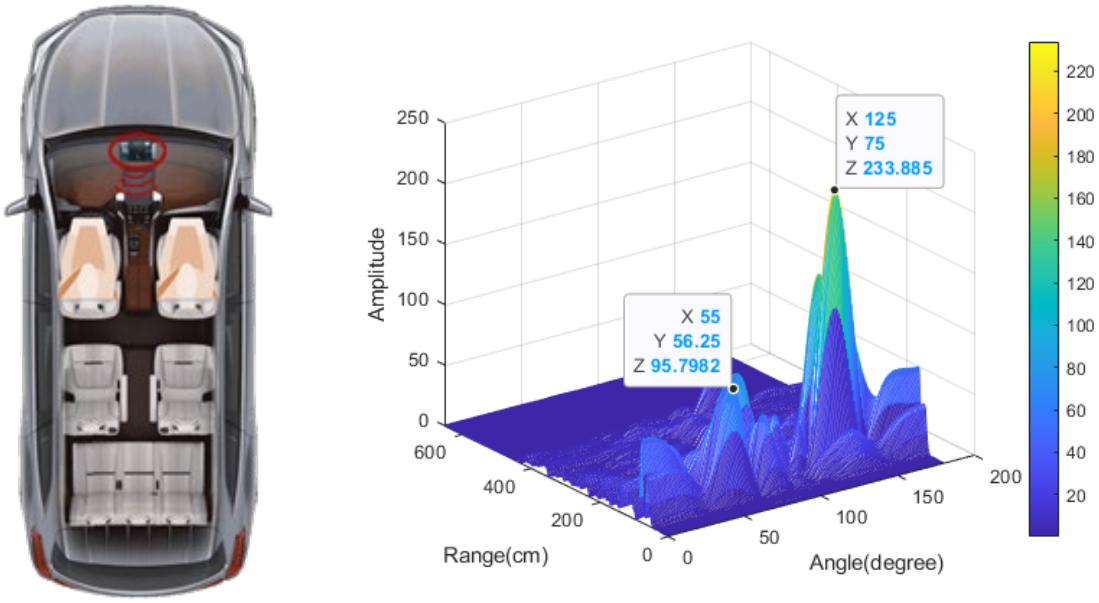

(a) (b)

Figure 4.9: Dual adult scenario occupied the first row: (a) the scenario and the occupied seats and(b) Beamforming results.

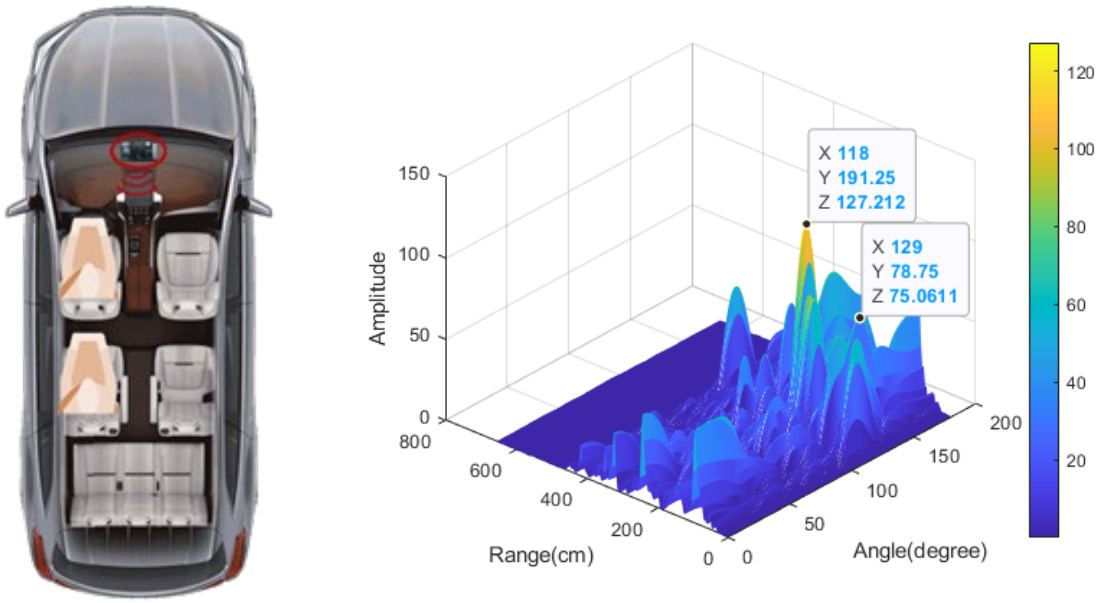

(a) (b)

Figure 4.10: Dual adult scenario occupied the first and the third seats: (a) the scenario and the occupied seats and (b) beamforming results.

Table 4-2: Average RMSE in various BRs inside the vehicle for Figure 4.9.

BR	Multi-bin approach
9	0.74
12	0.84
15	0.79
18	1.1
21	1.3

Table 4-3: Average RMSE in various BRs for the driver in Figure 4.10.

BR	Multi-bin approach
9	0.95
12	0.73
15	0.65
18	1.2
21	1.4

Figure 4.11 depicts three dual-people scenarios in which only one seat from each row is occupied. Table 4-4 represents the average RMSE in various BRs inside the vehicle for the subjects in the first row in these scenarios. The maximum average RMSE is 1.31 breaths per minute. The second seat has a higher rate of error than the first seat. It is because of antenna gain, which is stronger on the right side. For the fourth seat, the BR of an adult is set at 15 breaths per minute, or the BR of the baby is set at 20 breaths per minute in the whole scenario. However, the average RMSE is 5.1, 5.6, and 6.2 breaths per minute for these scenarios, respectively. It seems that the driver's multipath reflections are sometimes dominant when combined with the second subject's reflections.

(a) (b) (c)

Figure 4.11: Dual people scenarios: (a) the first and fourth seats are occupied by an adult and a baby, respectively, (b) the second and fourth seats are occupied by an adult and a baby, respectively, and (c) the second and fourth seats are occupied by two adults.

In conclusion, using a single MIMO radar for monitoring multiple people in multiple rows due to the multipath effect of in-cabin environments is challenging. Therefore, MIMO radars can effectively

monitor multiple people who are seated in a row. Using a multi-beam approach may help reduce the effect of multipath inside a vehicle.

Table 4-4: Average RMSE in various BRs inside the vehicle for the subjects in the first row in the scenarios of Figure 4.11.

BR	Figure 4.11(a)	Figure 4.11(b)	Figure 4.11(c)
9	0.75	1.1	0.66
12	0.63	1.2	0.84
15	0.43	0.95	0.98
18	0.86	0.91	1.21
21	1.12	1.31	1.14

4.4.2 In-Vehicle Occupancy Detection

Three common kinds of radars are employed for in-cabin applications, including CW radars, UWB radars, and FMCW radars. CW radars cannot provide a sufficient range resolution for in-vehicle applications. UWB radars generate a short-time pulse which leads to distinguishing between reflected signals of the nearby targets [127], [142], [143], [144], [212], [213], [214], [215]. However, these radar systems operate based on the amplitude of signals. Therefore, they can be affected by clutter reflection, especially inside a vehicle. FMCW radars sweep from a low frequency to a high frequency to cover a wide frequency range and provide a high-resolution system [149], [216]. MIMO FMCW radars represent the state-of-the-art technology for in-cabin applications, as they are capable of range detecting and angle differentiation of targets [15], [127], [217], [218].

There are different signal processing techniques to detect occupancy. The most straightforward approach is to use reflected energy. This technique is commonly used for detecting left-behind children and pets, especially in cold or hot conditions [11], [73], [96], [97], [98], [99], [100], [101], [102], [103], [104], [127]. The most common approach is based on the extracted features of micro-doppler [6], [7], [70], [71], [72], [73], [74], [75], [76], [77], [78], [79], [127] due to the human body motions. Then, AI is employed to detect individuals. These features are usually extracted from a time-frequency map [71], [72], [73], [77], [79], [127], a range-azimuth map [6], [74], [127], or a range-doppler map [80], [127]. In conclusion, recent studies mostly focused on energy-based approaches for occupancy detection.

However, energy-based approaches are highly dependent on the range of targets from radar based on the radar equation [144]. Therefore, these approaches need to have a separate database for each seat, which adds complexity to the classification. In addition, the multipath reflections can affect energy-based

approaches, especially when the front seats are occupied by adults. In this thesis, a volume-based occupancy detection approach based on the detected point cloud is proposed. This approach is less dependent on the range of targets from radar and uses only 3 labels, including adult, baby, and empty. This approach is more robust to multiple reflections from other seats compared to energy-based approaches.

4.4.2.1 Experimental Setup

Figure 4.12 represents the placement and relative spacing of the transmitter and receiver antennas and the equivalent antenna array in AWR6843AOP. The angle resolution (θ_{res}) of a MIMO radar when targets are in front of the radar can be determined as follows:

$$\theta_{res} = \frac{2}{N_{Tx}.\ N_{Rx}} \tag{4.1}$$

where N_{Tx} and N_{Rx} represent the number of transmitters and receivers, respectively. The azimuth and elevation angle resolutions by using all the transmitters equals 28.6° when targets are in front of the system. Figure 4.13 shows the AWR6843AOP radar sensor mounted above the headrest of the first-row seats while tilted slightly toward the second row. It is capable of detecting across two rows of a vehicle with about 120-degree azimuth and 120-degree elevation field of view. Table 4-5 describes the key parameters of the radar system used in this thesis. AWR6843AOP sensor with a start frequency of 60 GHz is used for overhead mount occupancy detection.

Table 4-5: The key parameters of the used system [82].

parameter	Configuration
Device	AWR6843AOP
Number of transmitters	3
Number of receivers	4
Field of view	120° horizontal, 120° vertical
Maximum range	2.7 m
Range resolution	5.3 cm
Maximum velocity	1.7 m/s
Velocity resolution	1.5 cm/s
Frame periodicity	200 ms

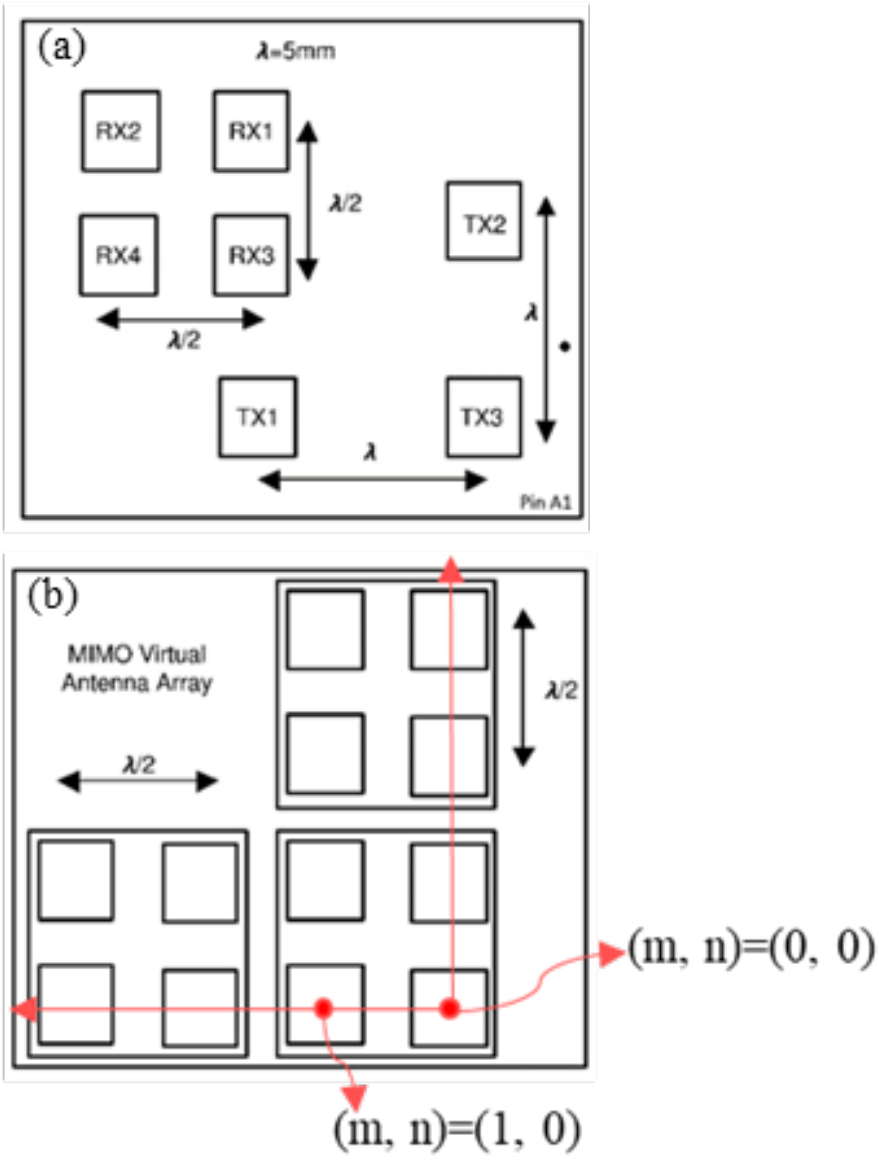

Figure 4.12: MIMO antenna array: (a) antenna positions and (b) equivalent virtual array. λ represents wavelength which is equal to 5 mm at 60 GHz [82].

Figure 4.13: Radar setup inside the vehicle for occupancy detection.

70 different scenarios, including single-subject and multi-subject scenarios, are implemented. 4 subjects were involved in tests from age 12 to 50, with weights from 35 Kg to 90 Kg and heights from 130cm to 180cm. Bella Rose baby doll from Ashton Drake is also used to mimic a baby [219].

4.4.2.2 Signal Processing Chain for Point Cloud Detection

Figure 4.14 shows the signal processing chain for point cloud detection. First, an FFT is applied to the beat signals to obtain range information. Then, the radar cube is reconstructed from the received chirp signals over time. Since occupants inside the vehicle are non-stationary, zero velocity clutter removal is performed, and 2D Capon is used in the next step. Then, the CFAR method is used to distinguish between targets and noise and generate a point cloud. The produced point cloud has a range, azimuth angle, elevation angle, and SNR for each point.

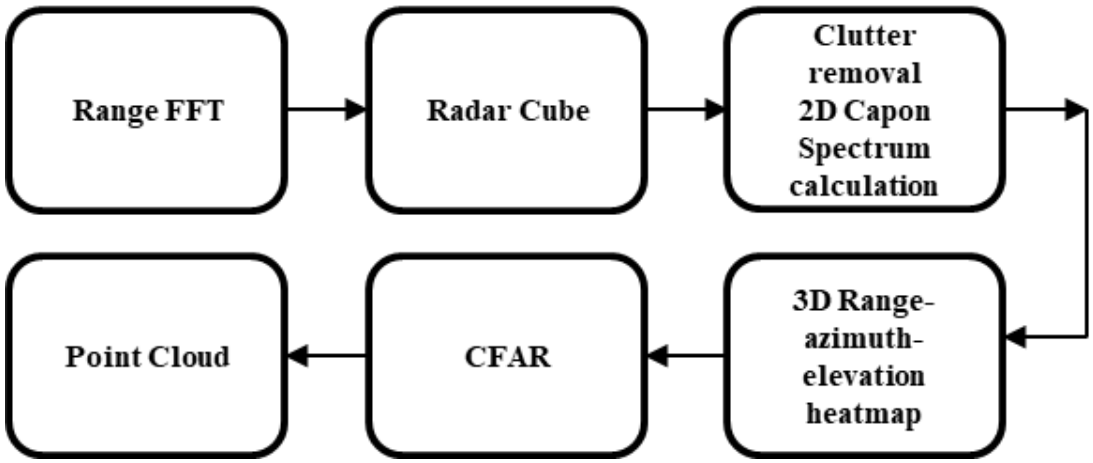

Figure 4.14: The signal processing chain for point cloud detection.

4.4.2.3 Results and Discussion

Three different occupancy detection approaches are used in this thesis. The first approach is the mean SNR of all the detected points for each seat. The number of detected points for each seat is considered the second approach. The proposed method to detect occupancy uses the location variance of the detected points for each seat as the last approach. All the detected points are divided between different seats based on the defined zones on the x-z plane.

The proposed approach demonstrates more robustness against false detections caused by multipath signals. The SNR-based approach may determine the occupancy correctly if those false points have low SNR. The in-cabin applications of radar, however, often suffer from a high amplitude of falsely detected points due to the low range of targets from radar. Consequently, in such scenarios, the SNR-based approach misclassifies empty seats as occupied. However, the proposed variance-based approach remains accurate due to the low location variance of those falsely detected points.

Figure 4.15 represents the detected points for an adult in seat 2 in a single target scenario. The majority of detected points are located inside the designated zone for seat 2. It also shows that the other seats are empty in this scenario. On the other hand, Figure 4.16 shows a falsely detected point due to the multipath in seat 5. Figure 4.16 displays that the mean SNR of detected points for this empty seat, even over time, is like an occupied seat. However, the variance-based approach indicates this seat is empty.

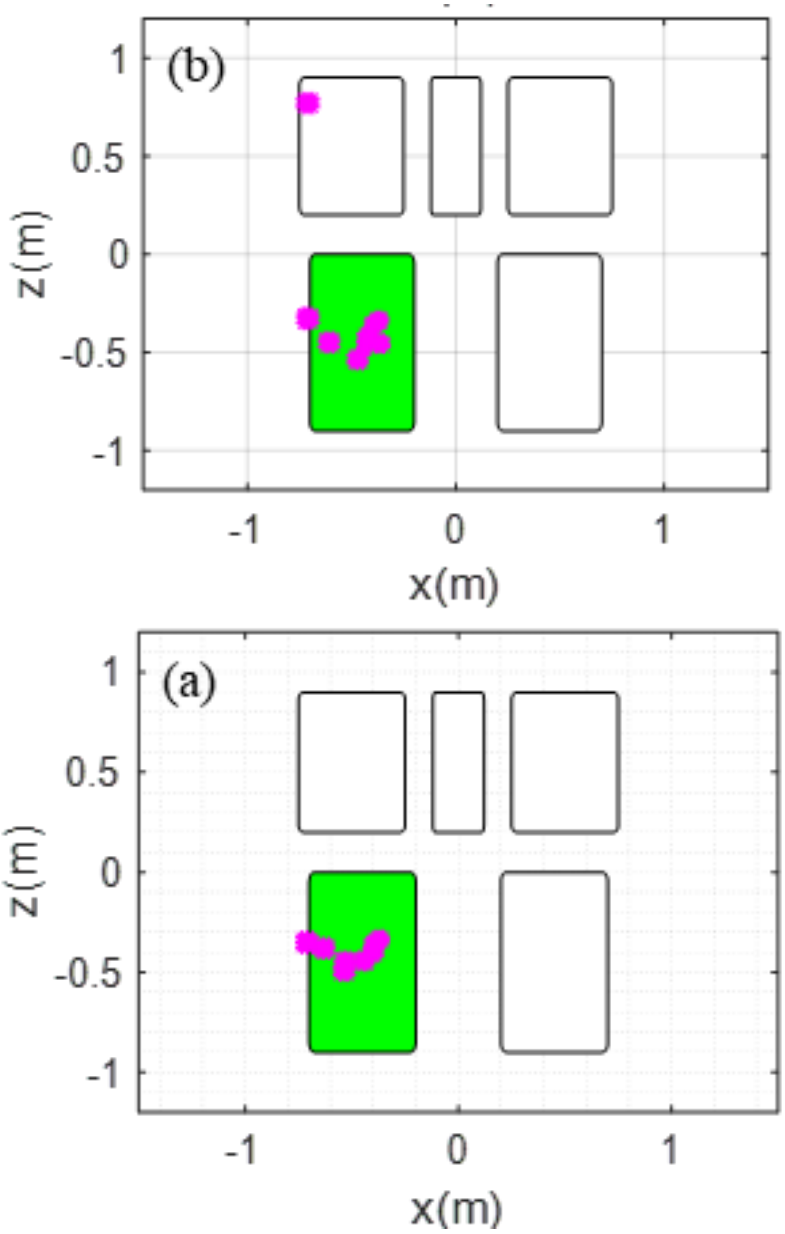

Figure 4.15: The detected points for an adult in seat 2 in a single target scenario: (a) without multipath issue and (b) with multipath issue.

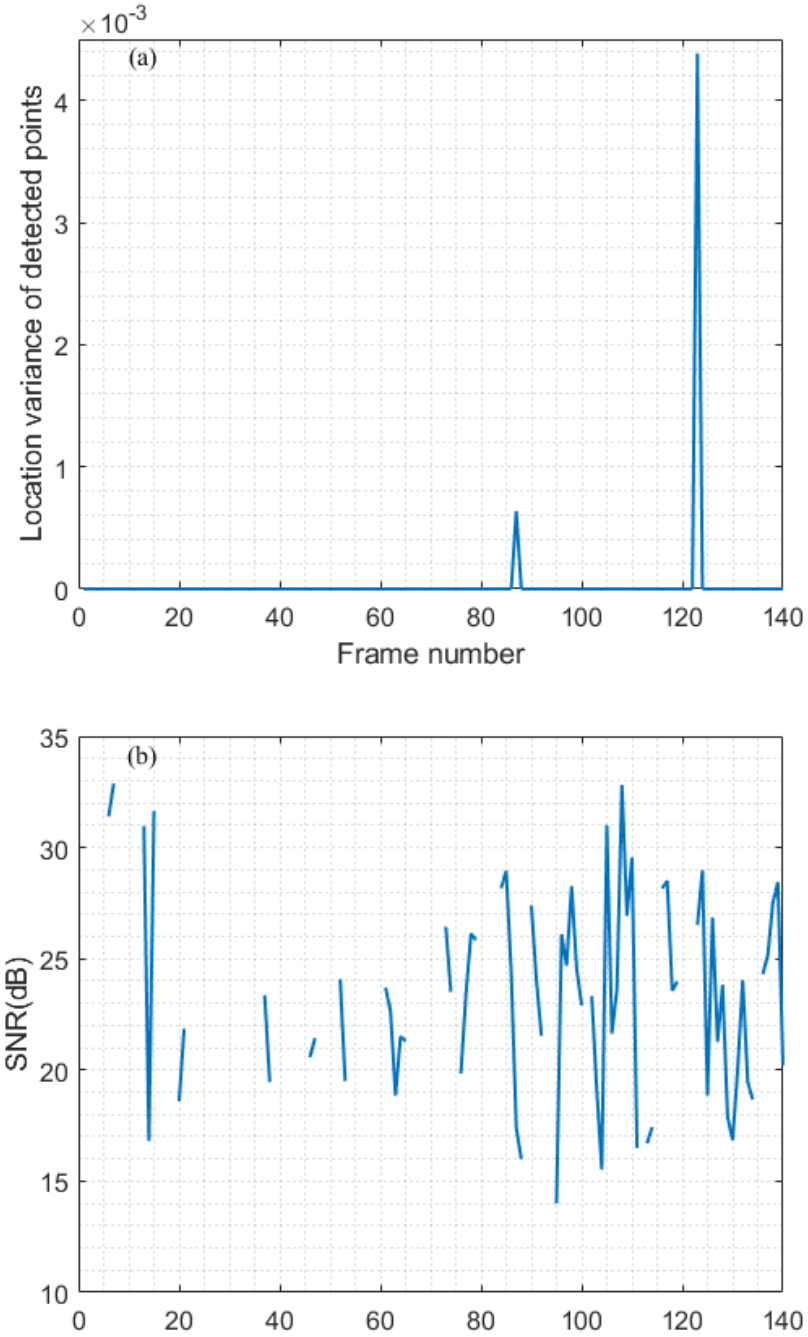

Figure 4.16: The multiple reflections from seat 2 on seat 5: (a) the location variance of detected points and (b) the mean SNR.

Figure 4.16Figure 4.17 shows the number of detected points in all seats for both adults and babies over 28 seconds (140 frames). In general, adults exhibit a higher number of detected points compared to babies

across different seats. Therefore, this indicator can identify the occupancy type of each seat individually. However, seat 3 shows fewer detected points for both an adult and a baby. Therefore, data collection needs to be conducted for each seat separately, resulting in the utilization of 17 labels for this indicator.

Figure 4.18 shows the mean SNR of detected points in all seats for both adults and babies over 28 seconds (140 frames). The SNR can distinguish between adults and babies in different seats. However, seat 4 exhibits a higher SNR for both an adult and a baby compared to other seats. The SNR of a baby in seat 4 has almost the SNR level as the SNR of adults in other seats. This indicator is inversely proportional to the range of the power of 4, as specified in the radar equation [144]. As a result, The SNR indicator also needs separate data collection for each seat, resulting in the utilization of 17 labels.

Figure 4.19 shows the location variance of detected points in different seats for both adults and babies over 28 seconds (140 frames). The location variance of detected points can differentiate between adults and babies in all seats. Unlike SNR, the location variance indicator exhibits less dependency on the range. Therefore, all seats represent the same amount of location variance for different occupancy types. Consequently, separate data collection for each seat is unnecessary.

Figure 4.17, Figure 4.18, and Figure 4.19 depict that all the methods presented in this thesis display fluctuations over time. Firstly, due to the low activity level of the human body before both inhalation and exhalation, human body reflections are suppressed by clutter cancellation. Secondly, occupancy type should be decided over time rather than relying on a single frame. In addition, all the indicators can distinguish between an empty seat and an occupied seat accurately. This capability allows the radar to differentiate between a left-behind baby case and an empty seat.

In the last step, a machine learning approach is employed to accomplish the classification task. To address the class imbalance, the synthetic minority oversampling technique is applied before training and testing. This technique mitigates the bias of classification by generating new data for minor labels. Nine different features, including minimum, maximum, mean, skewness, kurtosis, median, entropy, shape factor, and impulse factor, are extracted from each measurement. For training purposes, 80% of the data is utilized, while the remaining 20% is reserved for testing. Minimizing the miss-detection of babies is crucial to prevent heatstroke-related fatalities. The AdaBoost algorithm achieves a low miss-detection rate of just 1.3%, ensuring a high level of accuracy in identifying babies. Moreover, its overall detection accuracy stands at 96.7%.

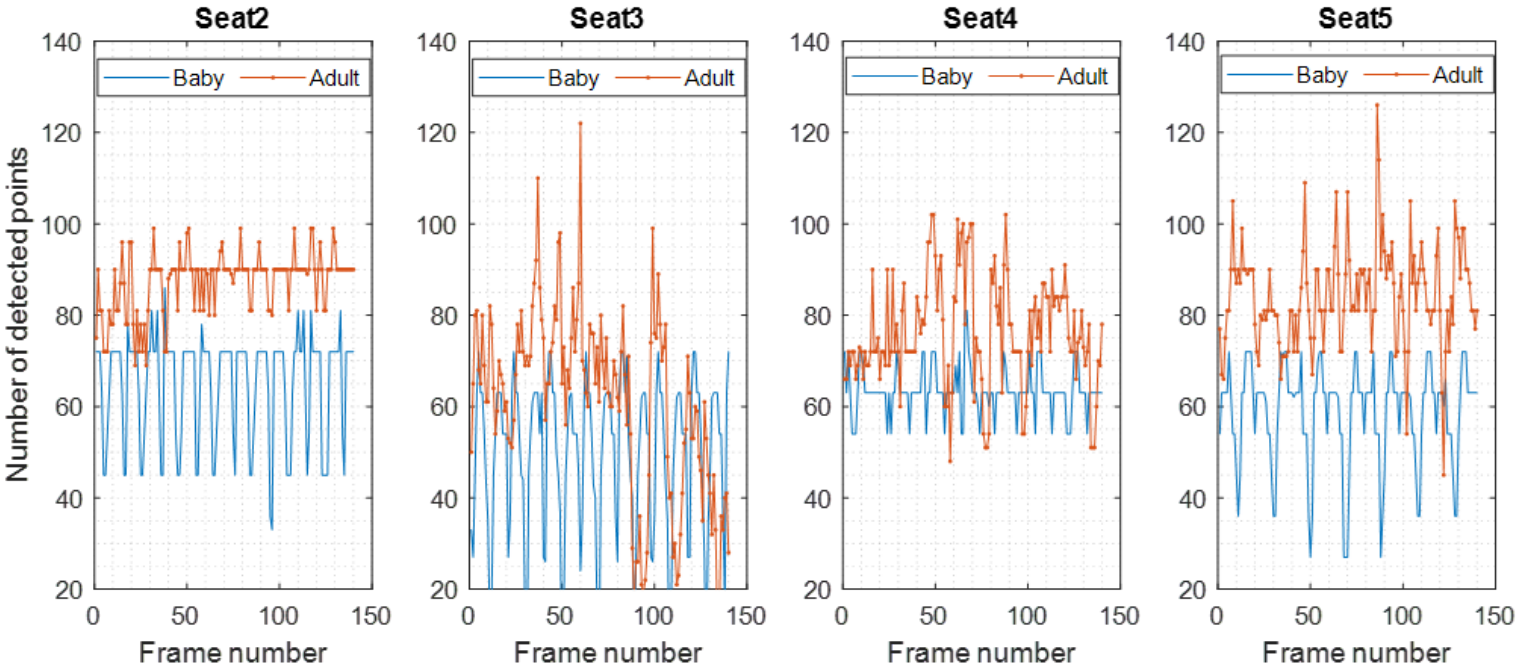

Figure 4.17: Number of detected points over 140 frames (28 seconds).

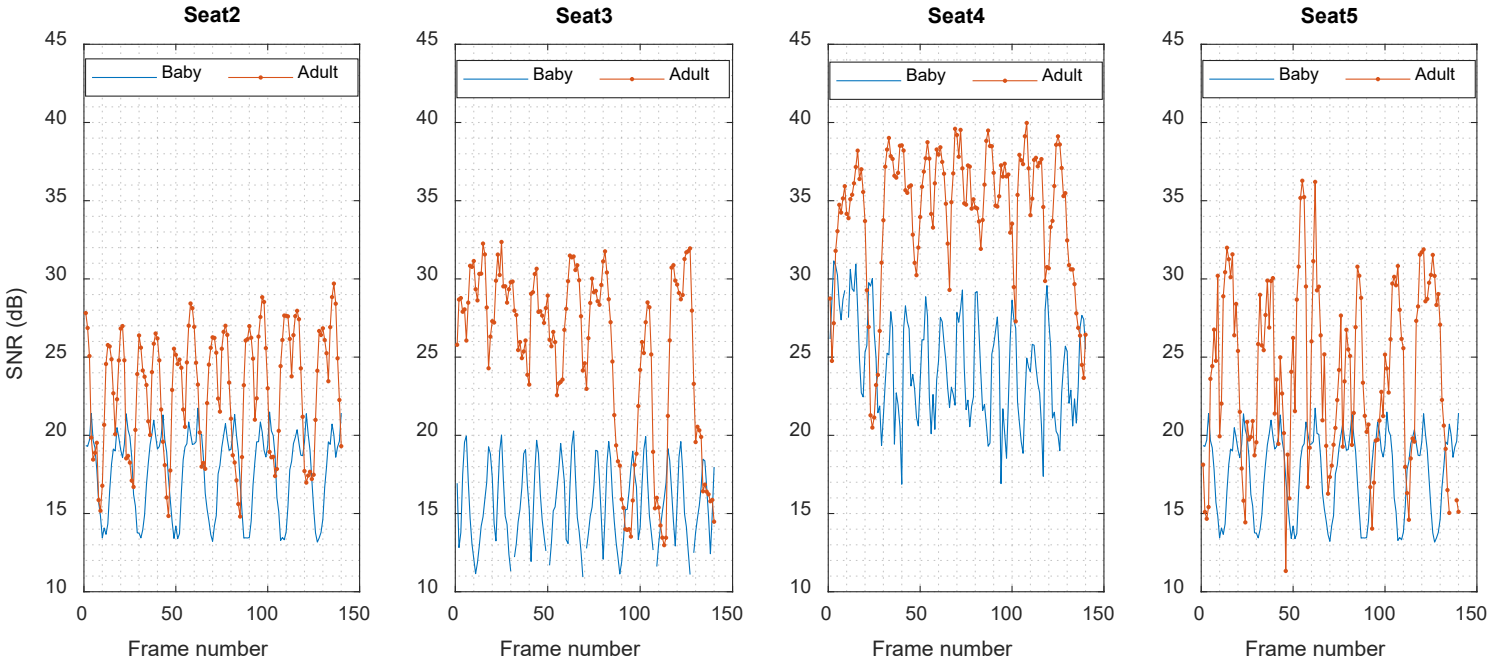

Figure 4.18: Mean SNR of the detected points over 140 frames (28 seconds).

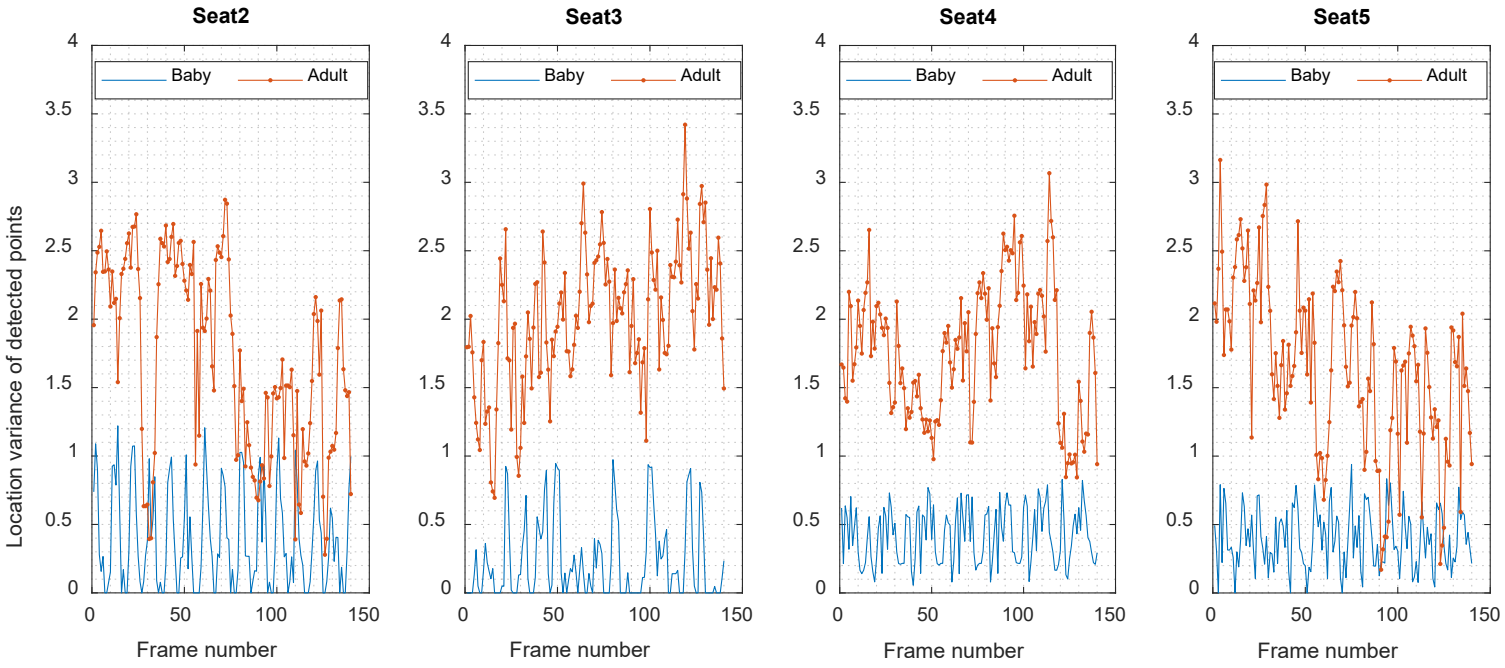

Figure 4.19: Location variance of detected points over 140 frames (28 seconds).

4.5 Conclusion

In conclusion, radars as non-contact sensors offer various applications inside the vehicle while preserving privacy. In this thesis, two important applications, including multiple-person vital sign monitoring and occupancy detection, are explored. Monitoring multiple individuals across multiple rows using a single MIMO radar presents challenges due to the multipath effect within in-cabin environments. Hence, MIMO radars offer effective monitoring solutions for individuals seated in a single row. Additionally, MIMO FMCW represents state-of-the-art technology that is capable of detecting occupancy even in dead spots. Recent studies proposed different approaches based on analyzing the reflected energy across range, angle, or frequency. These approaches are highly dependent on the range of occupants on the radar, requiring a separate database for each seat for occupancy detection. In addition, the energy-based approaches are susceptible to interference from multipath reflections. However, the proposed volume-based occupancy detection approach is seat-agnostic. Consequently, there are 3 labels, including adult, baby, and empty, in the classification task.

Chapter 5
Cardiac Health Monitoring Using Mm-Wave Radar

Utilizing radar technology to monitor the health of individuals within smart seats offers a practical solution to assess their well-being. While a couple of health monitoring systems have been proposed, many of them deal with issues related to user convenience and privacy. Radars present themselves as an appealing alternative due to their non-contact nature, ability to preserve privacy, adaptability to various environmental conditions, and high precision. Among the radar configurations, FMCW radars excel in accurately tracking crucial body vibrations, rendering them particularly suitable for heart waveform monitoring—a vital health indicator for the early detection of cardiac irregularities. In this study, a 60 GHz FMCW radar system is placed strategically behind a seat, facilitating the monitoring of heart waveforms. The proposed algorithm adeptly identifies distinctive heart waveform patterns for healthy subjects characterized by the sequential emergence of two peaks followed by a valley in each cycle. However, individuals with the prolonged corrected QT interval (QTc) have shown different heart waveform patterns.

The effects of three different sources of distortion are explored in this chapter, including breathing harmonics, body movements, and car body vibration. Breathing harmonics and body movements are explored in smart homes. High-frequency components of breathing, potentially with high amplitude in the heart band, are suppressed in heart waveform reconstruction after decomposing by variational mode decomposition (VMD). Additionally, the impact of body movements in seated individuals was mitigated within the time domain. The proposed body movement detection approach successfully identifies all strong body movements. Finally, this system was implemented inside a running vehicle to monitor both drivers and passengers. Significant car vibrations caused by road defects were detected using IMU data. Finally, a comprehensive study focused on HRV and HR estimation is conducted.

5.1 Relevance

The utilization of a single MIMO radar for monitoring multiple individuals across multiple rows in in-cabin environments presents challenges, primarily due to the multipath effect. Furthermore, for accurate monitoring of heart and breathing vibrations to detect heart and breathing conditions, strategic radar placement is essential to minimize interference from other sources of vibration, such as hand and head movements. Therefore, positioning the radar behind the seat can effectively monitor heart and breathing movements while also reducing distractions for drivers, allowing them to focus on driving.

Furthermore, recent studies have primarily concentrated on the detection of HR, BR, and HRV. However, utilizing radar measurements to analyze heart waveforms presents a promising avenue for identifying heart conditions such as prolonged QTc. Individuals with this condition may exhibit normal HR and HRV, making it challenging to detect solely based on these parameters. Therefore, detecting such conditions requires additional efforts, including the extraction and analysis of heart waveforms.

Finally, it is crucial to explore the impact of additional interferences, even with the radar placed behind the seat. These interferences may include body movements, deep and shallow breathing, and car body vibrations. Mitigating these interferences is essential to obtain accurate heart waveforms, which are crucial in detecting heart conditions. Therefore, a thorough investigation is warranted to effectively mitigate the effects of these interferences in this thesis.

5.2 The Heart Functionality

The heart is typically divided into four main chambers: the right atrium (RA), right ventricle (RV), left atrium (LA), and left ventricle (LV), as shown in Figure 5.1. The atria and ventricles are divided by atrioventricular valves, while the left and right ventricles are separated by the ventricular septum. The left ventricle is linked to the aorta through the aortic valve, and the right ventricle is connected to the pulmonary artery through the pulmonary valve [220].

In a healthy individual, the heart's electrical and mechanical activities follow a specific pattern. It starts with an electrical signal, the depolarization wave, originating in the right atrium, leading to atrial contraction (P wave on the ECG). This atrial contraction is known as atrial systole. Following this, the depolarization of the right and left ventricles (marked by the QRS complex on the ECG) triggers their contraction, initiating ventricular systole. Repolarization of the ventricular muscle cells occurs in two phases, spanning from the end of the QRS complex to the end of the T wave. The cardiac cycle is completed with the T wave. Because the ventricles are larger and depolarize more quickly than the atria, their contraction during ventricular systole is more forceful and rapid [220]. The key stages of the cardiac cycle and their alignment with ECG waves are illustrated in Figure 5.2.

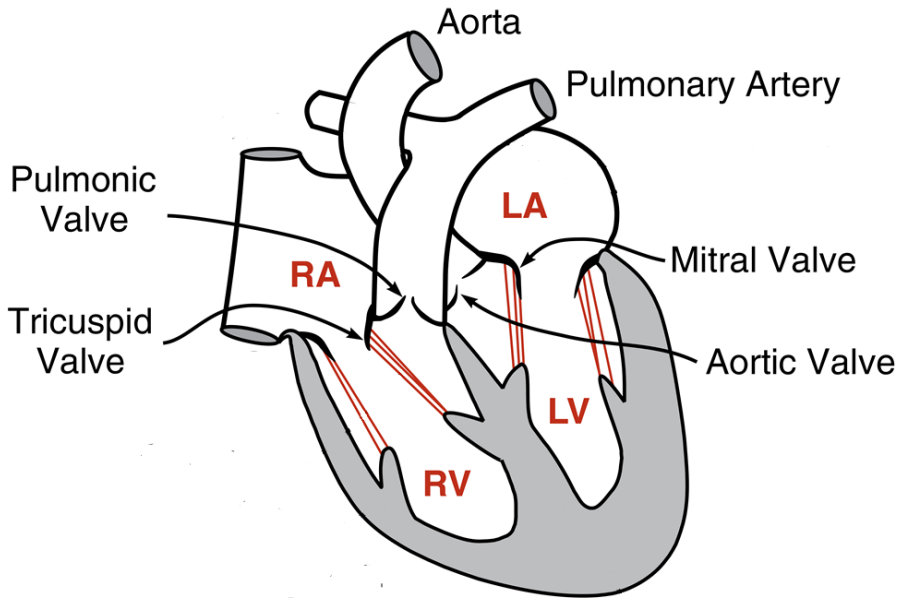

Figure 5.1: Anatomy of the heart.

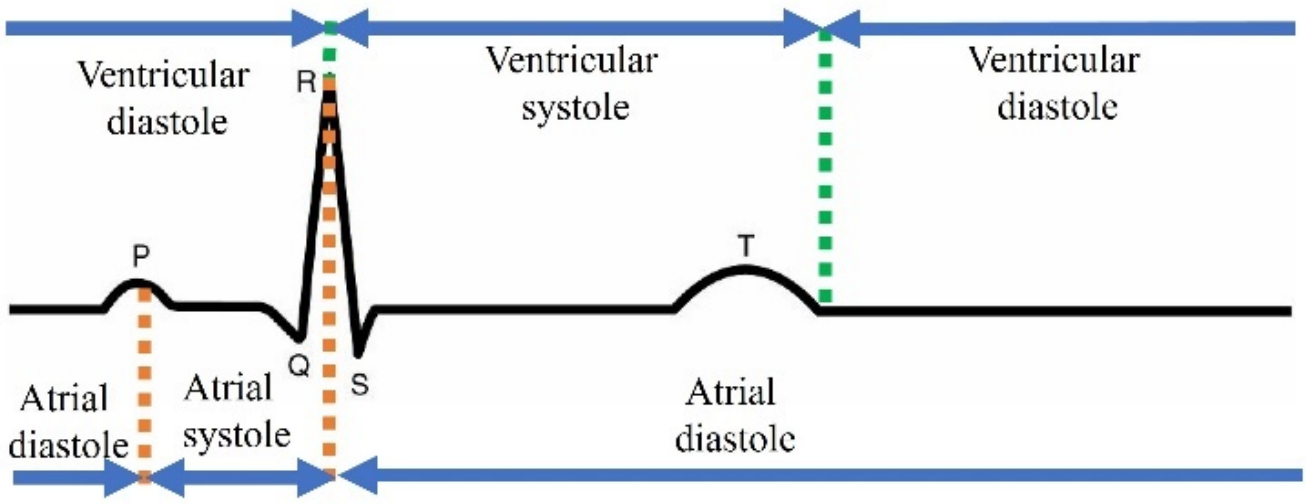

Figure 5.2: ECG waves and their relation to the cardiac cycle.

5.3 Signal and System Design to Estimate the Heart Waveform.

5.3.1 Signal Design

In this section, the designed signal in 3.2.4 is used. The primary alteration lies in the number of chirps, directly impacting signal quality. Given the gradual nature of breathing and heart movements, the reflected

chirps within a frame exhibit high similarity. Therefore, by averaging all chirps within a frame, signal phase noise can be enhanced. In this study, a configuration of 32 chirps per pulse was adopted.

5.3.2 Undesired Harmonics and Body Movement Effects

The first step in accurately monitoring heart waveform is to understand other movements, including breathing and body movements. Firstly, it is necessary to estimate BR since breathing harmonics could be stronger than heart waveform components. If the strongest harmonic in the heart frequency band, which is 0.8 Hz to 6 Hz, is an integer multiple of the BR frequency, it should be disregarded. In addition, the intermodulation harmonics can be generated because of the non-linear relation between breathing and heart displacements. These components are not stronger than the heart waveform since the effect of each displacement is based on the Bessel function of the first kind, which is less than one [221].

Secondly, body movements have a direct effect on the measurement of breathing and heart waveforms. Since these movements usually have greater displacements than breathing and heart displacements, they can spoil human vibration signals in the frequency domain. Figure 5.3 shows the effect of torso movements on the unfiltered vibration signal when the radar is behind a seat. As can be seen in Figure 5.3(a), the body movement effect resembles a narrow, strong pulse. Therefore, its frequency response resembles a sinc function which has strong low-frequency components. These low-frequency components can make BR and HR estimations difficult. In addition, since it has a strong amplitude, it can generate strong high-frequency components that might affect the estimated heart waveform as well. Figure 5.3(b) and Figure 5.3(c) show positive and negative DC offsets, respectively. These DC offsets can affect all the frequencies and can make BR, HR, breathing waveform, and heart waveform estimations incorrect.

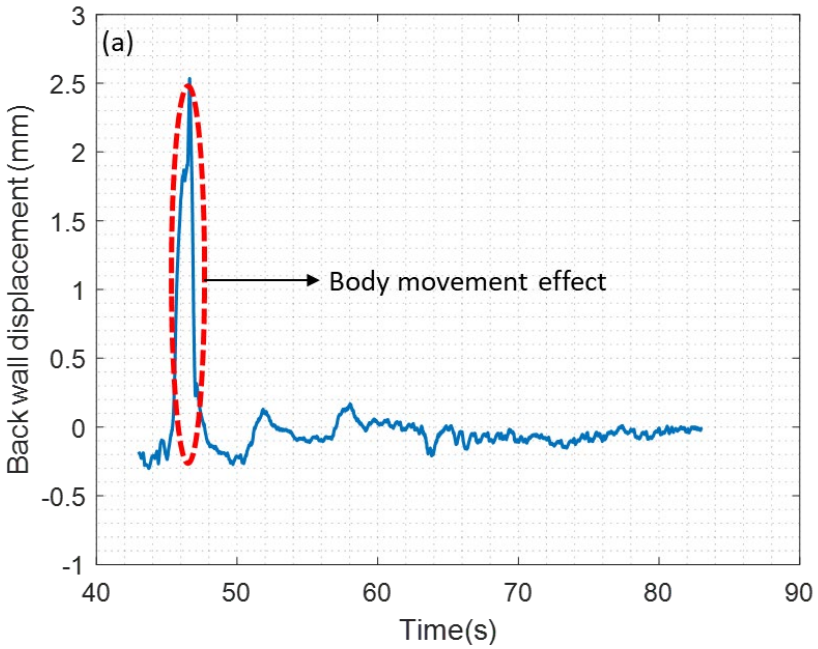
(a)
Back wall displacement (mm)
Time(s)
Body movement effect
3
2.5
2
1.5
1
0.5
0
-0.5
-1
40
50
60
70
80
90

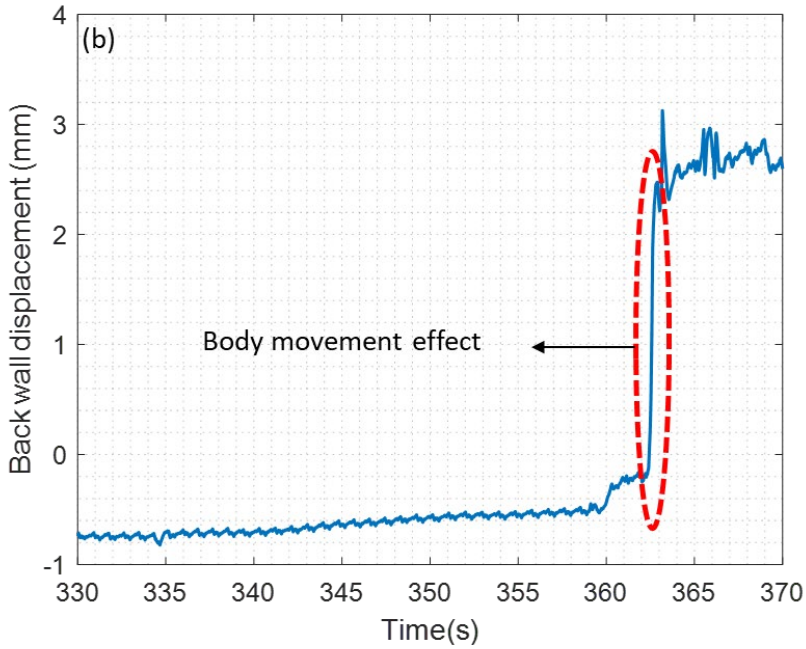
(b)
Back wall displacement (mm)
Time(s)
Body movement effect
4
3
2
1
0
-1
330
335
340
345
350
355
360
365
370

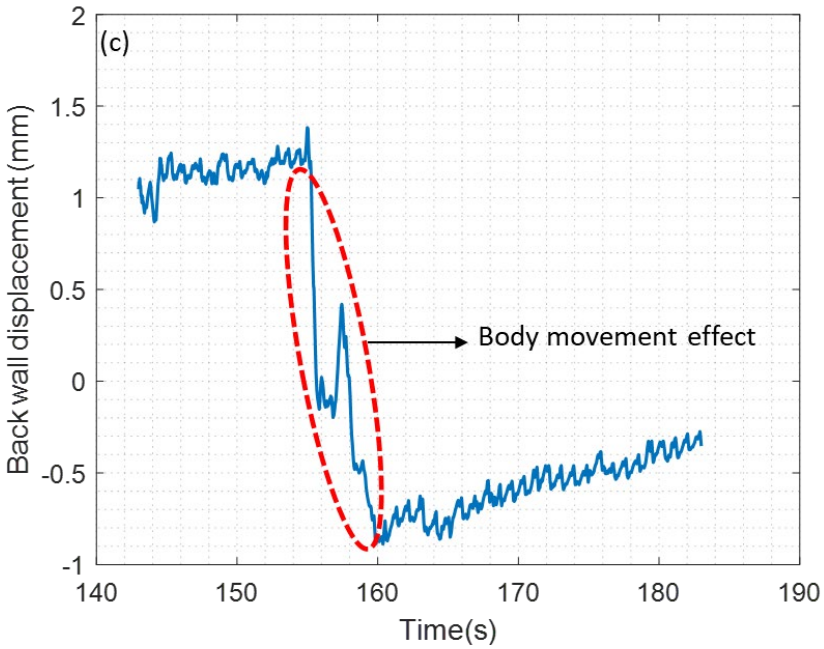

Figure 5.3: Torse movements impact on the unfiltered vibration signal: (a) strong pulse, (b) positive DC offset, and (c) negative DC offset.

Figure 5.4 depicts the STFT of different activities in which the signal is filtered by a high pass filter with a cutoff frequency of 0.1 Hz. In all the measurements except sitting, the participant was breathing. Normal and deep breathing does not exhibit significant high-amplitude components, as demonstrated in Figure 5.4(a) and Figure 5.4(b), respectively. However, other activities in which the torso moves forward or backward have high-amplitude displacement and can make strong frequency components, especially in lower frequencies. Therefore, body movements can distort breathing and heart displacements. As a result, since these body movements cannot be mitigated by filtering and can affect BR and HR estimations, they should be compensated in the time domain. By taking a derivative from an unfiltered signal and setting a threshold for the spikes, those spikes can be detected and compensated. The threshold can be determined by studying different participants with different BRs and depths.

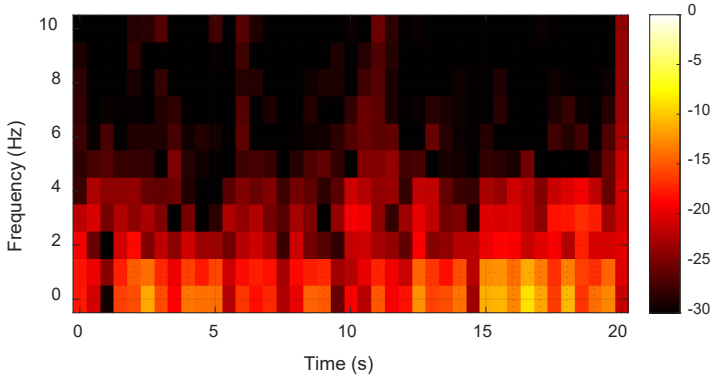

(a) Normal breathing

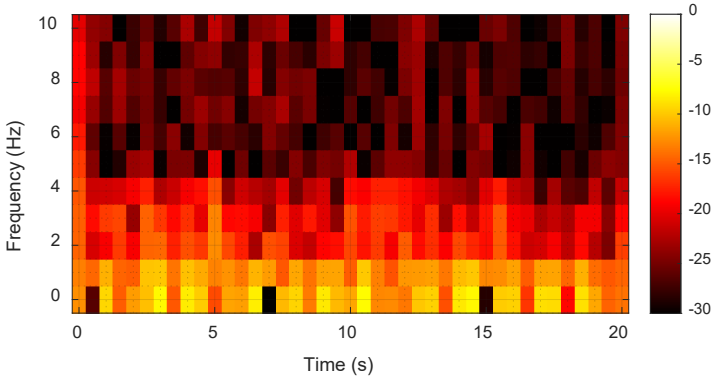

(b) Deep breathing

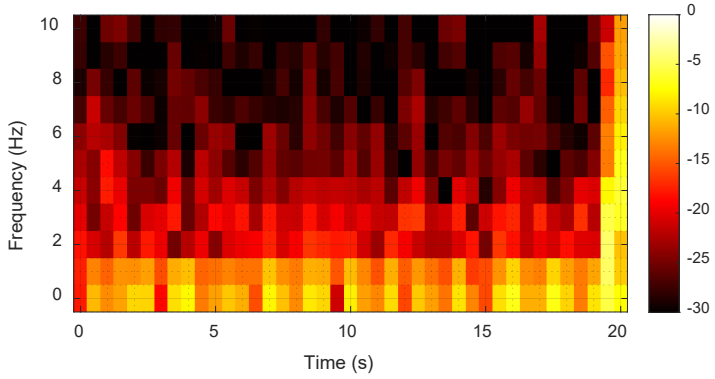

(c) Standing

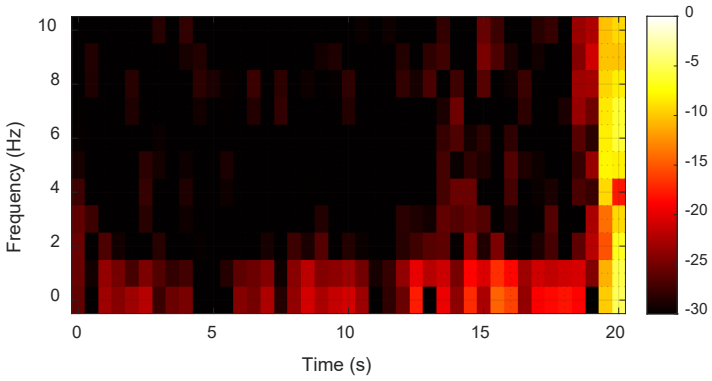

(d) Sitting

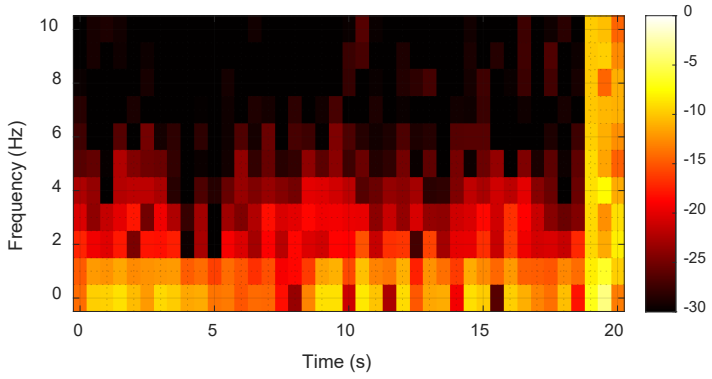

(e) Torso movements

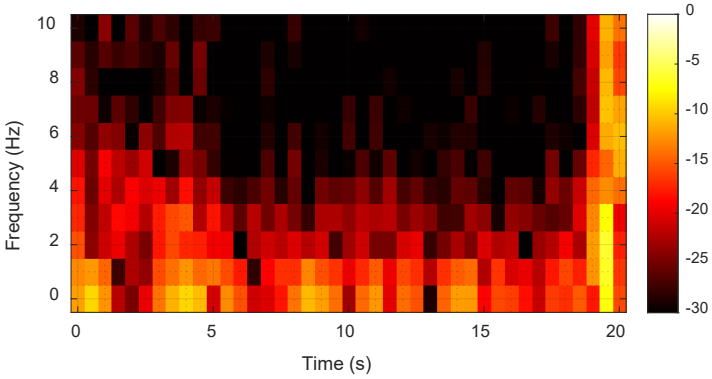

(f) Random body movements

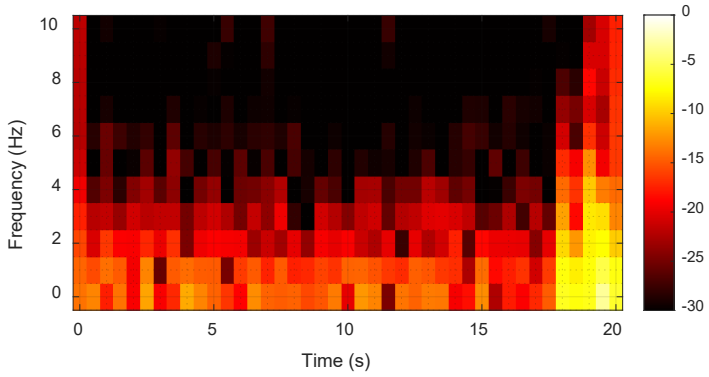

(g) Hitting the chair

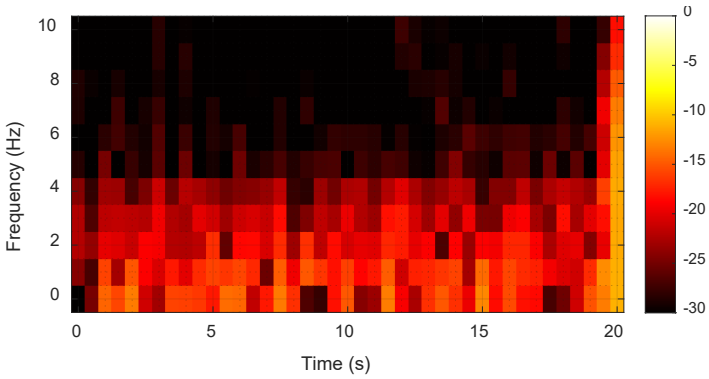

(h) Swinging the chair

Figure 5.4: The STFT of different activities in which the signal is filtered by a high pass filter with a cut-off frequency of 0.1 Hz: (a) normal breathing, (b) deep breathing, (c) standing, (d) sitting, (e) torso movements, (f) random body movements, (g) hitting the chair, and (h) swinging the chair.

5.4 Smart Home Monitoring

5.4.1 Signal Processing Chain to Reconstruct Heart Waveform.

Figure 5.5 depicts the signal processing chain used to reconstruct heart waveforms from human body vibrations. In this thesis, after DC removal and fast-time FFT, multiple range bins are employed to reconstruct the heart waveform. Since the torso width is more than 40 cm for adults [205] and the radar is placed in the middle of the back, 6 range bins (from range bin number 4 to 9) are chosen, considering a 3 cm range resolution [222]. Then, the phase of each bin is extracted to reconstruct body vibrations. Due to the high amplitude of human body vibrations in comparison to wavelength, which is almost 5 mm, it is necessary to unwrap the phase. In the next step, body movements should be detected and compensated.

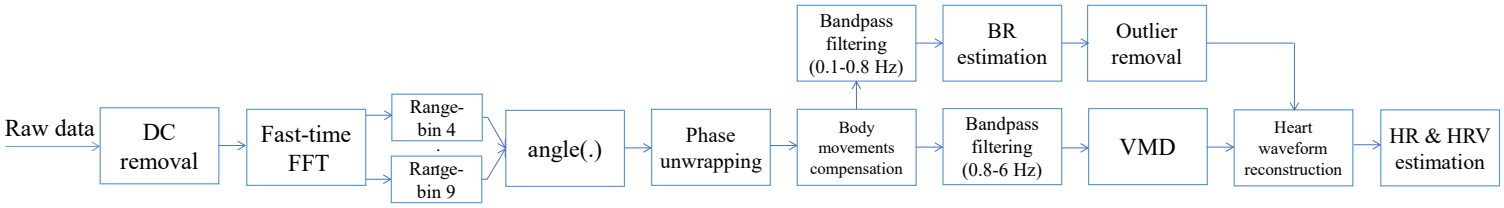

Figure 5.5: The signal processing chain to reconstruct heart waveform from human body vibrations.

Multiple steps should be taken to mitigate the high amplitude body movements in the time domain, as provided in Algorithm 1. Firstly, the derivative of the signal is taken to find spikes in the vibration signal. In the next step, a threshold is used to determine the spikes in the signal. The threshold level determination needs to be done statistically by collecting data from different participants. These participants were asked to breathe shallowly and deeply while seated. Approximately 300 measurements were collected from a group of 4 participants to estimate statistical parameters. The threshold level based on the empirical rule [207] is determined to be 0.48 mm/sample. If the amplitude of the differentiated movement is more than this threshold, the derivative of the signal is set to zero. Finally, the cumulative sum reconstructs the body vibration signal with compensated body movements.

Algorithm 1: Body movements compensation algorithm

Input: Body Vibration Signal After Phase Unwrapping
Output: Body Vibration Signal with Compensated Movements

Derivative Signal = Derivative of Input
for counter = 0 to Length of Derivative Signal
    if Derivative Signal (counter) > Threshold:
        Derivative Signal(counter) = 0

return Cumulative Summation of Derivative Signal

Algorithm 2: Heart waveform reconstruction

Input: IMFs from VMD and estimated BR
Output: The Reconstructed Heart Waveform

```
Derivative Signal = Derivative of Body Vibration Signal
for i = 0 to Number of Remained Range Bins after Outlier Removal
    Heart_Waveform (i) = []
    for j = 9 to 0
        Selected_IMF = IMF (j)
        if   HR of Selected_IMF != integer   multiple of BR
            HR = HR of Selected_IMF
            Heart_Waveform (i) = Selected_IMF
            First_Harmonic = j
            break

    for k = First_Harmonic to 0
        Selected_IMF = IMF (k)
        if   HR of Selected_IMF != integer   multiple of BR and Rate
of Selected_IMF == integer multiple of HR
                Heart_Waveform (i) += Selected_IMF
Final_Heart_Waveform = sum (Heart_Waveform)
return HR and Final_Heart_Waveform
```

After body movement compensation, the body vibration signal can be used for BR, HR, and HRV estimations. Since breathing waveform is the second interferer after body movement compensation for heart waveform reconstruction, breathing waveform should not be involved in heart waveform reconstruction. Due to the periodic nature of breathing, BR estimation can determine breathing harmonics. Therefore, the body vibration signal without body movements is filtered by a bandpass filter from 0.1 Hz to 0.8 Hz. In addition to this human body movement compensation, an outlier removal is applied to remove distorted range bins as 3.2.

To estimate HR and HRV, the main harmonic of the breathing waveform can be filtered by a band pass filter from 0.8 Hz to 6 Hz. A narrower bandpass filter removes heart waveform details. However, higher frequency harmonics of breathing waveform still can interfere with heart waveform, especially during deep breathing. VMD approach can be employed to decompose different harmonics after bandpass filtering. In this thesis, the filtered signal is decomposed into 10 intrinsic mode functions (IMF). The strongest IMF, which is not an integer multiple of BR, is the main harmonic of the heart waveform. As was discussed earlier, nonlinear harmonics generated from breathing and heart displacements cannot be stronger than the main harmonic of the heart. If the higher harmonics of the heart waveform are not an integer multiple of BR, they can be used for heart waveform reconstruction. The heart waveform should be reconstructed by at least two harmonics. Otherwise, the heart waveform cannot be reconstructed. Finally, HRV can be estimated based on the reconstructed waveform. In this thesis, HRV metrics, such as the root mean square of successive differences (RMSSDs), the standard deviation of the RR interval (SDRR), and the percentage of successive IBIs that differ by more than 50 ms (pNN50) are derived [154]. Algorithm 2 provides the heart waveform reconstruction.

5.4.2 Experimental Setup and Protocol

In this study, the BGT60TR13C radar module developed by Infineon is employed. This radar module operates at 60 GHz and can provide almost 5 GHz bandwidth. The overall dimensions of this radar package measure 64 mm x 25.4 mm [141]. Due to its compact size, this radar module can be integrated into smart furniture without causing any inconvenience to occupants.

The placement of the sensor has a significant impact on the radar's ability to accurately measure displacement. There are two key factors to consider in sensor placement. First, the angle and distance between the radar and the human body play a crucial role. Placing the radar in front of the displacement enables precise estimation because the radar measures radial displacements, and high-amplitude displacements are less susceptible to noise interference. Moreover, the radar equation shows that reflected power increases significantly with shorter distances to the fourth power, making radar measurements less susceptible to noise at close ranges. Therefore, for the most precise displacement estimates, it is advisable to position the radar in front of the displacement at the closest possible range.

Secondly, for individuals in a seated position, the radar can be placed either on the desk in front of the chest or behind the seat. The desk-mounted radar can effectively measure chest and abdomen wall displacements, which typically exhibit higher amplitudes compared to back wall displacement. However, it may be more susceptible to interference from other human body movements, such as hand and head

movements. In contrast, the seat-mounted radar operates at a closer range, resulting in a stronger signal-to-noise ratio. Furthermore, it offers a more stable setup compared to the desk-mounted radar, which can be easily altered due to its position on the desk. As a result, the use of seat-mounted radar technology for monitoring seated individuals proves to be a reliable choice.

Figure 5.6 illustrates the experimental setup for data collection. Participants were asked to sit on a chair and were given the option to either work with their laptops or take a rest. Figure 5.6(a) and Figure 5.6(b) depict a young subject and an elderly subject, respectively. Figure 5.6(c) depicts the experimental setup for the interference effect from wall radar with and without synchronization. To evaluate seat radar results, two different belts, including Frontier X for ECG data collection [223] as can be seen in Figure 5.6(d), and BioRadio piezo electric respiratory effort belt for respiratory data collection [224] as can be seen in Figure 5.6(e), are employed.

In the first data campaign, the accuracy of HRV and HR estimation are evaluated. Eight healthy subjects (four females and four males; age: 30 ± 11 years; weight: 70 ± 20 kg; height: 164 ± 14 cm) participated in these experiments. The duration of the main measurement was around 20 minutes. Additionally, body movement detection in human body vibrations is investigated in a separate measurement.

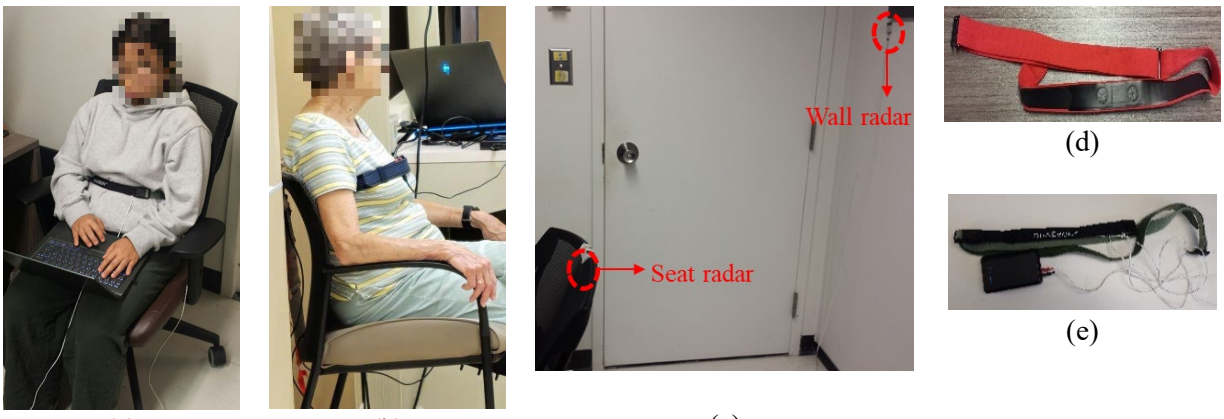

(a) (b) (c) (d) (e)

Figure 5.6: The experimental setup: (a) the participant is working with a laptop, (b) the participant is taking a rest, (c) the interference test setup in the presence of wall radar, (d) Frontier X for ECG data collection, and (e) BioRadio piezo electric respiratory effort belt for respiratory data collection.

In the second data campaign, the evaluation focused on studying the heart waveform in senior subjects with and without cardiac conditions. The subject group consisted of 15 subjects with an average age of

75 years (±5 years), average weight of 65 kg (±10 kg), and average height of 167 cm (±9 cm). These individuals actively engaged in the experiments while in a seated position, and the measurement duration was approximately 12 minutes. Notably, among these participants, five were identified with heart issues based on ECG data. Specifically, one participant exhibited tachycardia, while the remaining four had a prolonged QTc. The research ethics office at the university approved the study for data collection (ORE #: 43843).

5.4.3 Results and Discussion

5.4.3.1 Heart Waveform Verification

In this thesis, the investigations of radar signals measuring heart waveform indicate a periodic pattern on the skin. Figure 5.7 represents a heart waveform filtered from 0.8 Hz to 3 Hz in a breath-hold period, synchronized with ECG data. In this measurement, the radar is placed in the middle of the back of the seat, and its z-height is equal to the heart's height. Based on [132], it is concluded that T waves correspond to valleys in radar displacements after synchronization, which is compatible with the findings in this thesis. Figure 5.7 also shows that P-waves can correspond to the peak value of displacements. However, wider bandwidth might be required for more details [149].

Figure 5.8 represents the heart waveform filtered from 0.8 Hz to 6 Hz while the radar is located behind the seat and has the same height as the heart during a breath-hold. Each heart cycle by radar signals has two sequential peaks and one valley. If valleys correspond to T waves, the second peaks correspond to P-waves. Furthermore, when the participant is in a seated, calm state, the second peak is predominantly stronger than the first peak. However, when the radar is located on the chest and attached to the shirt by adhesive tape, the second peaks do not correspond to P-waves in the heart waveform with the same filtering as can be seen in Figure 5.9. Additionally, the investigation into the influence of radar height revealed that similar heart waveforms are obtained when the radar height is within the range of HH +5 to HH -10, where HH represents heart height.

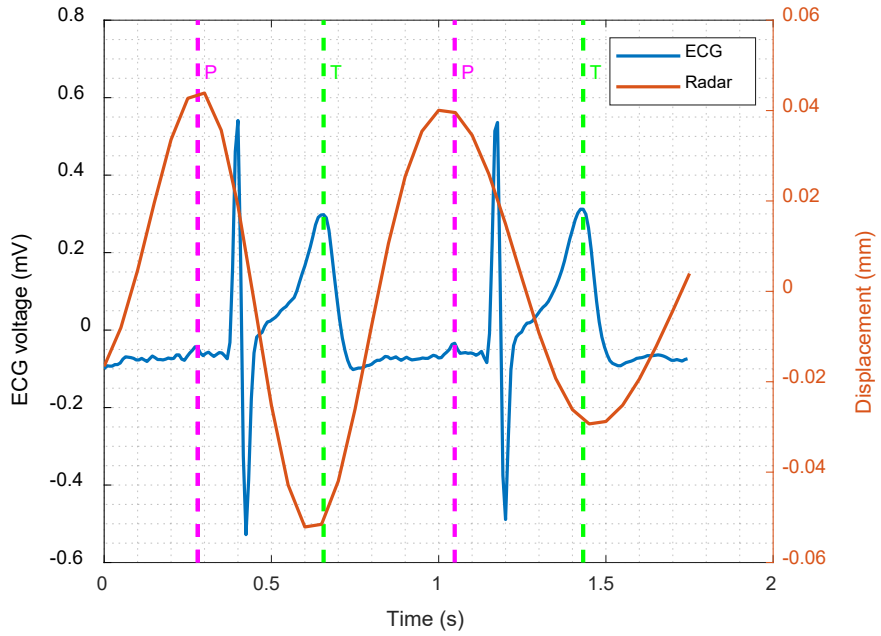

Figure 5.7: Heart waveform filtered from 0.8 Hz to 3 Hz in a breath-hold period compared with ECG data. The green and pink dashed lines correspond to T and P-waves, respectively.

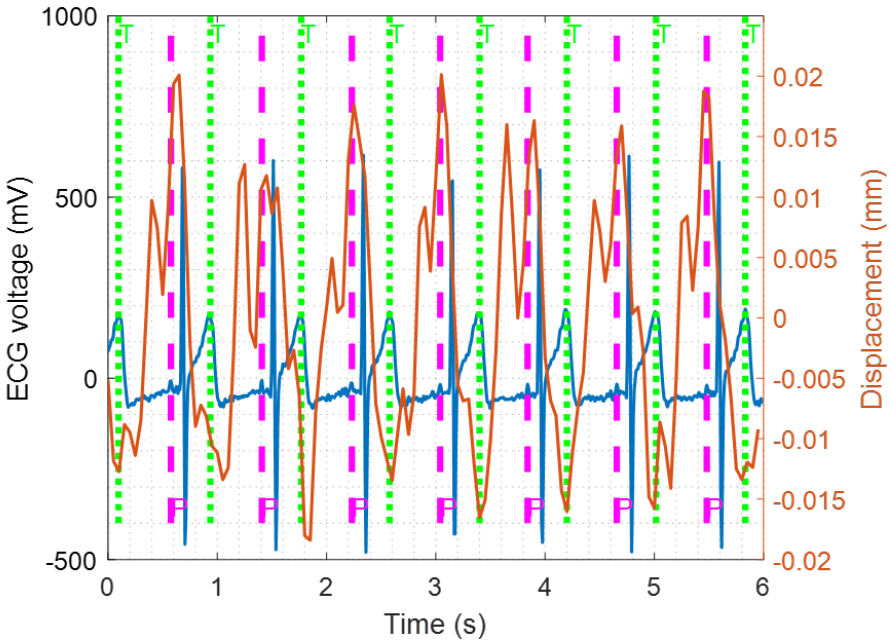

Figure 5.8: The heart waveform filtered from 0.8 Hz to 6 Hz while radar is located behind the seat and has the same height as the heart during a breath-hold. The green and pink dashed lines correspond to T and P-waves, respectively.

Figure 5.10 represents the heart waveform of a participant during a breath-hold after a jugging while the radar is located behind the seat at almost the same height as the heart. The heart waveform pattern resembles that of a calm state, although HR is 98 beats per second. However, the first peak is mostly stronger than the second peak in the heart displacements. In addition, the amplitude of the heart waveform is almost 7 dB greater than during a calm state, which is a physiological response to physical activities. Furthermore, P-waves in this measurement do not correspond to the second peak when T waves are aligned with valleys. As a result, while the heart waveform is a quasi-periodic signal, its valley can be reliably used for HRV estimation in different radar locations.

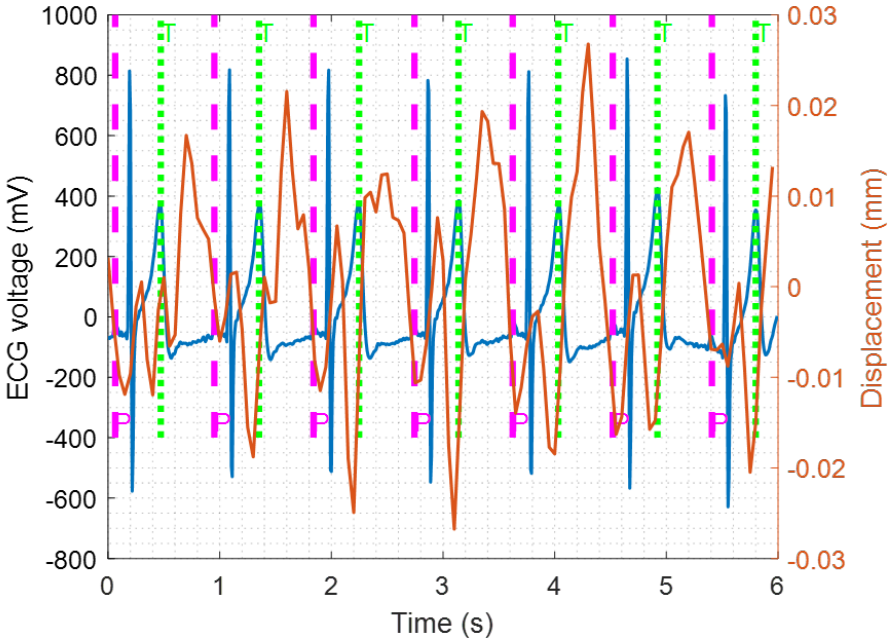

Figure 5.9: The heart waveform filtered from 0.8 Hz to 6 Hz while radar is located on the chest and attached to the shirt by an adhesive tape and has the same height as the heart during a breath-hold. The green and pink dashed lines correspond to T and P-waves, respectively.

5.4.3.2 Validation of the Radar Setup

Figure 5.11 represents BR estimation by seat and desk radars. In this scenario, the participant is asked to follow an online metronome [209] for different BRs, including 9, 12, 15, and 17, while the participant did not have body movements. These BRs cover normal and abnormal range of BRs. Between two different rates, there is a 20 to 30-second breath-hold period in which BR drops during a breath-hold period and displacement is less than 0.15 mm [222]. Table 5-1 compares the average RMSE of BR estimation for both

radars. The results indicate that both radars have average RMSE of less than 1.12, while the seat radar is slightly better than the desk radar in various BRs. However, body movements like head and hand movement can affect BR and HR estimations in desk radar more than seat radar. Furthermore, the estimated back wall displacements are less than chest wall displacements. Therefore, they might be affected by phase noise.

Figure 5.12 compares synchronized desk and seat radar results with ECG data for HR estimation. Both radars can track HR when there is no body movement. However, when there are head and hand movements, which are quite possibly happening for seated people, the desk radar is affected more than the seat radar. As can be seen in Figure 5.12, desk radar estimations for HR spikes incorrectly when there are body movements. However, seat radar is not affected by hand and head movements and can track HR accurately. The average absolute error for the desk and chair radars are 7.9 beats and 4.1 beats, respectively. However, it cannot compare these two radars in terms of false estimations made by body movements. As a result, using radar behind the seat might reduce some kinds of body movement effects like head and hand movements.

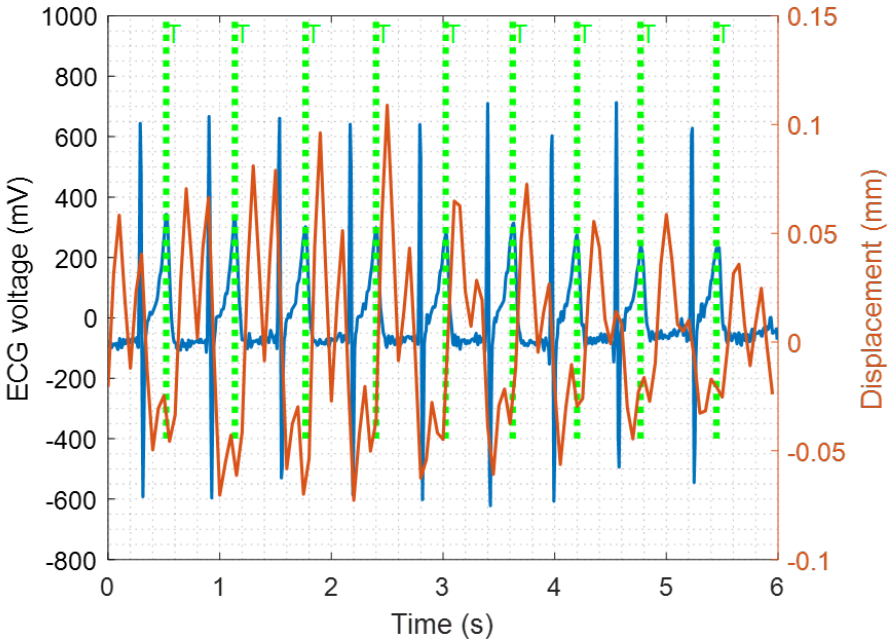

Figure 5.10: The heart waveform of a participant during a breath-hold followed an exercise, with the radar positioned behind the seat at chest height. The green dashed lines correspond to T-waves.

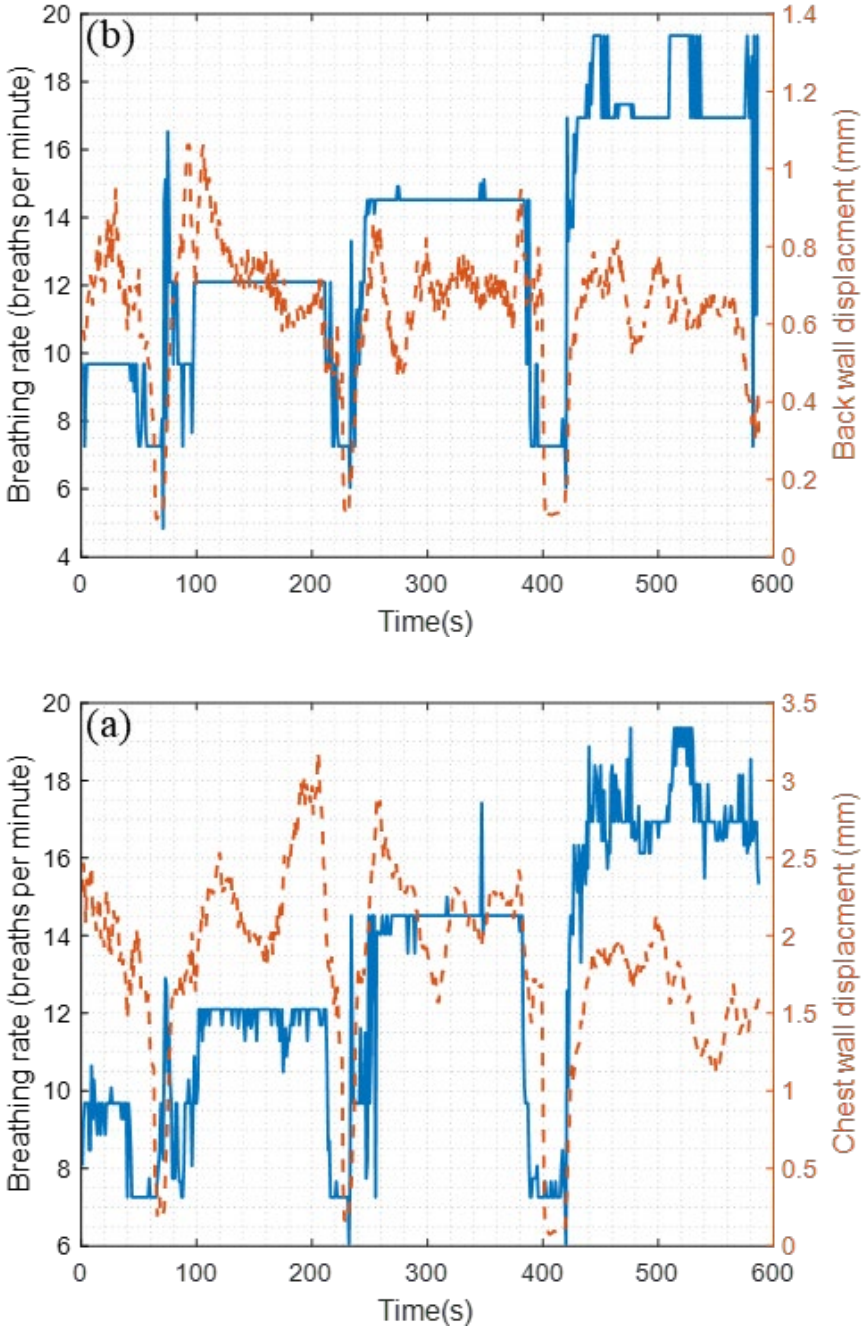

Figure 5.11: BR estimations were conducted using a dual radar setup at various BRs, including 9, 12, 15, and 17, under conditions where the participant remained without significant body movements: (a) desk radar and (b) seat radar.

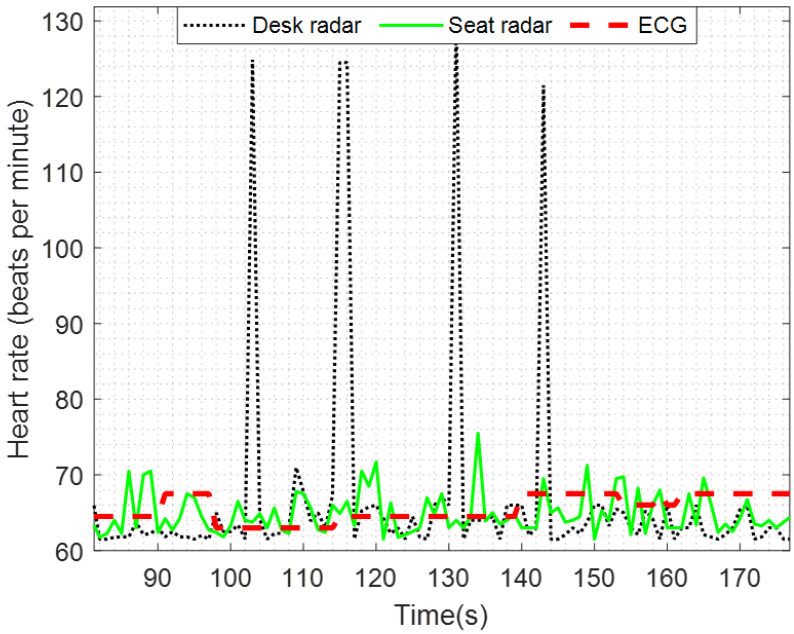

Figure 5.12: The comparison between the desk and the seat radars estimations for HR estimation based on ECG results.

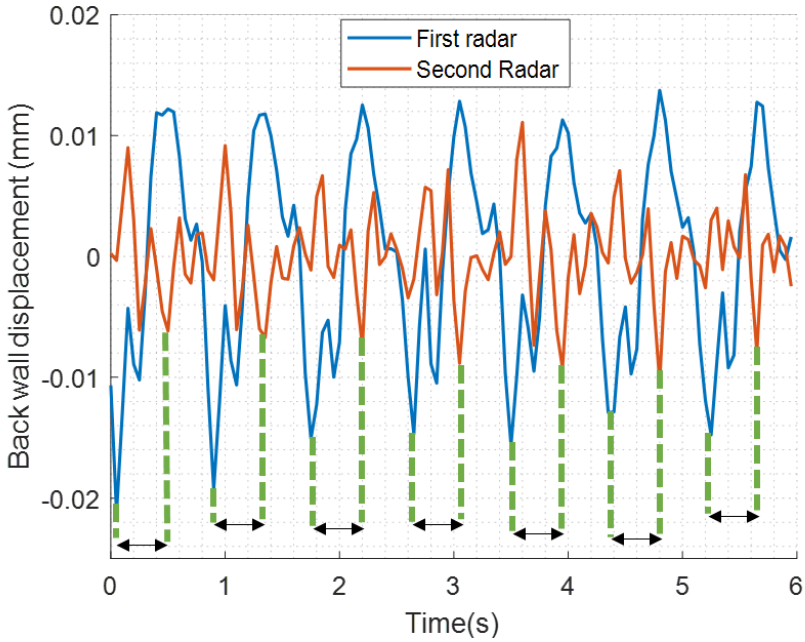

Figure 5.13: Comparing heart waveforms captured by two synchronized radars from different positions, one situated at the heart height and the other behind the participant's waist.

Figure 5.13 compares heart waveforms resulting from two synchronized radars from behind the seat when there is no interference between them. The first radar is located at the same height as the heart. The second radar is located behind the participant's waist. The second radar results are almost different from the first

radar. Firstly, the valleys in the second radar are not strong enough to be reliably used for HRV estimation, and the amplitude of displacement is also lower than that of the first radar. Secondly, the second radar results are less quasi-periodic. However, the time distance between the valleys of the first and the second radars remained constant.

One of the challenges in using radars is the effect of interference when there are a couple of radars in smart homes. In this thesis, the effect of interference is evaluated by a dual radar setup, including seat radar and wall radar as can be seen in Figure 5.6(c). In the first experiment, the wall radar is blocked by a metallic sheet to have minimum effect from this radar on the seat radar while radars are sending signals without a time delay. In the second experiment, the wall radar is not blocked by a metallic sheet, and the time delay between radars is also zero. In the final experiment, radars are working with a 5 ms delay while the wall radar has not been blocked by a metallic sheet. This delay is almost two times the actual timing of a frame in each radar. Therefore, radars are separately sending signals in the time domain to have less interference effect. The average power in zero Doppler in the second experiment is 0.7 dB greater than in the first experiment. However, the power difference between the first and the last experiments is almost zero. As a result, this time delay configuration can solve interference issues in smart home monitoring when multiple radars operate at the same carrier frequency simultaneously.

Table 5-1: The average RMSE of BR estimations in different BRs for desk and seat radars.

BR	Desk radar average RMSE (breaths per minute)	Seat radar average RMSE (breaths per minute)
9	1.12	0.81
12	0.35	0.12
15	0.57	0.47
17	0.85	0.65

5.4.3.3 Validation of the Proposed Algorithm

Figure 5.14 represents seat radar results in different range bins for HR estimation. The seat radar estimation is based on these 4 range bins. Therefore, false estimations might be removed by using an outlier removal algorithm. However, using a single range bin could be affected by random body movements. Since the human body captures more than one range bin when the radar is close to the human body, especially behind the seat, using multiple range bins can improve HR and heart waveform estimations.

Figure 5.15 compares the phase noise of a single chirp and averaged chirps in a frame. By taking an average of 32 chirps in a frame, the phase noise is suppressed by almost 10 dB. Since breathing displacements are much stronger than phase noise, using a single chirp can estimate displacements [124]. However, the heart waveform might be affected by the phase noise of a single chirp. As seen in Figure 5.12, heart displacements reach 0.02 mm, which could be affected by phase noise. As a result, using an average of multiple chirps in a frame can effectively improve heart waveform estimations.

Figure 5.16 depicts the heart displacement harmonics of a participant during a breath-hold while the radar is located behind the seat at almost the same height as the heart. The lower and upper cut-off frequencies of the bandpass filter are 1 Hz and 3 Hz, respectively [225]. The estimated HR based on the radar results is 108 beats per second. However, the actual HR based on the ECG data is 55 beats per second. It seems that the estimated HR by radar is two times the actual value. Therefore, the first peak, which is the actual HR, is suppressed by the rising edge of the bandpass filter. As a result, it is necessary to reduce the lower cut-off frequency of the bandpass filter. In this thesis, the bandpass filter was applied from 0.8 Hz to 6 Hz.

Figure 5.17 shows different IMF results, with the participant having shallow breathing and the BR having 17 breaths per minute. Therefore, the strongest IMF, which is also the lowest frequency component, results from heart displacements. As a result, the HR is 60 beats per minute. The second harmonic of heart displacement is 120 beats per minute. Since this rate is not among the detected IMFs, it might be distorted by other harmonics. The third and fourth harmonics' rates are 180 and 240, respectively. IMF 5 and IMF 3 correspond for the third and the fourth harmonics rate, respectively. The reconstructed heart waveform based on this harmonic analysis is shown in Figure 5.18. The valleys can be aligned with T waves. However, the waveform does not have two sequential peaks all the time, like during breath-hold. As a result, the reconstructed waveform during shallow breathing can estimate HRV based on the valleys.

Figure 5.19 shows different IMF results while the participant had deep breathing, and the BR was 17 breaths per minute. The strongest IMF, which is IMF10 resulted from the second harmonic of breathing vibrations since it is two times the actual BR. IMF 9 is the main harmonic of Heart displacements. The second harmonic of heart displacements is interfered with other harmonics and cannot be recovered. However, the third harmonic of Heart displacements is IMF4. The reconstructed heart waveform based on these harmonics is shown in Figure 5.20. The reconstructed heart waveform has two peaks. However, when valleys align with T-waves, P-waves do not align with the second peak. Therefore, during deep breathing, valleys correspond to T-waves and can be utilized for HRV estimation, like shallow breathing.

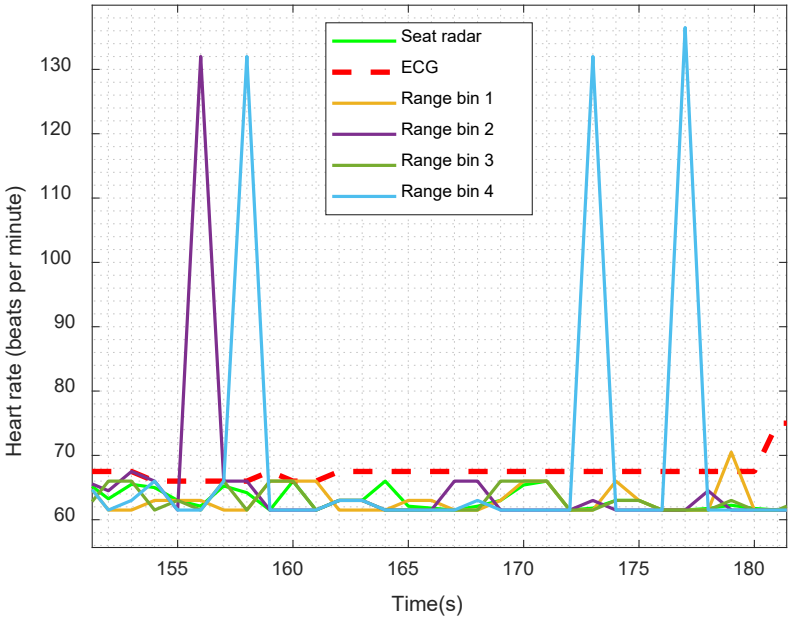

Figure 5.14: The comparison between the different range bins in the seat radar for HR estimation with ECG.

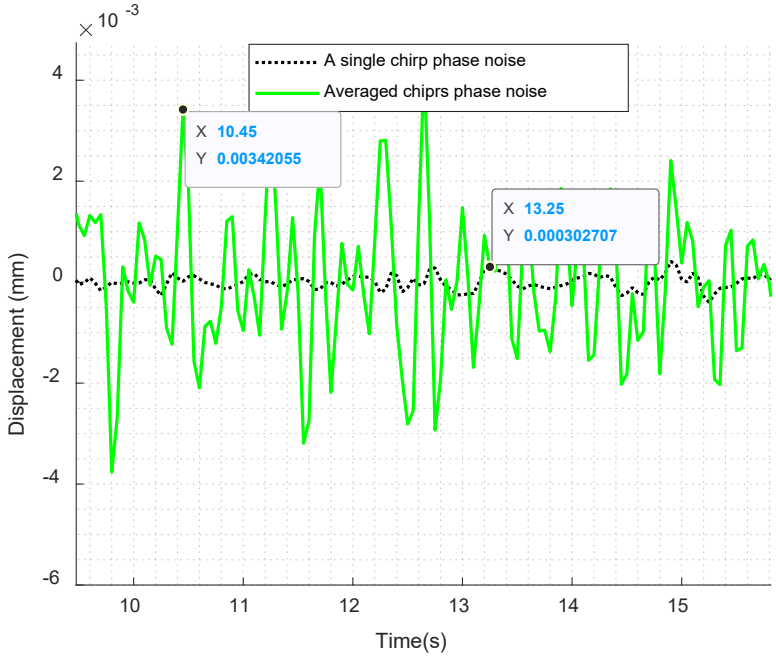

Figure 5.15: Comparison between phase noise of a single chirp and averaged chirps in a frame with 32 chirps.

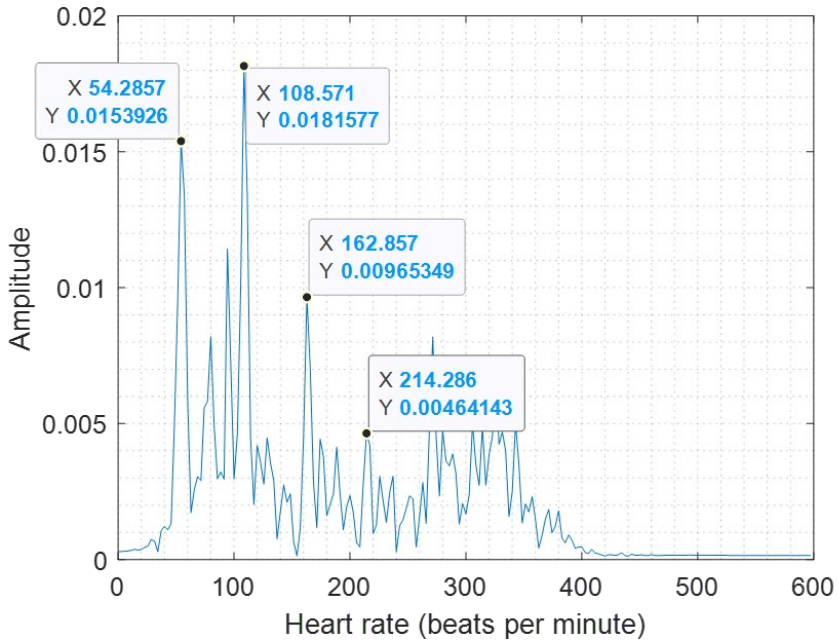

Figure 5.16: The heart displacements in the frequency domain during the breath-hold while the lower and upper cutoff frequencies of the bandpass filter are 1 Hz and 6 Hz, respectively.

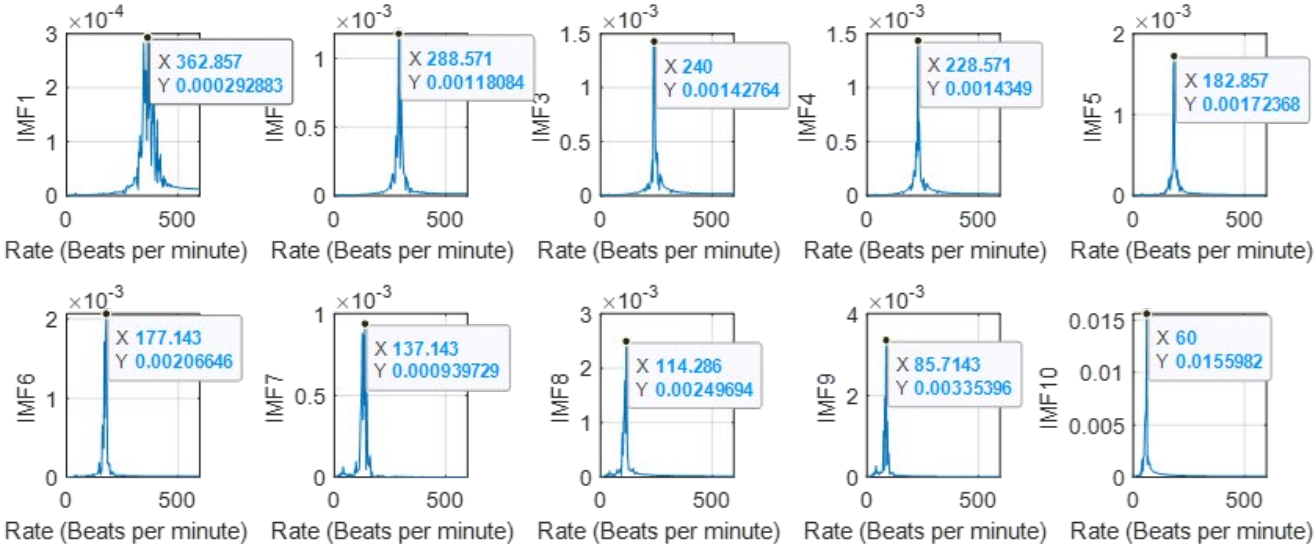

Figure 5.17: Different IMFs results while the participant had shallow breathing, and the BR was 17 breaths per minute.

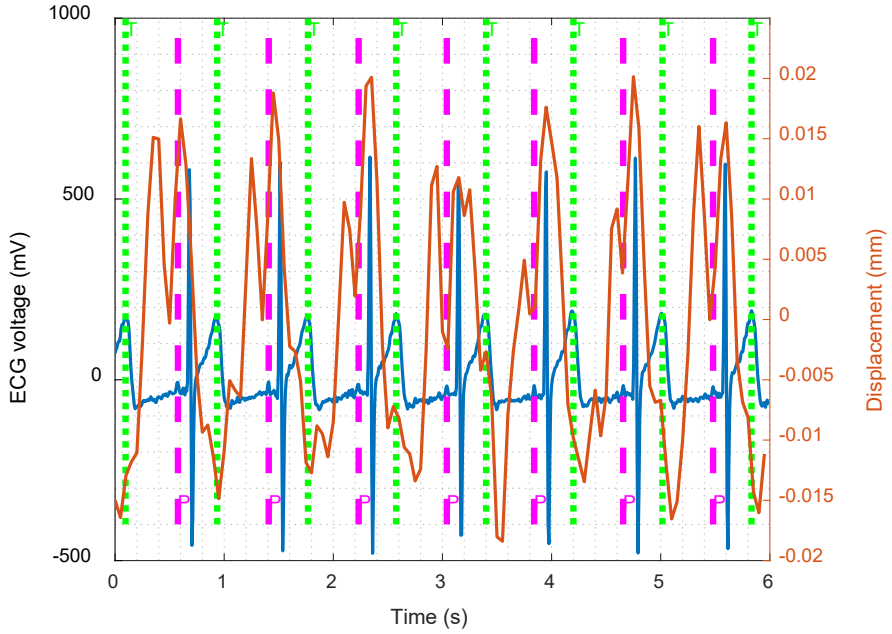

Figure 5.18: The reconstructed heart waveform based on the harmonic analysis compared with ECG data while the participant had shallow breathing, and the BR was 17 breaths per minute.

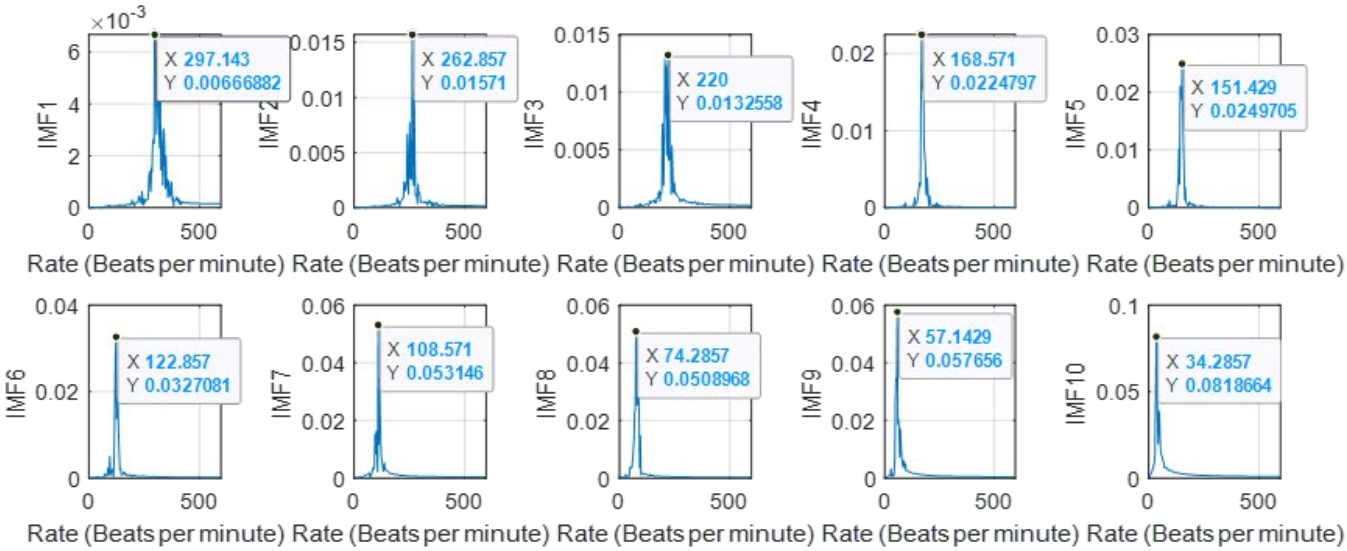

Figure 5.19: Different IMFs results while the participant had deep breathing, and the BR was 17 breaths per minute.

Figure 5.21 compares back wall displacements measured by radar from behind the seat before and after body movement compensation. As can be seen, body movements cause spikes in a short period. These spikes should be mitigated before heart waveform reconstruction. Otherwise, due to the strong amplitude, they spoil the breathing band and heart band. The proposed approach for body movement detection can effectively detect all body movements. Figure 5.22 depicts the body movement compensation effect on BR estimation when the actual BR is 24. As can be seen, due to the body movements, the estimated BR drops to almost 10 breaths per minute. Table 5-2 compares the average RMSE of BR for different BRs during the body movements. As can be seen, when BR is high, the average RMSE of BR increases significantly.

Table 5-2: The average RMSE of BR estimations in different BRs during the body movements.

BR	Average RMSE (breaths per minute)
9	0.9
11	1.1
14	2.9
16	5.7
18	8.1
22	11.5
24	13.2

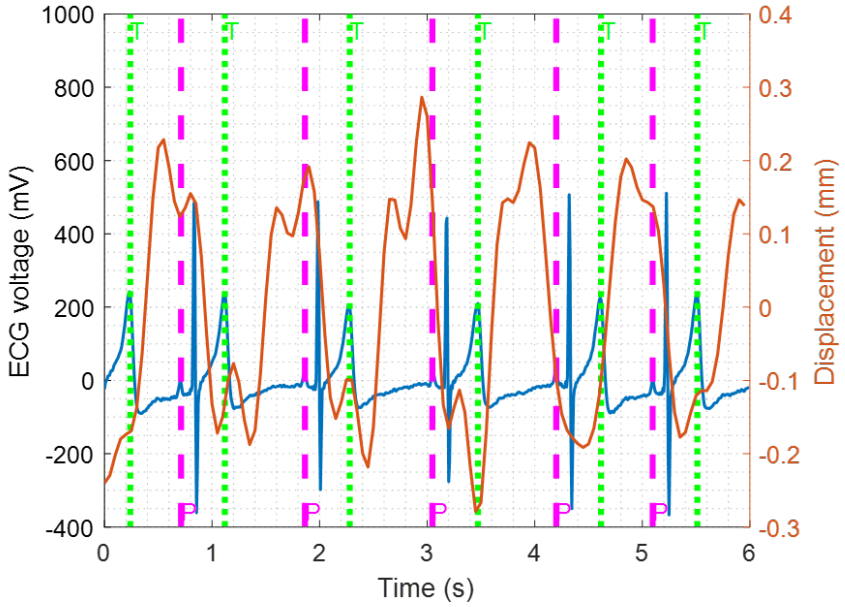

Figure 5.20: The reconstructed heart waveform while the participant had deep breathing and BR was 17 breaths per minute.

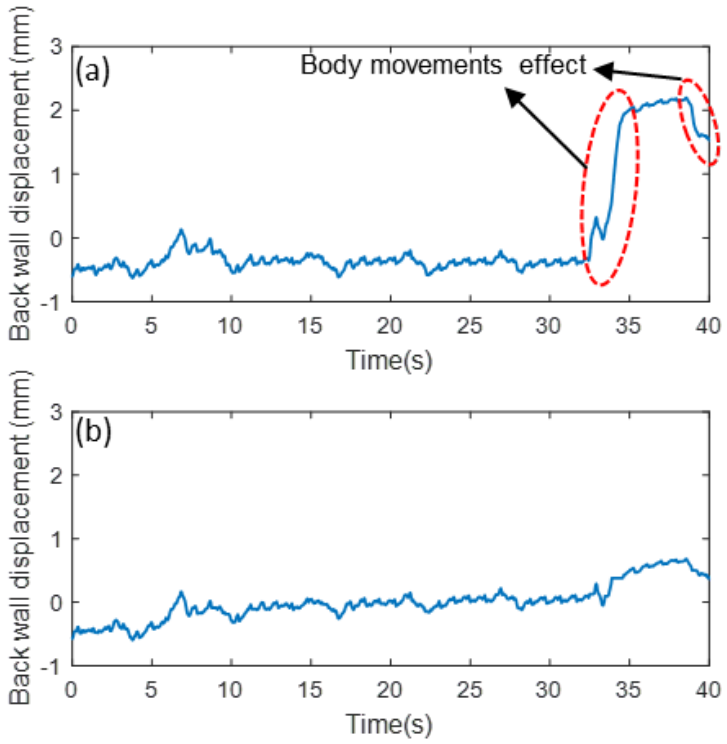

Figure 5.21: Displacements from behind the seat when radar has the same height as the heart: (a) before body movements compensation and (b) after body movements compensation.

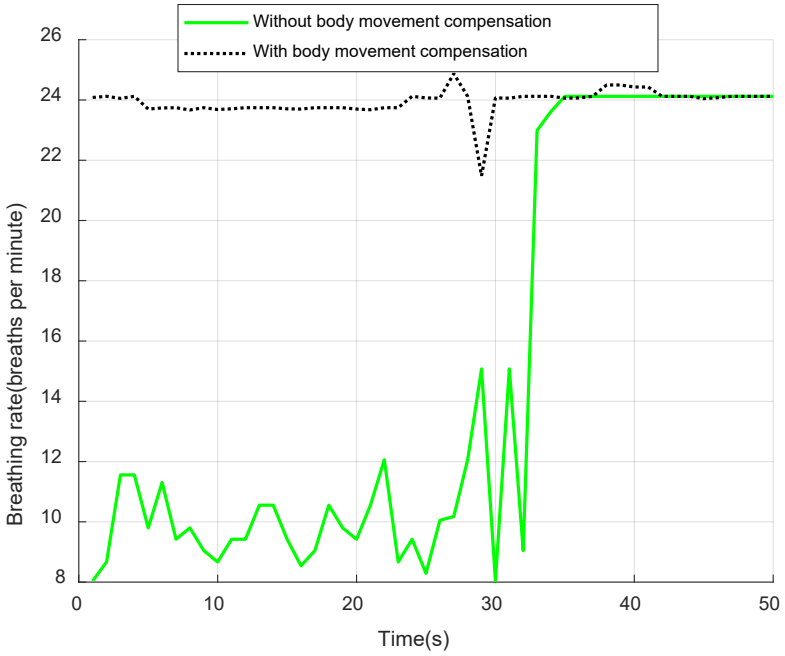

Figure 5.22: BR estimation when actual BR is 24 from behind the seat: (a) before body movements compensation and (b) after body movements compensation.

5.4.3.4 Heart Waveform in Subjects with Heart Conditions

Figure 5.23 depicts the heart waveform of a senior subject with tachycardia condition, resulting in an elevated HR even during periods of rest. As illustrated, the heart waveform displays two peaks followed by a single valley in each cycle, with a resting HR of 101 beats per minute. Healthy subjects exhibit a similar heart waveform, with a normal HR during rest. In addition, the first peak is stronger than the second peak, which is similar to healthy subjects' heart waveform after physical exercise.

Figure 5.24 illustrates the heart waveform of a senior subject with a prolonged QTc. The depicted waveform deviates from the typical pattern observed in healthy subjects, where two peaks are followed by a valley. In contrast, the subject with a prolonged QTc displays three peaks followed by a valley. This divergence from the norm suggests a potential heart condition. Therefore, variations in the derived heart waveform can serve as an indicator of underlying cardiac issues in comparison to the waveform observed in healthy individuals. Notably, all four subjects with a prolonged QTc have normal HR and HRV in these experiments.

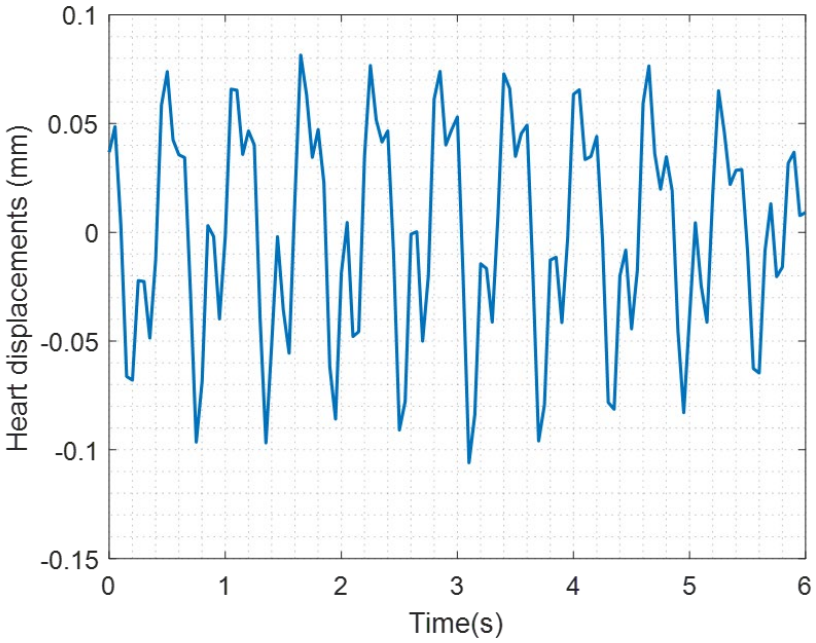

Figure 5.23: The heart waveform of a senior subject with tachycardia condition.

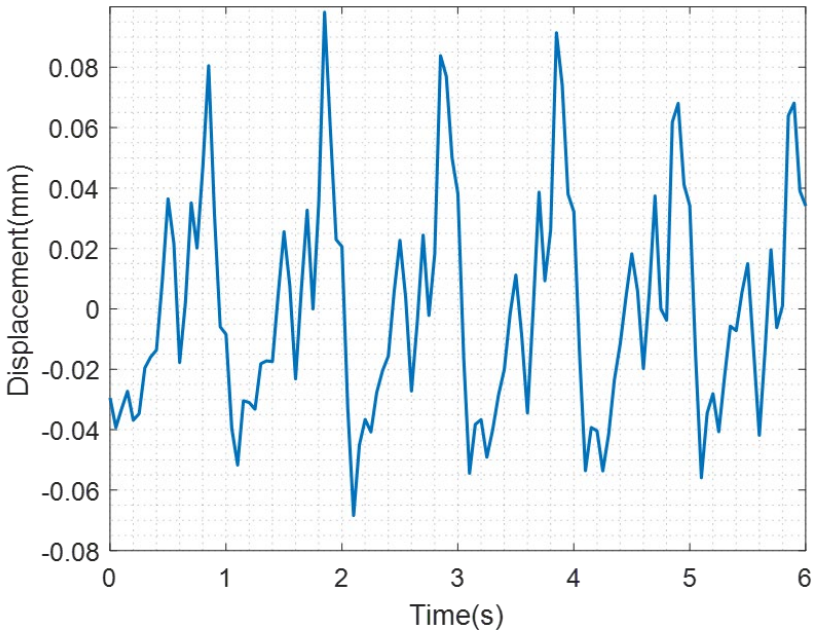

Figure 5.24: The heart waveform of a senior subject with a prolonged QTc condition.

5.4.3.5 Discussion

Figure 5.25 compares the impact of different signal processing methods on the absolute IBI estimation error. The pairwise comparisons using t-tests between the four methods revealed statistically significant differences, with all p-values less than 0.001. The combination of the multi-bin approach with VMD demonstrates a median error reduction of approximately 20 ms compared to the multi-bin approach without VMD. Notably, the maximum error also exhibits significant improvement, with a reduction of 57 ms. Additionally, the utilization of multiple bins also directly influences both the median and maximum IBI estimation errors. When VMD is also applied, there is an enhancement of approximately 8.2 ms in the median error and 20 ms in the maximum error. Furthermore, it is crucial to highlight that the 75th percentile error for the multi-bin approach combined with VMD remains below 50 ms. This finding underscores the effectiveness of the proposed method in this thesis.

To evaluate the proposed method's robustness across diverse users, Figure 5.26 depicts a comprehensive illustration of the distribution of absolute errors in IBI estimation for all eight participants. The findings reveal that the proposed method yields varying IBI estimation errors among different users, with median errors ranging from 17.5 to 42.8 ms. These variations can be attributed to a range of factors, including differences in individual physiological traits, such as body mass and variations in cardiac strength. Importantly, it is evident that the 75th percentile error for all participants consistently remains below 62

ms. In addition, Table 5-3 also compares the absolute estimation error of HR for all participants. The results indicate that the absolute relative error for HR estimation reached 4.8%. To assess the accuracy of HRV estimation,

Table 5-4 presents the estimated HRV metrics, including RMSSD, SDRR, and pNN50 for 8 participants. The results indicate that the proposed method achieves an average error of 6.1 ms for RMSSD, 6.7 ms for SDRR, and 6.3 % for pNN50. These observations underscore the method's resilience and effectiveness when applied to a diverse group of subjects.

Table 5-5 compares this study with recent publications across four criteria: body movement compensation, breathing harmonic cancellation, range bin sensitivity, and resultant outcomes. Emphasizing the necessity of addressing body movements and breathing harmonics in signal processing for realistic applications, the study highlights their significant impact on estimated vital signs. Additionally, the stability of radar integrated into furniture provides resilience against human manipulation, suggesting a reduced necessity for specific range bin selection in signal processing for the radar positioned behind the seat. The study's outcomes show reliable results based on HRV metrics and HR errors.

Table 5-3: The average absolute errors of HR estimations in different participants by the proposed method.

User ID	Relative error (%)
1	5.2
2	5.1
3	4.6
4	2.9
5	5.9
6	5.4
7	4.6
8	4.7

Table 5-4: HRV estimation errors in terms of RMSSD, SDRR, and pNN50 for 8 subjects.

Metrics	User ID							
	1	2	3	4	5	6	7	8
RMSSD (ms)	5.9	6.4	3.4	8.3	7.3	5.6	4.5	7.3
SDRR (ms)	11.2	5.8	3.8	7.6	6.5	7.2	5.3	6.5
pNN50 (%)	6.1	11.1	4.6	6.5	4.5	4.2	6.1	7.3

Table 5-5: The comparison between this study and the recently published papers based on four factors, including body movement compensation, breathing harmonic cancellation, sensitivity to range bin selection, and achieved results.

Ref	Body movement compensation	Breathing harmonic cancellation	Sensitivity to range bin selection	HRV metrics	HRV error	HR error (%)
[132]	No	No	Yes	NA	NA	NA
[149]	No	No	No	RMSSD	NA	2.42
[150]	No	No	Yes	SDNN, RMSSD, LF, and HF	NA	2.07
[151]	No	No	Yes	NA	NA	1.3
[152]	No	No	Yes	NA	NA	NA
[153]	No	No	Yes	LF and HF	NA	NA
[154]	Yes	Yes	Yes	Mean IBI, RMSSD, SDRR, and pNN50	3.89 ms, 6.43 ms, 6.44 ms, 2.55%	NA
[155]	Yes	Yes	Yes	SDNN and RMSSD	NA	NA
[156]	Yes	Yes	Yes	SDNN	6 ms	3
This study	Yes	Yes	No	RMSSD, SDRR, and pNN50	4.5 ms, 6.1 ms, 6.7 ms, 6.3 %	4.8

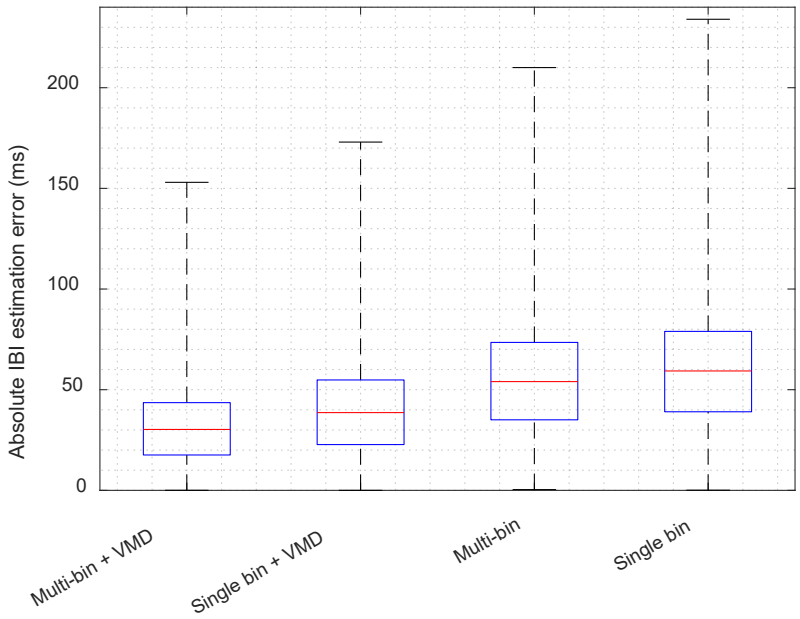

Figure 5.25: The impact of different signal processing approaches on the error in absolute IBI estimation.

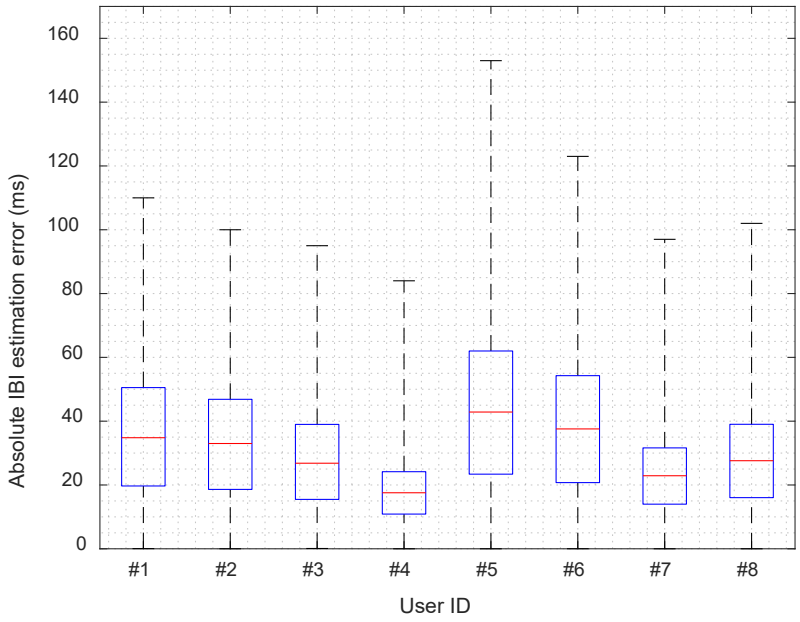

Figure 5.26: Influence of user diversity on the error in absolute IBI estimation.

5.5 In-Vehicle Heart Monitoring

In-vehicle heart waveform monitoring is a challenging task due to car body vibrations compared to smart home heart monitoring. Figure 5.27 illustrates the z-axis acceleration in the frequency domain up to 10 Hz. The predominant frequency of vibrations, approximately 1.5 Hz, poses challenges for heart waveform reconstruction. These vibrations are usually caused by road defects. Therefore, it is crucial to detect these sources of vibrations, particularly based on z-axis acceleration [226].

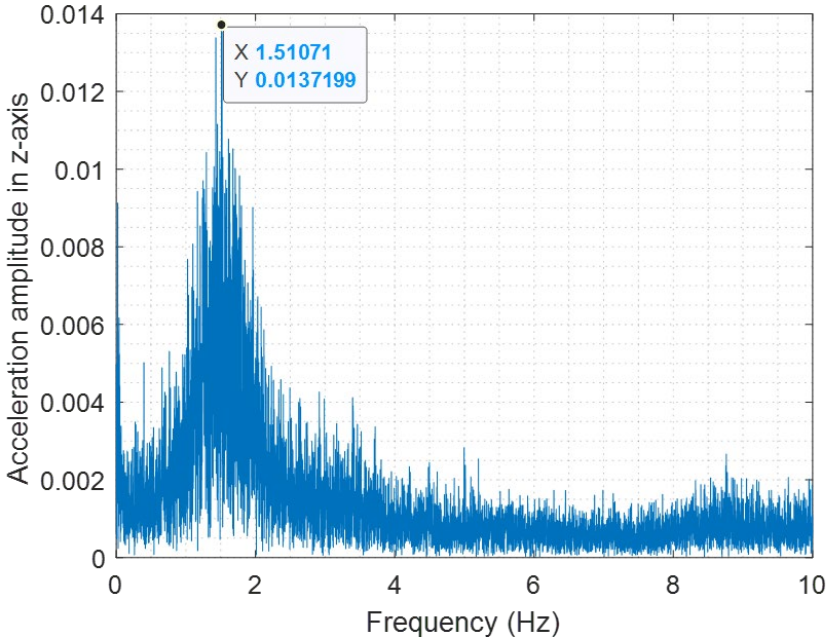

Figure 5.27: The z-axis acceleration in the frequency domain.

5.5.1 Singal and System Design

As a proof of concept, a compact 38 mm × 13.2 mm baseboard (Infineon, DEMO BGT60TR13C) with a built-in USB interface for radar module configuration and data acquisition is positioned on the car seat, covered by a thick layer of foam. Six healthy subjects (three females and three males; age: 28 ± 8 years; weight: 72 ± 18 kg; height: 164 ± 14 cm) participated in these experiments, with each session lasting approximately 20 minutes. To validate the proposed approach, the Fourth Frontier (Frontier X) was worn beneath the clothing, in direct contact with the skin on the upper abdomen for heart monitoring. Additionally, a BioRadio piezoelectric respiratory effort belt was worn over the clothing for respiratory monitoring (refer to Figure 5.6). In addition, the signal design is as 5.3.1 where the heart waveform is explored in smart homes.

Figure 5.28 represents the signal processing chain for BR, HR, HRV, and heart waveform in the presence of two significant sources of interference, including car body vibration and human body movements. To address interferences from car body vibration, distinguishing between different vibrations is essential, particularly based on z-axis acceleration [226]. By utilizing this acceleration data, HRV may be eliminated from estimations. The ARIMA model can be employed to reconstruct human vibrations when car body vibrations interfere. In this thesis, ARIMA model forward forecasting is used. Compensation for human body movements is also addressed based on a study conducted inside smart homes. Additionally, a multi-bin approach is employed to improve the estimations as discussed in Chapter 3.

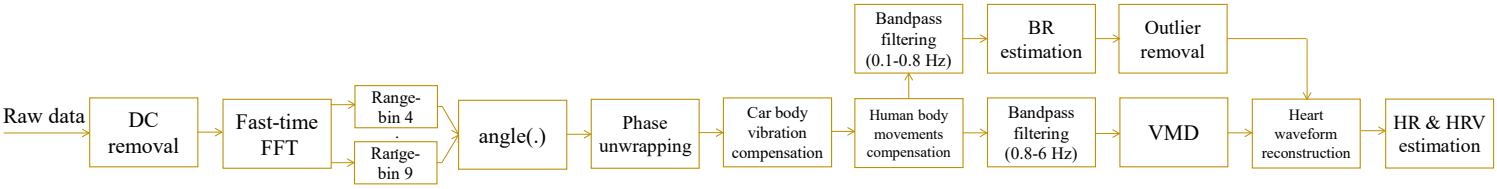

Figure 5.28: Signal processing chain for BR, HR, HRV, and heart waveform in the presence of two significant sources of interference, including car body vibration and human body movements.

5.5.2 Experimental Studies

Road defects like cracks and potholes can cause car body vibration, causing human body vibrations [54]. In [227], it is shown that when a vehicle is running on a smooth road, the z-axis acceleration can reach up to almost 12 m/s^2. However, road defects and speed bumps can cause stronger z-axis acceleration. In this thesis, the z-axis acceleration is used to detect road defects and speed bumps. After detecting road defects, it is crucial to remove those parts from human vibration and use forecasting approaches. In [228], different forecasting approaches have been utilized, and the ARIMA forward forecasting model is introduced as an optimum model for reconstructing spoiled human vibrations. In this thesis, this model is used for this purpose.

Figure 5.29 illustrates the effects of different driving situations on human body vibrations estimated by radar. Road defects are detected based on z-axis accelerations, and the signal is reconstructed using ARIMA model forward forecasting. In Figure 5.29(a), when the vehicle passed over a crack, a spike in human body vibrations was observed, with the affected portion identified based on z-axis acceleration. Similarly, in Figure 5.29(b), when the vehicle encountered a pothole, the signal was also compromised. In Figure 5.29(c), when the car traversed a speed bump, the signal distortion lasted for a shorter duration compared to other road defects. Hence, road defects have a greater impact on the signal than speed bumps. Finally, in Figure 5.29(d), when the car traverses multiple potholes, the signal is distorted for a longer duration.

Figure 5.30 illustrates the heart waveform of a healthy subject inside a running vehicle on a smooth pavement. Remarkably, the extracted heart waveform closely resembles that of a healthy subject in an in-home environment. This similarity suggests that findings from in-home settings can be applied to in-cabin applications for detecting individuals with heart conditions. However, on uneven pavement with road defects, the extracted heart waveform may not be reliable.

To evaluate the proposed method's robustness across diverse users, Figure 5.31 depicts a comprehensive illustration of the distribution of absolute errors in IBI estimation for all six participants. The findings reveal that the proposed method yields varying IBI estimation errors among different users, with median errors ranging from 21.6 to 45.8 ms. These variations can be attributed to a range of factors, including differences in individual physiological traits, such as body mass and variations in cardiac strength. Importantly, it is evident that the 75^{th} percentile error for all participants consistently remains below 66 ms. In addition, Table 5-6 also compares the absolute estimation error of HR for all participants. The results indicate that the absolute relative error for HR estimation reached 5.9%. To assess the accuracy of HRV estimation, Table 5-7 presents the estimated HRV metrics, including RMSSD, SDRR, and pNN50 for 8 participants. The results indicate that the proposed method achieves an average error of 7.3 ms for RMSSD, 7.7 ms for SDRR, and 7.7 % for pNN50. These observations underscore the method's resilience and effectiveness when applied to a diverse group of subjects.

Table 5-6: The average absolute errors of HR estimations in different participants by the proposed method in the running vehicle measurement.

User ID	Relative error (%)
1	6.3
2	6.1
3	5.8
4	3.8
5	7.1
6	6.4

Table 5-7: HRV estimation errors in terms of RMSSD, SDRR, and pNN50 for 8 subjects.

Metrics	User ID					
	1	2	3	4	5	6
RMSSD (ms)	6.4	6.9	6.2	9.2	8.6	6.4
SDRR (ms)	13.2	5.5	4.3	6.5	7.9	8.8
pNN50 (%)	7.3	12.2	5.3	5.9	8.9	6.8

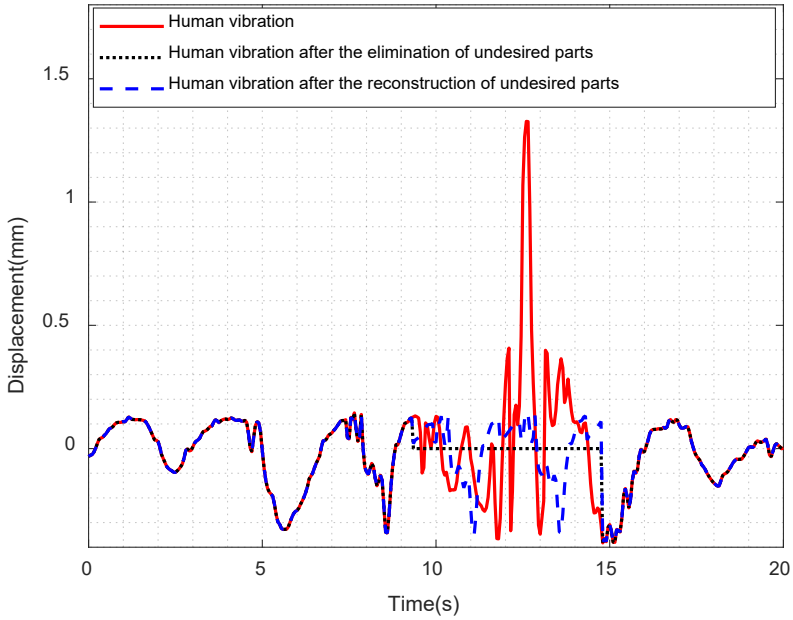

(a)

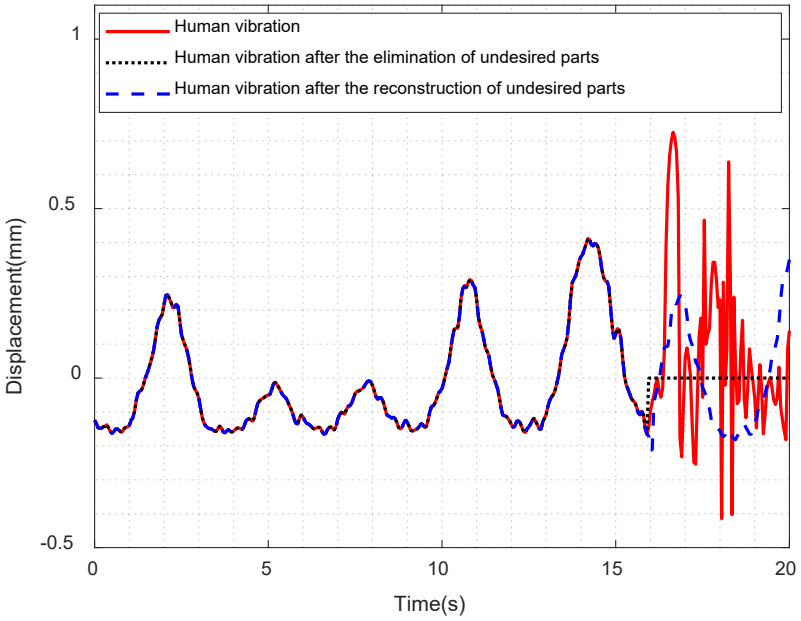
Human vibration
Human vibration after the elimination of undesired parts
Human vibration after the reconstruction of undesired parts
Displacement(mm)
Time(s)
1
0.5
0
-0.5
0
5
10
15
20

(b)

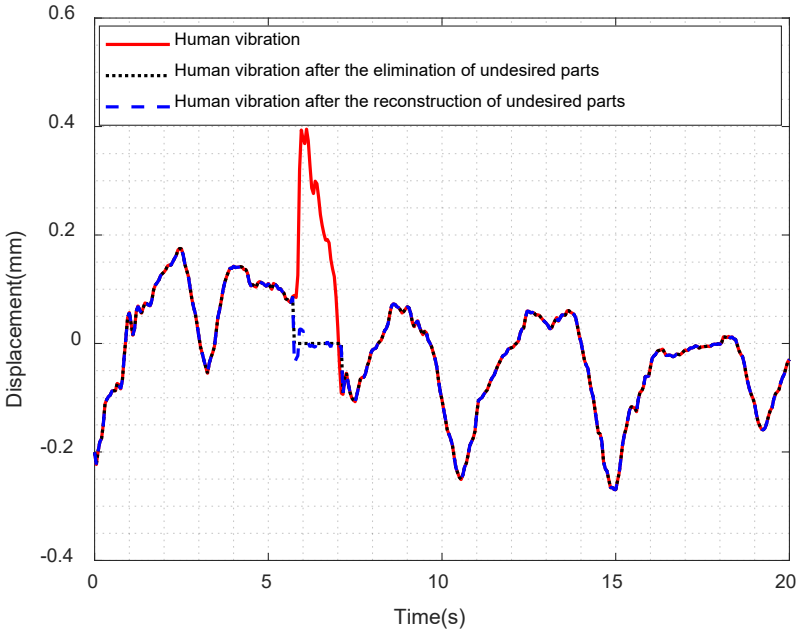
Human vibration
Human vibration after the elimination of undesired parts
Human vibration after the reconstruction of undesired parts
Displacement(mm)
Time(s)
0.6
0.4
0.2
0
-0.2
-0.4
0
5
10
15
20

(c)

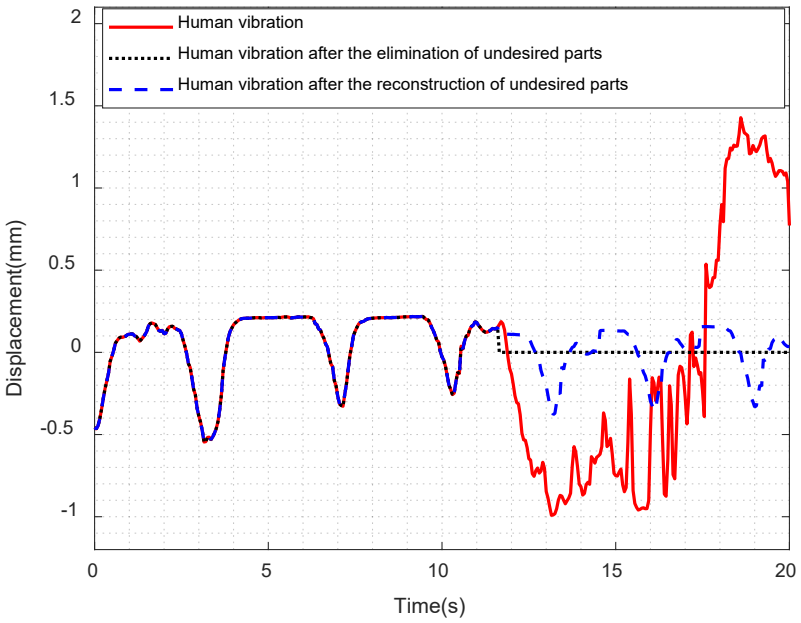

(d)

Figure 5.29: The effects of different driving situations on human body vibrations estimated by radar: (a) crack, (b) pothole, (c) speed bump, and (d) multiple potholes.

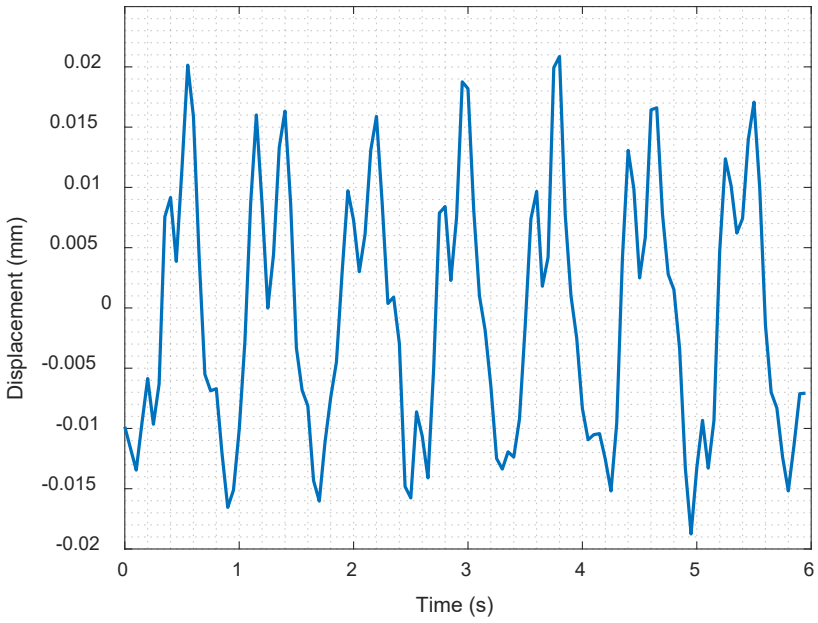

Figure 5.30: The heart waveform of a healthy subject inside a running vehicle on a smooth pavement.

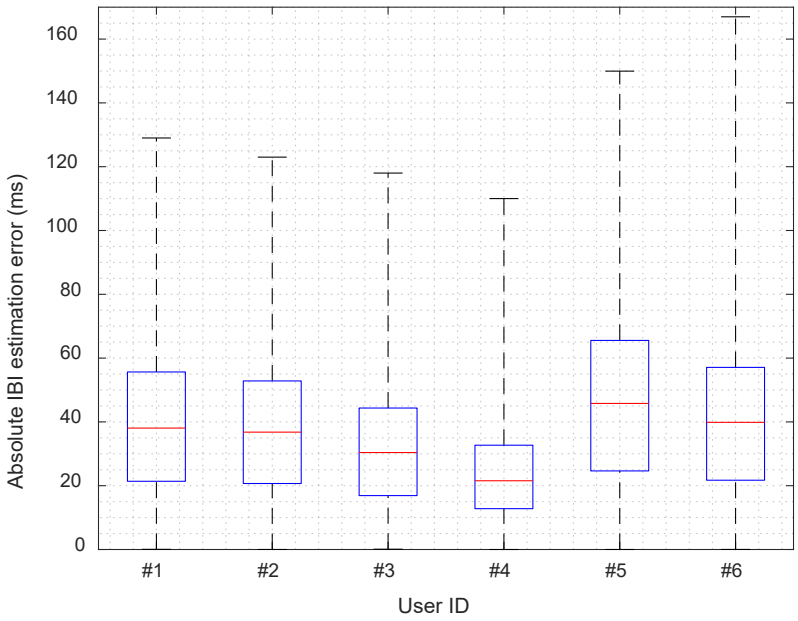

Figure 5.31: Influence of user diversity on the error in absolute IBI estimation for inside the vehicle.

5.6 Conclusion

In this investigation into cardiac health monitoring within smart furniture using a mm-wave radar, this study reveals distinctive heart waveform patterns for healthy individuals, even during breathing, when the radar is strategically positioned behind the subjects. This specific pattern includes two peaks and a valley in each cycle, offering reliable HRV estimation, particularly with the valleys. Additionally, the heart waveform extracted from individuals with prolonged QTc is compared to that of healthy individuals. The comparison reveals distinguishable differences, indicating that those with this condition exhibit a different heart waveform compared to their healthy counterparts. Consequently, this distinctive heart waveform serves as a potential indicator for the detection of underlying heart issues. As a result, this system provides a low-power, cost-effective, and non-contact solution for monitoring heart issues in elderly individuals who may forget to wear sensors, all while ensuring privacy. The experiments demonstrate a median IBI estimation error of 30 ms and an average relative error of 4.8% for HR estimation using the proposed VMD and multi-bin approach. Furthermore, the study addresses seated individuals' body movements using a time-domain approach, effectively detecting and mitigating these movements. Finally, the impact of car body vibrations within vehicle applications is investigated. The proposed signal processing chain enables the detection of road defects and speed bumps, facilitating accurate heart monitoring. This results in a median IBI estimation error of 37 ms and an average relative error of 5.9% for HR estimation.

Chapter 6
Conclusions and Future Works

Technologies capable of detecting and estimating health conditions can play a crucial role in preventing serious issues and sudden deaths. Such technologies are particularly useful in vehicles and smart homes, where people spend a significant portion of their day. Given the privacy concerns in these environments, radars are a preferred option for these applications. Mm-wave FMCW radars can monitor human health conditions. Their ability to radiate short-wavelength waves enables the estimation of human body vibrations that can be utilized to estimate breathing and heart waveforms. These waveforms can be employed to estimate vital signs such as BR, HR, HRV, and heart waveform. Ultimately, these criteria can be utilized to detect health conditions.

6.1 Summary of Contributions

- **Novel Dual Radar Fusion Approach for Breathing Monitoring**

A novel dual radar fusion approach for accurate monitoring of drivers' breathing patterns is presented. The proposed method utilizes two radars that are separated both in the time domain and in the covered spots to avoid interference and improve accuracy. Time domain separation is based on the signal parameters, specifically tailored for the driver status monitoring application. Additionally, the radars are placed in distinct positions to separate covered spots. The use of dual radar fusion with these separation techniques can provide more reliable and precise monitoring of breathing patterns, which is crucial for ensuring the health and safety of drivers. To the best of our knowledge, the proposed approach represents the first instance in which dual radar fusion, incorporating both time and space separations, has been employed for driver status monitoring inside a vehicle.

In signal processing chains, a comprehensive framework that encompasses all the necessary steps for estimating BR and detecting breath-hold periods using a dual radar system is presented. The proposed algorithm for breathing monitoring can detect a range of breathing abnormalities, including Tachypnea, Bradypnea, Biot, Cheyne-stokes, and Apnea. Although most in-cabin papers focused on BR estimation [23], [24], [26], [28], [29], [45], this thesis focuses on the detection of these abnormalities while driving. It is worth noting that the proposed signal processing chain employs multiple range bins to estimate vital signs to be more robust to other interfering vibrations.

- **Exploration of Heart Waveform Patterns in both Healthy and Unhealthy Subjects**

A novel signal processing chain is proposed to estimate the heart waveform using a single radar positioned behind the seat, eliminating the need for range bin selection and vulnerability to noise effects. However, the proposed signal processing chain faces various challenges, such as body movements, shallow breathing, and deep breathing. The body movements investigation indicates that body movements usually cause spikes in estimated movements by radar signal introducing interferences across a wide range of frequency bands, covering both breathing and heartbeat frequencies. Consequently, it is imperative to employ time-domain approaches to effectively address and mitigate the interferences caused by these movements. The investigation into removing deep and shallow breathing effects from heart displacements, utilizing a heuristic approach with the VMD algorithm and harmonic analysis, suggests that even with deep breathing, it is feasible to reconstruct heart waveforms using only two harmonics.

The investigation into the heart waveform of healthy subjects reveals that heart displacements on the skin have two peaks sequenced with one valley in each cycle. This pattern is verified in different situations, including body movements, shallow breathing, and deep breathing. Additionally, in individuals with the prolonged QTc condition, the previously mentioned typical heart waveform pattern is no longer applicable. Consequently, this distinctive heart waveform can serve as an effective indicator for detecting heart-related issues.

Finally, the in-home monitoring signal processing chain is enhanced with road defect detection based on z-axis acceleration for utilization inside the running vehicle. It is worth noting that the proposed signal processing chains employ multiple range bins to estimate vital signs to be more robust to other interfering vibrations.

6.2 Comparison Between Different Proposed Methods

Table 6-1 compares different proposed setups in this thesis based on price issue, wiring difficulty, computation difficulty, multipath issue, hand and head movement issue, and false detection issue. While MIMO radar presents an economical and simplified wiring solution, it faces significant challenges with multipath reflections. Both dual radar and MIMO radar systems are susceptible to issues with hand and head movements due to their frontal positioning relative to subjects. In contrast, seat radar technology effectively mitigates multipath issues without requiring intricate signal processing algorithms for target detection. Furthermore, in terms of cost-effectiveness, seat radar emerges as a more financially viable alternative compared to dual radar systems.

Table 6-1: Comparison between different proposed setups.

	Price issue	Wiring difficulty	Computation difficulty	Multipath issue	Hand and head movement issue	False detection issue
Dual radar	Worse	Worse	Moderate	Moderate	Moderate	Moderate
MIMO radar	Great	Great	Worse	Worse	Worse	Worse
Seat Radar	Moderate	Moderate	Great	Great	Great	Great

6.3 Impact of This Research

Monitoring the driver's condition is crucial for ensuring safety within vehicles, as it aids in identifying potential health or safety hazards that may compromise the driver's ability to operate the vehicle safely. This includes vigilance for fatigue, distraction, or impairment, all of which can precipitate vehicular accidents. While numerous solutions for health monitoring in private vehicles have been proposed, many are impractical or pose risks of privacy infringement. Radars offer a promising avenue to address these concerns, given their inherent privacy protection, contactless operation, accuracy, convenience, affordability, and resilience to environmental factors. Among various radar configurations, mm-wave FMCW radars stand out for their ability to detect range precisely and monitor displacements, which is crucial for health monitoring.

Breathing pattern monitoring serves as a vital indicator of the driver's health. A precise estimation of breathing patterns facilitates the detection of various abnormalities, such as Tachypnea, Bradypnea, Biot, Cheyne–Stokes, and Apnea. These patterns can be assessed from both chest and abdomen movements. In this study, two 60 GHz FMCW radars are utilized for this purpose. The proposed algorithm effectively detects these abnormalities by estimating BRs and identifying breath-hold periods.

Integrating radar technology into smart furniture and seats offers a practical way to monitor health. In this thesis, an mm-wave radar system placed strategically behind a seat is introduced, along with an algorithm that can identify unique heart waveform patterns in healthy individuals. These patterns typically include two peaks followed by a valley in each cycle, allowing for accurate heart waveform monitoring.

The findings indicate that individuals with prolonged corrected QT intervals have different heart waveforms. Therefore, the proposed system can be employed to detect these heart conditions.

6.4 Limitations and Future Directions

The research presented in this thesis has also several limitations. Firstly, the proposed approach for breathing and heart waveforms monitoring struggles with handling high random body movements. If such activity persists for more than 10 seconds, estimating the BR becomes challenging, especially when the actual BR is more than 20. This phenomenon commonly occurs when the driver is stressed and steers the wheel sharply.

Secondly, the extracted heart waveform from individuals with prolonged QTc conditions is visually compared with those from healthy individuals. Consequently, it is crucial to collect data from individuals with various HRs to enable the use of machine-learning approaches for detection. Otherwise, the detection may be unreliable.

Thirdly, employing a MIMO radar for occupancy detection presents several challenges, particularly due to the similarity between adults and children older than 5 years old. In this thesis, the occupied volume in each seat is used as an indicator to detect occupancy. However, it becomes essential to incorporate multiple features beyond just occupied volume. This necessitates collecting data from children within this age range.

Additionally, relying solely on z-axis acceleration for road defect detection is not a reliable approach, as this method is employed in this thesis. This task requires studying various features of IMU data and collecting data from different road defects and vehicles to ensure accuracy and robustness. In this way, AI can be used for road defect identification.

6.5 Publications

A. Gharamohammadi, M. Pirani, A. Khajepour and G. Shaker, "Multibin Breathing Pattern Estimation by Radar Fusion for Enhanced Driver Monitoring," in *IEEE Transactions on Instrumentation and Measurement*, vol. 73, pp. 1-12, 2024, Art no. 8001212, doi: 10.1109/TIM.2023.3345909.

A. Gharamohammadi, A. Khajepour and G. Shaker, "In-Vehicle Monitoring by Radar: A Review," in *IEEE Sensors Journal*, vol. 23, no. 21, pp. 25650-25672, 1 Nov.1, 2023, doi: 10.1109/JSEN.2023.3316449.

S. Abu-Sardanah, A. Gharamohammadi, O. M. Ramahi and G. Shaker, "A Wearable mm-Wave Radar Platform for Cardiorespiratory Monitoring," in *IEEE Sensors Letters*, vol. 7, no. 6, pp. 1-4, June 2023, Art no. 6003404, doi: 10.1109/LSENS.2023.3277365.

M. O. Bagheri, A. Gharamohammadi, S. Abu-Sardanah, O. M. Ramahi, and G. Shaker, “Radar near-field sensing using metasurface for biomedical applications,” in *Communications Engineering*, vol. 3, no. 1, p. 51, 2024, doi: 10.1038/s44172-024-00194-4.

A. Gharamohammadi and G. Shaker, "A novel back-projection algorithm improved by antenna pattern automatized by 2-D CFAR," *2022 IEEE International Symposium on Antennas and Propagation and USNC-URSI Radio Science Meeting (AP-S/URSI)*, Denver, CO, USA, 2022, pp. 1158-1159, doi: 10.1109/AP-S/USNC-URSI47032.2022.9886587.

A. Gharamohammadi, F. Behnia, A. Shokouhmand, and G. Shaker, “Robust Wiener filter-based time gating method for detection of shallowly buried objects,” *IET Signal Processing*, 2021, doi: 10.1049/sil2.12011.

Bibliography

[1] H. Lichtinger, B. M. Curtis, R. Graf, D. Reich, S. Morrell, and M. Kremer, "Sensor assembly for seat occupant weight classification system," Mar. 2009 Accessed: Oct. 07, 2022. [Online]. Available: https://patents.google.com/patent/US7503417B2/en

[2] D. S. Breed, W. E. DuVall, and W. C. Johnson, "Dynamic weight sensing and classification of vehicular occupants," Nov. 2009 Accessed: Oct. 08, 2022. [Online]. Available: https://patents.google.com/patent/US7620521B2/en

[3] F. Reverter, J. Jordana, M. Gasulla, and R. Pallàs-Areny, "Accuracy and resolution of direct resistive sensor-to-microcontroller interfaces," *Sens Actuators A Phys*, vol. 121, no. 1, pp. 78–87, 2005, doi: https://doi.org/10.1016/j.sna.2005.01.010.

[4] M. G. Kisic, N. V Blaz, K. B. Babkovic, L. D. Zivanov, and M. S. Damnjanovic, "Detection of Seat Occupancy Using a Wireless Inductive Sensor," *IEEE Trans Magn*, vol. 53, no. 4, pp. 1–4, 2017, doi: 10.1109/TMAG.2016.2632862.

[5] A. Satz, D. Hammerschmidt, and D. Tumpold, "Capacitive passenger detection utilizing dielectric dispersion in human tissues," *Sens Actuators A Phys*, vol. 152, no. 1, pp. 1–4, 2009, doi: https://doi.org/10.1016/j.sna.2009.03.005.

[6] H. Abedi, S. Luo, V. Mazumdar, M. M. Y. R. Riad, and G. Shaker, "AI-Powered In-Vehicle Passenger Monitoring Using Low-Cost mm-Wave Radar," *IEEE Access*, vol. 10, pp. 18998–19012, 2022, doi: 10.1109/ACCESS.2021.3138051.

[7] H. Song and H.-C. Shin, "Single-Channel FMCW-Radar-Based Multi-Passenger Occupancy Detection Inside Vehicle," *Entropy*, vol. 23, no. 11, 2021, doi: 10.3390/e23111472.

[8] Y.-L. Hou and G. K. H. Pang, "People Counting and Human Detection in a Challenging Situation," *IEEE Transactions on Systems, Man, and Cybernetics - Part A: Systems and Humans*, vol. 41, no. 1, pp. 24–33, 2011, doi: 10.1109/TSMCA.2010.2064299.

[9] N. C. Tang, Y.-Y. Lin, M.-F. Weng, and H.-Y. M. Liao, "Cross-Camera Knowledge Transfer for Multiview People Counting," *IEEE Transactions on Image Processing*, vol. 24, no. 1, pp. 80–93, 2015, doi: 10.1109/TIP.2014.2363445.

[10] L. Wu and Y. Wang, "A Low-Power Electric-Mechanical Driving Approach for True Occupancy Detection Using a Shuttered Passive Infrared Sensor," *IEEE Sens J*, vol. 19, no. 1, pp. 47–57, 2019, doi: 10.1109/JSEN.2018.2875659.

[11] H. Abedi, C. Magnier, V. Mazumdar, and G. Shaker, “Improving passenger safety in cars using novel radar signal processing,” *Engineering Reports*, vol. 3, no. 12, p. e12413, 2021, doi: 10.1002/eng2.12413.

[12] J. Yang, M. Santamouris, and S. E. Lee, “Review of occupancy sensing systems and occupancy modeling methodologies for the application in institutional buildings,” *Energy Build*, vol. 121, pp. 344–349, 2016, doi: 10.1016/j.enbuild.2015.12.019.

[13] H. Abedi, M. Ma, J. Yu, J. He, A. Ansariyan, and G. Shaker, “On the Use of Machine Learning and Deep Learning for Radar- Based Passenger Monitoring,” in *2022 IEEE International Symposium on Antennas and Propagation and USNC-URSI Radio Science Meeting (AP-S/URSI)*, 2022, pp. 902–903. doi: 10.1109/AP-S/USNC-URSI47032.2022.9887034.

[14] H. Lv *et al.*, “Multi-target human sensing via UWB bio-radar based on multiple antennas,” in *2013 IEEE International Conference of IEEE Region 10 (TENCON 2013)*, 2013, pp. 1–4. doi: 10.1109/TENCON.2013.6718817.

[15] N. Maaref, P. Millot, Ch. Pichot, and O. Picon, “A Study of UWB FM-CW Radar for the Detection of Human Beings in Motion Inside a Building,” *IEEE Transactions on Geoscience and Remote Sensing*, vol. 47, no. 5, pp. 1297–1300, 2009, doi: 10.1109/TGRS.2008.2010709.

[16] W. Kang, C. Zhou, and W. Wu, “Respiration Monitoring of All Occupants in a Vehicle Using Time-Division Multiplexing FMCW Radar Based on Metasurface Technology,” *IEEE Trans Microw Theory Tech*, pp. 1–15, 2024, doi: 10.1109/TMTT.2024.3361949.

[17] S. Lim, G. S. Jang, W. Song, B. Kim, and D. H. Kim, “Non-Contact VITAL Signs Monitoring of a Patient Lying on Surgical Bed Using Beamforming FMCW Radar,” *Sensors*, vol. 22, no. 21, 2022, doi: 10.3390/s22218167.

[18] “Hyundai Inc.” Accessed: Oct. 28, 2022. [Online]. Available: https://www.tu-auto.com/hyundais-radar-to-protect-forgotten-kids/

[19] “Toyota Inc.” Accessed: Nov. 06, 2022. [Online]. Available: https://blog.vayyar.com/vayyar-sensor-for-toyota-cabin-awareness

[20] H. U. R. Siddiqui *et al.*, “Non-Invasive Driver Drowsiness Detection System,” *Sensors*, vol. 21, no. 14, 2021, doi: 10.3390/s21144833.

[21] K. Staszek, K. Wincza, and S. Gruszczynski, “Driver’s drowsiness monitoring system utilizing microwave Doppler sensor,” in *2012 19th International Conference on Microwaves, Radar & Wireless Communications*, 2012, pp. 623–626. doi: 10.1109/MIKON.2012.6233616.

[22] G. Ciattaglia, S. Spinsante, and E. Gambi, “Slow-Time mmWave Radar Vibrometry for Drowsiness Detection,” in *2021 IEEE International Workshop on Metrology for Automotive (MetroAutomotive)*, 2021, pp. 141–146. doi: 10.1109/MetroAutomotive50197.2021.9502850.

[23] M. Mahler, H.-O. Ruob, and W. Menzel, “Radar Sensors to Determine Position and Physiological Parameters of a Person in a Vehicle,” in *2002 32nd European Microwave Conference*, 2002, pp. 1–4. doi: 10.1109/EUMA.2002.339439.

[24] X. Xu *et al.*, “mmECG: Monitoring Human Cardiac Cycle in Driving Environments Leveraging Millimeter Wave,” in *IEEE INFOCOM 2022 - IEEE Conference on Computer Communications*, 2022, pp. 90–99. doi: 10.1109/INFOCOM48880.2022.9796912.

[25] A. Lazaro, M. Lazaro, R. Villarino, and D. Girbau, “Seat-Occupancy Detection System and Breathing Rate Monitoring Based on a Low-Cost mm-Wave Radar at 60 GHz,” *IEEE Access*, vol. 9, pp. 115403–115414, 2021, doi: 10.1109/ACCESS.2021.3105390.

[26] S. Leonhardt, L. Leicht, and D. Teichmann, “Unobtrusive Vital Sign Monitoring in Automotive Environments—A Review,” *Sensors*, vol. 18, no. 9, 2018, doi: 10.3390/s18093080.

[27] C. Yang, X. Wang, and S. Mao, “Respiration Monitoring With RFID in Driving Environments,” *IEEE Journal on Selected Areas in Communications*, vol. 39, no. 2, pp. 500–512, 2021, doi: 10.1109/JSAC.2020.3020606.

[28] L. Broto and M. Okimoto, “Utilization of Low-Cost Pulse Coherent Radar for Physiological Assessment in Vehicle Interior,” in *XXXVIII Brazilian Symposium on Telecommunications and Signal Processing*, Jul. 2020. doi: 10.14209/SBRT.2020.1570661619.

[29] S. Lee *et al.*, “A 24-GHz RF Transmitter in 65-nm CMOS for In-Cabin Radar Applications,” *Electronics (Basel)*, vol. 9, no. 12, 2020, doi: 10.3390/electronics9122005.

[30] C. Schwarz, H. Zainab, S. Dasgupta, and J. Kahl, “Heartbeat Measurement with Millimeter Wave Radar in the Driving Environment,” in *2021 IEEE Radar Conference (RadarConf21)*, 2021, pp. 1–6. doi: 10.1109/RadarConf2147009.2021.9455182.

[31] M. J. López Montero, A. Aguasca Solé, J. Romeu Robert, and L. Jofre Roca, “In-cabin 120 GHz radar system for functional human breathing monitoring in a 3D scenario,” in *XXXVI Simposium Nacional de la Unión Científica Internacional de Radio (URSI 2021 Vigo): virtual: Septiembre 20-24, 2021: actas*, Íñigo Cuiñas Gómez, 2021. Accessed: Oct. 09, 2022. [Online]. Available: https://upcommons.upc.edu/bitstream/handle/2117/370191/URSI_FINAL.pdf?sequence=1&isAllowed=y

[32] L. C. Broto, “Application of low cost pulse radar for heart rate detection in vehicle interior,” Technische Hochschule Ingolstadt, 2021. Accessed: Oct. 08, 2022. [Online]. Available: https://opus4.kobv.de/opus4-haw/frontdoor/index/index/docId/789

[33] C. Loss, C. Gouveia, R. Salvado, P. Pinho, and J. Vieira, “Textile Antenna for Bio-Radar Embedded in a Car Seat,” *Materials*, vol. 14, no. 1, 2021, doi: 10.3390/ma14010213.

[34] K.-K. Shyu, L.-J. Chiu, P.-L. Lee, and L.-H. Lee, “UWB Simultaneous Breathing and Heart Rate Detections in Driving Scenario Using Multi-Feature Alignment Two-Layer EEMD Method,” *IEEE Sens J*, vol. 20, no. 17, pp. 10251–10266, 2020, doi: 10.1109/JSEN.2020.2992687.

[35] I. Sloushch, V. Kotlar, K. Berezin, and A. Arshavski, “System for non-contact detection and monitoring of vital signs of occupants of a vehicle,” 2019 Accessed: Oct. 07, 2022. [Online]. Available: https://patents.google.com/patent/WO2019026076A1/en%20US4325121.pdf

[36] D. Oloumi and M. Bassi, “Monitoring Vital Sign of Occupant in a Vehicle Seat,” Mar. 18, 2021 Accessed: Oct. 07, 2022. [Online]. Available: https://patents.google.com/patent/US20210076971A1/en

[37] M.-J. López, C. Palacios, J. Romeu, and L. Jofre-Roca, “In-Cabin MIMO Radar System for Human Dysfunctional Breathing Detection,” *IEEE Sens J*, p. 1, 2022, doi: 10.1109/JSEN.2022.3221052.

[38] C. Gouveia, C. Loss, P. Pinho, J. Vieira, and D. Albuquerque, “Low-Profile Textile Antenna for Bioradar Integration Into Car Seat Upholstery: Wireless acquisition of vital signs while on the road.,” *IEEE Antennas Propag Mag*, pp. 2–12, 2023, doi: 10.1109/MAP.2023.3254484.

[39] M.-J. López, C. Palacios, J. Romeu, and L. Jofre-Roca, “MIMO Radar Antenna with Sectorial Human Torso Illumination for an In-Cabin Breathing Detection System,” in *2023 17th European Conference on Antennas and Propagation (EuCAP)*, 2023, pp. 1–5. doi: 10.23919/EuCAP57121.2023.10133775.

[40] T. V. Palandurkar, L. Y. Chan, J. L. Da Silva, A. Zimmer, and U. T. Schwarz, “Driver’s Chest Position Detection using FMCW Radar Data Collected in a Vehicle Mock-up and CNN,” in *2023 24th International Radar Symposium (IRS)*, 2023, pp. 1–12. doi: 10.23919/IRS57608.2023.10172421.

[41] J. Sini, L. Pugliese, S. Groppo, M. Guagnano, and M. Violante, “Towards In-Cabin Monitoring: A Preliminary Study on Sensors Data Collection and Analysis,” *arXiv preprint arXiv:2309.11890*, 2023.

[42] A. Kanakapura Sriranga, Q. Lu, and S. A. Birrell, “A Deep Learning Based Contactless Driver State Monitoring Radar System for In-Vehicle Physiological Applications,” *Qian and Birrell, Stewart A., A Deep Learning Based Contactless Driver State Monitoring Radar System for In-Vehicle Physiological Applications*.

[43] Z. Yang, M. Bocca, V. Jain, and P. Mohapatra, “Contactless Breathing Rate Monitoring in Vehicle Using UWB Radar,” in *Proceedings of the 7th International Workshop on Real-World Embedded Wireless*

Systems and Networks, in RealWSN'18. New York, NY, USA: Association for Computing Machinery, 2018, pp. 13–18. doi: 10.1145/3277883.3277884.

[44] G. Vinci, T. Lenhard, C. Will, and A. Koelpin, "Microwave interferometer radar-based vital sign detection for driver monitoring syst," in *2015 IEEE MTT-S International Conference on Microwaves for Intelligent Mobility (ICMIM)*, 2015, pp. 1–4. doi: 10.1109/ICMIM.2015.7117940.

[45] F. Wang, X. Zeng, C. Wu, B. Wang, and K. J. R. Liu, "Driver Vital Signs Monitoring Using Millimeter Wave Radio," *IEEE Internet Things J*, vol. 9, no. 13, pp. 11283–11298, 2022, doi: 10.1109/JIOT.2021.3128548.

[46] S. Suzuki *et al.*, "A non-contact vital sign monitoring system for ambulances using dual-frequency microwave radars," *Med Biol Eng Comput*, vol. 47, no. 1, pp. 101–105, 2009, doi: 10.1007/s11517-008-0408-x.

[47] S. K. Leem, F. Khan, and S. H. Cho, "Vital Sign Monitoring and Mobile Phone Usage Detection Using IR-UWB Radar for Intended Use in Car Crash Prevention," *Sensors*, vol. 17, no. 6, 2017, doi: 10.3390/s17061240.

[48] X. Gu, L. Zhang, Y. Xiao, H. Zhang, H. Hong, and X. Zhu, "Non-contact Fatigue Driving Detection Using CW Doppler Radar," in *2018 IEEE MTT-S International Wireless Symposium (IWS)*, 2018, pp. 1–3. doi: 10.1109/IEEE-IWS.2018.8400971.

[49] I. C. Kyo and M. B. Chan, "A Study of Detection of Drowsiness and Awakeness using Non-contact Radar Sensors".

[50] V. Branković, P. Jovanović, V. Mihajlović, M. Savić, and D. TASOVAC, "Mm-wave radar driver fatigue sensor apparatus," Jan. 09, 2018 Accessed: Oct. 07, 2022. [Online]. Available: https://patents.google.com/patent/US9862271B2/en

[51] H. Zhao, H. Zhao, L. Han, and Z. Sun, "Non-contact road anger detection device based on millimeter wave radar," in *2nd International Conference on Internet of Things and Smart City (IoTSC 2022)*, F. Falcone, H. Cui, and X. Ye, Eds., SPIE, 2022, pp. 969 – 974. doi: 10.1117/12.2637169.

[52] S. M. M. Islam, N. Motoyama, S. Pacheco, and V. M. Lubecke, "Non-Contact Vital Signs Monitoring for Multiple Subjects Using a Millimeter Wave FMCW Automotive Radar," in *2020 IEEE/MTT-S International Microwave Symposium (IMS)*, 2020, pp. 783–786. doi: 10.1109/IMS30576.2020.9223838.

[53] M. Yang, X. Yang, L. Li, and L. Zhang, "In-Car Multiple Targets Vital Sign Monitoring Using Location-Based VMD Algorithm," in *2018 10th International Conference on Wireless Communications and Signal Processing (WCSP)*, 2018, pp. 1–6. doi: 10.1109/WCSP.2018.8555567.

[54] S. Dias Da Cruz, H.-P. Beise, U. Schröder, and U. Karahasanovic, “A Theoretical Investigation of the Detection of Vital Signs in Presence of Car Vibrations and RADAR-Based Passenger Classification,” *IEEE Trans Veh Technol*, vol. 68, no. 4, pp. 3374–3385, 2019, doi: 10.1109/TVT.2019.2898512.

[55] S. D. Da Cruz, H.-P. Beise, U. Schröder, and U. Karahasanovic, “Detection of Vital Signs in Presence of Car Vibrations and RADAR-Based Passenger Classification,” in *2018 19th International Radar Symposium (IRS)*, 2018, pp. 1–10. doi: 10.23919/IRS.2018.8447952.

[56] I. D. Castro, M. Mercuri, A. Patel, R. Puers, C. van Hoof, and T. Torfs, “Physiological Driver Monitoring Using Capacitively Coupled and Radar Sensors,” *Applied Sciences*, vol. 9, no. 19, 2019, doi: 10.3390/app9193994.

[57] Y.-K. Yoo and H.-C. Shin, “Movement Compensated Driver’s Respiratory Rate Extraction,” *Applied Sciences*, vol. 12, no. 5, 2022, doi: 10.3390/app12052695.

[58] B. Möhring, U. Siart, S. Schweizer, and T. F. Eibert, “Transmission Line Based Frequency Modulated Continuous Wave Radar for Monitoring Airbag Deployment Processes,” in *2021 18th European Radar Conference (EuRAD)*, 2022, pp. 481–484. doi: 10.23919/EuRAD50154.2022.9784467.

[59] J. Jung, S. Lim, B.-K. Kim, and S. Lee, “CNN-Based Driver Monitoring Using Millimeter-Wave Radar Sensor,” *IEEE Sens Lett*, vol. 5, no. 3, pp. 1–4, 2021, doi: 10.1109/LSENS.2021.3063086.

[60] H. N. Nguyen, S. Lee, T.-T. Nguyen, and Y.-H. Kim, “One-shot learning-based driver’s head movement identification using a millimetre-wave radar sensor,” *IET Radar, Sonar & Navigation*, vol. 16, no. 5, pp. 825–836, 2022, doi: 10.1049/rsn2.12223.

[61] D. G. Bresnahan and Y. Li, “Classification of Driver Head Motions Using a mm-Wave FMCW Radar and Deep Convolutional Neural Network,” *IEEE Access*, vol. 9, pp. 100472–100479, 2021, doi: 10.1109/ACCESS.2021.3096465.

[62] H.-O. Ruoss, M. Mahler, and J. Seidel, “Radar-assisted sensing of the position and/or movement of the body or inside the body of living beings,” Mar. 27, 2007 Accessed: Oct. 07, 2022. [Online]. Available: https://patents.google.com/patent/US7196629B2/en

[63] V. Pettersson and S. An, “Radar Cross-Section Characterization of the Car In-Cabin Environment at Sub-THz Frequencies,” in *2022 19th European Radar Conference (EuRAD)*, 2022, pp. 269–272. doi: 10.23919/EuRAD54643.2022.9924792.

[64] I. Brishtel, S. Krauss, M. Chamseddine, J. R. Rambach, and D. Stricker, “Driving Activity Recognition Using UWB Radar and Deep Neural Networks,” *Sensors*, vol. 23, no. 2, 2023, doi: 10.3390/s23020818.

[65] J. Hu *et al.*, “BlinkRadar: Non-Intrusive Driver Eye-Blink Detection with UWB Radar,” 2022, Accessed: Oct. 08, 2022. [Online]. Available: https://dsg.tuwien.ac.at/team/sd/papers/Zeitschriftenartikel_2022_SD_Blink.pdf

[66] Y. Wang, Y. Shu, and M. Zhou, “A Novel Eye Blink Detection Method using Frequency Modulated Continuous Wave Radar,” in *2021 IEEE International Workshop on Electromagnetics: Applications and Student Innovation Competition (iWEM)*, 2021, pp. 1–3. doi: 10.1109/iWEM53379.2021.9790529.

[67] K. Yamamoto, K. Toyoda, and T. Ohtsuki, “Driver’s blink detection using Doppler sensor,” in *2017 IEEE 28th Annual International Symposium on Personal, Indoor, and Mobile Radio Communications (PIMRC)*, 2017, pp. 1–6. doi: 10.1109/PIMRC.2017.8292496.

[68] Y. Shu, Y. Wang, X. Yang, and Z. Tian, “An improved denoising method for eye blink detection using automotive millimeter wave radar,” *EURASIP J Adv Signal Process*, vol. 2022, no. 1, p. 9, 2022, doi: 10.1186/s13634-022-00841-y.

[69] C. Tamba, H. Hayashi, and T. Ohtsuki, “Improvement of Blink Detection Using a Doppler Sensor Based on CFAR Processing,” in *2016 IEEE Global Communications Conference (GLOBECOM)*, 2016, pp. 1–6. doi: 10.1109/GLOCOM.2016.7841887.

[70] S. Lim, J. Jung, S.-C. Kim, and S. Lee, “Deep Neural Network-Based In-Vehicle People Localization Using Ultra-Wideband Radar,” *IEEE Access*, vol. 8, pp. 96606–96612, 2020, doi: 10.1109/ACCESS.2020.2997033.

[71] M. Alizadeh, H. Abedi, and G. Shaker, “Low-cost low-power in-vehicle occupant detection with mm-wave FMCW radar,” in *2019 IEEE SENSORS*, 2019, pp. 1–4. doi: 10.1109/SENSORS43011.2019.8956880.

[72] E. Hyun, Y.-S. Jin, J.-H. Park, and J.-R. Yang, “Machine Learning-Based Human Recognition Scheme Using a Doppler Radar Sensor for In-Vehicle Applications,” *Sensors*, vol. 20, no. 21, 2020, doi: 10.3390/s20216202.

[73] H. Abedi, C. Magnier, and G. Shaker, “Passenger Monitoring Using AI-Powered Radar,” in *2021 IEEE 19th International Symposium on Antenna Technology and Applied Electromagnetics (ANTEM)*, 2021, pp. 1–2. doi: 10.1109/ANTEM51107.2021.9518503.

[74] H. Abedi, S. Luo, and G. Shaker, “On the Use of Low-Cost Radars and Machine Learning for In-Vehicle Passenger Monitoring,” in *2020 IEEE 20th Topical Meeting on Silicon Monolithic Integrated Circuits in RF Systems (SiRF)*, 2020, pp. 63–65. doi: 10.1109/SIRF46766.2020.9040191.

[75] Y. Chen, Y. Luo, A. Qi, M. Miao, and Y. Qi, “In-cabin Monitoring Based on Millimeter Wave FMCW radar,” in *2021 13th International Symposium on Antennas, Propagation and EM Theory (ISAPE)*, 2021, pp. 1–3. doi: 10.1109/ISAPE54070.2021.9753085.

[76] Y. Ma, Y. Zeng, and V. Jain, “CarOSense: Car Occupancy Sensing with the Ultra-Wideband Keyless Infrastructure,” *Proc. ACM Interact. Mob. Wearable Ubiquitous Technol.*, vol. 4, no. 3, Sep. 2020, doi: 10.1145/3411820.

[77] X. Yang, Y. Ding, X. Zhang, and L. Zhang, “Spatial-Temporal-Circulated GLCM and Physiological Features for In-Vehicle People Sensing Based on IR-UWB Radar,” *IEEE Trans Instrum Meas*, vol. 71, pp. 1–13, 2022, doi: 10.1109/TIM.2022.3165808.

[78] S. Lim, S. Lee, J. Jung, and S.-C. Kim, “Detection and Localization of People Inside Vehicle Using Impulse Radio Ultra-Wideband Radar Sensor,” *IEEE Sens J*, vol. 20, no. 7, pp. 3892–3901, 2020, doi: 10.1109/JSEN.2019.2961107.

[79] H. Song, Y. Yoo, and H.-C. Shin, “In-Vehicle Passenger Detection Using FMCW Radar,” in *International Conference on Information Networking (ICOIN)*, Jul. 2021, pp. 644–647. doi: 10.1109/ICOIN50884.2021.9334014.

[80] L. Servadei *et al.*, “Label-Aware Ranked Loss for Robust People Counting Using Automotive In-Cabin Radar,” in *ICASSP 2022 - 2022 IEEE International Conference on Acoustics, Speech and Signal Processing (ICASSP)*, 2022, pp. 3883–3887. doi: 10.1109/ICASSP43922.2022.9747621.

[81] Vayyar Inc., “In-cabin occupant status .” Accessed: Aug. 11, 2022. [Online]. Available: https://vayyar.com/auto/solutions/in-cabin/os/

[82] Texas Instruments Inc., “Vehicle occupant detection reference design.” Accessed: Aug. 11, 2022. [Online]. Available: shorturl.at/iPRW7

[83] Novelic Inc., “A Whole-Cabin Solution for In-Vehicle Safety and Comfort.” Accessed: Aug. 11, 2022. [Online]. Available: https://www.novelic.com/acam-automotive-in-cabin-monitoring-radar/

[84] Infineon Inc, “Presence detection and sensing”, Accessed: Aug. 11, 2022. [Online]. Available: https://www.infineon.com/cms/en/applications/solutions/sensor-solutions/presence-detection/

[85] A. Diewald, “Radar sensing of vehicle occupancy,” Jun. 06, 2017 Accessed: Oct. 07, 2022. [Online]. Available: https://patents.google.com/patent/US9671492B2/en

[86] G. Carenza and J. Landwehr, “Radar sensing of vehicle occupancy,” Oct. 05, 2017 Accessed: Oct. 07, 2022. [Online]. Available: https://patents.google.com/patent/US9671492B2/en

[87] S. Li, “Vehicle occupant detection system and method using radar motion sensor,” Jun. 22, 2004 Accessed: Oct. 07, 2022. [Online]. Available: https://patents.google.com/patent/US6753780B2/en

[88] S.-Y. Kwon and S. Lee, “In-Vehicle Seat Occupancy Detection Using Ultra-Wideband Radar Sensors,” in *2022 23rd International Radar Symposium (IRS)*, 2022, pp. 275–278. doi: 10.23919/IRS54158.2022.9905064.

[89] E. Turkmen *et al.*, “Car Interior Radar for Advanced Life-Signs Detection,” in *2022 24th International Microwave and Radar Conference (MIKON)*, 2022, pp. 1–6.

[90] R. Li, Z. Weng, Z. Cai, Y. Luo, and Y. Qi, “A Lens Antenna Design for In-Cabin Detection,” in *2022 Asia-Pacific International Symposium on Electromagnetic Compatibility (APEMC)*, 2022, pp. 382–384. doi: 10.1109/APEMC53576.2022.9888702.

[91] J. Möderl, F. Pernkopf, and K. Witrisal, “Car Occupancy Detection Using Ultra-Wideband Radar,” in *2021 18th European Radar Conference (EuRAD)*, 2022, pp. 313–316. doi: 10.23919/EuRAD50154.2022.9784505.

[92] H. Abedi, M. Ma, J. He, J. Yu, A. Ansariyan, and G. Shaker, “Deep Learning-Based In-Cabin Monitoring and Vehicle Safety System Using a 4D Imaging Radar Sensor,” *IEEE Sens J*, p. 1, 2023, doi: 10.1109/JSEN.2023.3270043.

[93] Y. Chen *et al.*, “Non-Contact In-Vehicle Occupant Monitoring System Based on Point Clouds from FMCW Radar,” *Technologies (Basel)*, vol. 11, no. 2, 2023, doi: 10.3390/technologies11020039.

[94] E. Hyun, Y. Jin, J. Bae, and P. Chi-Ho, “Machine Learning based In-Cabin Radar System for Passenger Monitoring System,” in *2023 IEEE 97th Vehicular Technology Conference (VTC2023-Spring)*, 2023, pp. 1–4. doi: 10.1109/VTC2023-Spring57618.2023.10200306.

[95] Z. Xiao, K. Ye, and G. Cui, “PointNet-Transformer Fusion Network for In-Cabin Occupancy Monitoring With mm-Wave Radar,” *IEEE Sens J*, vol. 24, no. 4, pp. 5370–5382, 2024, doi: 10.1109/JSEN.2023.3347893.

[96] N. M. Z. Hashim, H. Basri, A. Jaafar, M. A. Aziz, A. Salleh, and A. S. Ja’afar, “Child in car alarm system using various sensors,” 2014.

[97] H. Sterner, W. Aichholzer, and M. Haselberger, “Development of an Antenna Sensor for Occupant Detection in Passenger Transportation,” *Procedia Eng*, vol. 47, pp. 178–183, 2012, doi: 10.1016/j.proeng.2012.09.113.

[98] T. Mousel, P. Larsen, and H. Lorenz, “Unattended children in cars: radiofrequency-based detection to reduce heat stroke fatalities,” in *25th International Technical Conference on the Enhanced Safety of Vehicles (ESV): Innovations in Vehicle Safety: Opportunities and Challenges*, 2017. Accessed: Oct. 08, 2022. [Online]. Available: https://www-esv.nhtsa.dot.gov/Proceedings/25/25ESV-000039.pdf

[99] A. R. Diewald *et al.*, “RF-based child occupation detection in the vehicle interior,” in *2016 17th International Radar Symposium (IRS)*, 2016, pp. 1–4. doi: 10.1109/IRS.2016.7497352.

[100] A. Caddemi and E. Cardillo, “Automotive Anti-Abandon Systems: a Millimeter-Wave Radar Sensor for the Detection of Child Presence,” in *2019 14th International Conference on Advanced Technologies,*

Systems and Services in Telecommunications (TELSIKS), 2019, pp. 94–97. doi: 10.1109/TELSIKS46999.2019.9002193.

[101] A. R. Diewald, A. Fox, and D. Tatarinov, "Thorough analysis of multipath propagation effects for radar applications in the vehicle interior," in *2018 11th German Microwave Conference (GeMiC)*, 2018, pp. 63–66. doi: 10.23919/GEMIC.2018.8335029.

[102] A. R. Diewald and D. Tatarinov, "Non-broadside patch antenna for car-interior passenger detection," in *2017 18th International Radar Symposium (IRS)*, 2017, pp. 1–10. doi: 10.23919/IRS.2017.8008130.

[103] W. Peng *et al.*, "Safety Protection System Computer Aided Design in Enclosed Vehicle Using Film Pressure Sensor and Microwave Radar," in *2021 IEEE International Conference on Data Science and Computer Application (ICDSCA)*, 2021, pp. 553–555. doi: 10.1109/ICDSCA53499.2021.9650260.

[104] J. Liao, G. Xiang, L. Cao, J. Xia, and L. Yue, "The left-behind human detection and tracking system based on vision with multi-model fusion and microwave radar inside the bus," *Proceedings of the Institution of Mechanical Engineers, Part D: Journal of Automobile Engineering*, vol. 234, no. 9, pp. 2342–2354, 2020, doi: 10.1177/0954407020912137.

[105] Vayyar Inc., "In-cabin child presence detection." Accessed: Aug. 11, 2022. [Online]. Available: https://vayyar.com/auto/solutions/in-cabin/cpd/

[106] InnoSenT Inc., "Radar data contribute to passenger safety and protecting little ones." Accessed: Aug. 11, 2022. [Online]. Available: https://www.innosent.de/en/automotive/incabin-radar-monitoring/

[107] IEE Smart Sensing Solutions Inc., "Sensing Solutions for Child Presence Detection in Cars." Accessed: Aug. 11, 2022. [Online]. Available: https://iee-sensing.com/automotive/safety-and-comfort/vitasense/

[108] L.-D. Mathieu *et al.*, "Method and system for unattended child detection," Jun. 11, 2020 Accessed: Oct. 07, 2022. [Online]. Available: https://patents.google.com/patent/US20200180472A1/en

[109] G. Freiberger, H. Schreiber, E. Leitgeb, W. Bösch, and D. Veit, "Measurement of a Baby Dummy with a Channel Sounder in an Anechoic Chamber for Child Presence Detection," in *2023 24th International Radar Symposium (IRS)*, 2023, pp. 1–9. doi: 10.23919/IRS57608.2023.10172472.

[110] S. Lim, J. Jung, E. Lee, J. Choi, and S.-C. Kim, "In-Vehicle Passenger Occupancy Detection Using 60-GHz FMCW Radar Sensor," *IEEE Internet Things J*, vol. 11, no. 4, pp. 7002–7012, 2024, doi: 10.1109/JIOT.2023.3313357.

[111] A. Lazaro, N. Munte, R. Villarino, and D. Girbau, "In-Vehicle Monitoring Based on a Low-Cost mm-Wave Radar at 60 GHz," in *2023 SBMO/IEEE MTT-S International Microwave and Optoelectronics Conference (IMOC)*, 2023, pp. 241–243. doi: 10.1109/IMOC57131.2023.10379792.

[112] S. Yoo *et al.*, “Radar Recorded Child Vital Sign Public Dataset and Deep Learning-Based Age Group Classification Framework for Vehicular Application,” *Sensors*, vol. 21, no. 7, 2021, doi: 10.3390/s21072412.

[113] A. C. Ramachandra, V. Viswanatha, K. Kishor, H. Suhas, and E. Pannir Selvam, “In-Cabin Radar Monitoring System: Detection and Localization of People Inside Vehicle Using Vital Sign Sensing Algorithm,” EasyChair, 2022. Accessed: Nov. 23, 2022. [Online]. Available: https://mail.easychair.org/publications/preprint_download/L2rh

[114] J. Möderl, E. Leitinger, F. Pernkopf, and K. Witrisal, “Variational Message Passing-Based Respiratory Motion Estimation and Detection Using Radar Signals,” in *ICASSP 2023 - 2023 IEEE International Conference on Acoustics, Speech and Signal Processing (ICASSP)*, 2023, pp. 1–5. doi: 10.1109/ICASSP49357.2023.10095725.

[115] X. zhang, Q. Wu, and D. Zhao, “Dynamic Hand Gesture Recognition Using FMCW Radar Sensor for Driving Assistance,” in *2018 10th International Conference on Wireless Communications and Signal Processing (WCSP)*, 2018, pp. 1–6. doi: 10.1109/WCSP.2018.8555642.

[116] K. A. Smith, C. Csech, D. Murdoch, and G. Shaker, “Gesture Recognition Using mm-Wave Sensor for Human-Car Interface,” *IEEE Sens Lett*, vol. 2, no. 2, pp. 1–4, 2018, doi: 10.1109/LSENS.2018.2810093.

[117] X. Wang, J. Bai, X. Zhu, L. Huang, and M. Xiong, “Research on Gesture Recognition Algorithm Based on Millimeter-Wave Radar in Vehicle Scene,” SAE Technical Paper, 2022. doi: 10.4271/2022-01-7017.

[118] G. Li, S. Zhang, F. Fioranelli, and H. Griffiths, “Effect of sparsity-aware time–frequency analysis on dynamic hand gesture classification with radar micro-Doppler signatures,” *IET Radar, Sonar & Navigation*, vol. 12, no. 8, pp. 815–820, 2018, doi: 10.1049/iet-rsn.2017.0570.

[119] P. Molchanov, S. Gupta, K. Kim, and K. Pulli, “Multi-sensor system for driver’s hand-gesture recognition,” in *2015 11th IEEE International Conference and Workshops on Automatic Face and Gesture Recognition (FG)*, 2015, pp. 1–8. doi: 10.1109/FG.2015.7163132.

[120] P. Molchanov, S. Gupta, K. Kim, and K. Pulli, “Short-range FMCW monopulse radar for hand-gesture sensing,” in *2015 IEEE Radar Conference (RadarCon)*, 2015, pp. 1491–1496. doi: 10.1109/RADAR.2015.7131232.

[121] F. Khan, S. K. Leem, and S. H. Cho, “Hand-Based Gesture Recognition for Vehicular Applications Using IR-UWB Radar,” *Sensors*, vol. 17, no. 4, 2017, doi: 10.3390/s17040833.

[122] F. Khan and S. H. Cho, “Hand based Gesture Recognition inside a car through IR-UWB Radar,” *Korean Soc. Electron. Eng*, pp. 154–157, 2017, Accessed: Oct. 08, 2022. [Online]. Available: https://repository.hanyang.ac.kr/handle/20.500.11754/106113

[123] A. Farsaei *et al.*, “An IEEE 802.15.4z-Compliant IR-UWB Radar System for In-Cabin Monitoring,” in *2023 IEEE 34th Annual International Symposium on Personal, Indoor and Mobile Radio Communications (PIMRC)*, 2023, pp. 1–5. doi: 10.1109/PIMRC56721.2023.10293800.

[124] A. Shokouhmand, S. Eckstrom, B. Gholami, and N. Tavassolian, “Camera-Augmented Non-Contact Vital Sign Monitoring in Real Time,” *IEEE Sens J*, vol. 22, no. 12, pp. 11965–11978, 2022, doi: 10.1109/JSEN.2022.3172559.

[125] P. Kuchár, R. Pirník, T. Tichý, K. Rástočný, M. Skuba, and T. Tettamanti, “Noninvasive Passenger Detection Comparison Using Thermal Imager and IP Cameras,” *Sustainability*, vol. 13, no. 22, 2021, doi: 10.3390/su132212928.

[126] C. Yang, B. Bruce, X. Liu, B. Gholami, and N. Tavassolian, “A Hybrid Radar-Camera Respiratory Monitoring System Based on an Impulse-Radio Ultrawideband Radar,” in *2020 42nd Annual International Conference of the IEEE Engineering in Medicine & Biology Society (EMBC)*, 2020, pp. 2646–2649. doi: 10.1109/EMBC44109.2020.9175267.

[127] A. Gharamohammadi, A. Khajepour, and G. Shaker, “In-vehicle Monitoring by Radar: A Review,” *IEEE Sens J*, p. 1, 2023, doi: 10.1109/JSEN.2023.3316449.

[128] U. Rajendra Acharya, K. Paul Joseph, N. Kannathal, C. M. Lim, and J. S. Suri, “Heart rate variability: a review,” *Med Biol Eng Comput*, vol. 44, no. 12, pp. 1031–1051, 2006, doi: 10.1007/s11517-006-0119-0.

[129] G. A. Roth *et al.*, “The Burden of Cardiovascular Diseases Among US States, 1990-2016,” *JAMA Cardiol*, vol. 3, no. 5, pp. 375–389, May 2018, doi: 10.1001/jamacardio.2018.0385.

[130] S. Ahmed, Y. Lee, Y.-H. Lim, S.-H. Cho, H.-K. Park, and S. H. Cho, “Noncontact assessment for fatigue based on heart rate variability using IR-UWB radar,” *Sci Rep*, vol. 12, no. 1, p. 14211, 2022, doi: 10.1038/s41598-022-18498-w.

[131] D. Toda, R. Anzai, K. Ichige, R. Saito, and D. Ueki, “ECG Signal Reconstruction Using FMCW Radar and Convolutional Neural Network,” in *2021 20th International Symposium on Communications and Information Technologies (ISCIT)*, 2021, pp. 176–181. doi: 10.1109/ISCIT52804.2021.9590627.

[132] R. Grisot *et al.*, “Monitoring of heart movements using an FMCW radar and correlation with an ECG,” *IEEE Transactions on Radar Systems*, p. 1, 2023, doi: 10.1109/TRS.2023.3298348.

[133] M. Alizadeh, G. Shaker, J. C. M. De Almeida, P. P. Morita, and S. Safavi-Naeini, “Remote Monitoring of Human Vital Signs Using mm-Wave FMCW Radar,” *IEEE Access*, vol. 7, pp. 54958–54968, 2019, doi: 10.1109/ACCESS.2019.2912956.

[134] Y. Rong, A. Dutta, A. Chiriyath, and D. W. Bliss, “Motion-Tolerant Non-Contact Heart-Rate Measurements from Radar Sensor Fusion,” *Sensors*, vol. 21, no. 5, 2021, doi: 10.3390/s21051774.

[135] I. Kakouche, A. Maali, M. N. El Korso, A. Mesloub, and M. S. Azzaz, “Non-contact measurement of respiration and heart rates based on subspace methods and iterative notch filter using UWB impulse radar,” *J Phys D Appl Phys*, vol. 55, no. 3, p. 35401, Oct. 2021, doi: 10.1088/1361-6463/ac2c3b.

[136] S. A. Shah and F. Fioranelli, “RF Sensing Technologies for Assisted Daily Living in Healthcare: A Comprehensive Review,” *IEEE Aerospace and Electronic Systems Magazine*, vol. 34, no. 11, pp. 26–44, 2019, doi: 10.1109/MAES.2019.2933971.

[137] Y. Lee *et al.*, “A Novel Non-contact Heart Rate Monitor Using Impulse-Radio Ultra-Wideband (IR-UWB) Radar Technology,” *Sci Rep*, vol. 8, no. 1, p. 13053, 2018, doi: 10.1038/s41598-018-31411-8.

[138] M. Y. W. Chia, S. W. Leong, C. K. Sim, and K. M. Chan, “Through-wall UWB radar operating within FCC’s mask for sensing heart beat and breathing rate,” in *European Radar Conference, 2005. EURAD 2005.*, 2005, pp. 267–270. doi: 10.1109/EURAD.2005.1605615.

[139] M. Leib, W. Menzel, B. Schleicher, and H. Schumacher, “Vital signs monitoring with a UWB radar based on a correlation receiver,” in *Proceedings of the Fourth European Conference on Antennas and Propagation*, 2010, pp. 1–5.

[140] Y. Nijsure *et al.*, “An Impulse Radio Ultrawideband System for Contactless Noninvasive Respiratory Monitoring,” *IEEE Trans Biomed Eng*, vol. 60, no. 6, pp. 1509–1517, 2013, doi: 10.1109/TBME.2012.2237401.

[141] “Infineon Technologies BGT60TR13C.” Accessed: Jan. 02, 2023. [Online]. Available: https://www.infineon.com/cms/en/product/sensor/radar-sensors/radar-sensors-for-iot/60ghz-radar/bgt60tr13c/

[142] A. Gharamohammadi and A. Shokouhmand, “A robust whitening algorithm to identify buried objects with similar attributes in correlation-based detection,” *J Appl Geophy*, vol. 172, 2020, doi: 10.1016/j.jappgeo.2019.103917.

[143] A. Gharamohammadi, F. Behnia, A. Shokouhmand, and G. Shaker, “Robust Wiener filter-based time gating method for detection of shallowly buried objects,” *IET Signal Processing*, 2021, doi: 10.1049/sil2.12011.

[144] A. Gharamohammadi, F. Behnia, and R. Amiri, “Imaging based on correlation function for buried objects identification,” *IEEE Sens J*, vol. 18, no. 18, 2018, doi: 10.1109/JSEN.2018.2859170.

[145] C. Li and J. Lin, “Random Body Movement Cancellation in Doppler Radar Vital Sign Detection,” *IEEE Trans Microw Theory Tech*, vol. 56, no. 12, pp. 3143–3152, 2008, doi: 10.1109/TMTT.2008.2007139.

[146] M.-C. Tang, F.-K. Wang, and T.-S. Horng, “Single Self-Injection-Locked Radar With Two Antennas for Monitoring Vital Signs With Large Body Movement Cancellation,” *IEEE Trans Microw Theory Tech*, vol. 65, no. 12, pp. 5324–5333, 2017, doi: 10.1109/TMTT.2017.2768363.

[147] T. B. Conroy, X. Hui, P. Sharma, and E. C. Kan, “Heart ID: Biometric Identification Using Wearable MIMO RF Heart Sensors,” *IEEE J Electromagn RF Microw Med Biol*, vol. 7, no. 1, pp. 3–14, 2023, doi: 10.1109/JERM.2022.3223034.

[148] X. Hui, T. B. Conroy, and E. C. Kan, “Multi-Point Near-Field RF Sensing of Blood Pressures and Heartbeat Dynamics,” *IEEE Access*, vol. 8, pp. 89935–89945, 2020, doi: 10.1109/ACCESS.2020.2993994.

[149] S. Abu-Sardanah, A. Gharamohammadi, O. M. Ramahi, and G. Shaker, “A Wearable mm-Wave Radar Platform for Cardiorespiratory Monitoring,” *IEEE Sens Lett*, vol. 7, no. 6, pp. 1–4, 2023, doi: 10.1109/LSENS.2023.3277365.

[150] V. L. Petrović, M. M. Janković, A. V Lupšić, V. R. Mihajlović, and J. S. Popović-Božović, “High-Accuracy Real-Time Monitoring of Heart Rate Variability Using 24 GHz Continuous-Wave Doppler Radar,” *IEEE Access*, vol. 7, pp. 74721–74733, 2019, doi: 10.1109/ACCESS.2019.2921240.

[151] S. Zhang, T. Zheng, Z. Chen, and J. Luo, “Can We Obtain Fine-grained Heartbeat Waveform via Contact-free RF-sensing?,” in *IEEE INFOCOM 2022 - IEEE Conference on Computer Communications*, 2022, pp. 1759–1768. doi: 10.1109/INFOCOM48880.2022.9796905.

[152] S. Fan, Z. Deng, Q. Du, P. Pan, S. Yuan, and X. Huang, “Radiofrequency Doppler echocardiography,” *Measurement*, vol. 220, p. 113305, 2023, doi: https://doi.org/10.1016/j.measurement.2023.113305.

[153] K. Yamamoto, K. Toyoda, and T. Ohtsuki, “Spectrogram-Based Non-Contact RRI Estimation by Accurate Peak Detection Algorithm,” *IEEE Access*, vol. 6, pp. 60369–60379, 2018, doi: 10.1109/ACCESS.2018.2875737.

[154] F. Wang, X. Zeng, C. Wu, B. Wang, and K. J. R. Liu, “mmHRV: Contactless Heart Rate Variability Monitoring Using Millimeter-Wave Radio,” *IEEE Internet Things J*, vol. 8, no. 22, pp. 16623–16636, 2021, doi: 10.1109/JIOT.2021.3075167.

[155] H. Zhang *et al.*, “Radar-Beat: Contactless beat-by-beat heart rate monitoring for life scenes,” *Biomed Signal Process Control*, vol. 86, p. 105360, 2023, doi: https://doi.org/10.1016/j.bspc.2023.105360.

[156] Z. Chen, T. Zheng, C. Cai, and J. Luo, “MoVi-Fi: Motion-Robust Vital Signs Waveform Recovery via Deep Interpreted RF Sensing,” in *Proceedings of the 27th Annual International Conference on Mobile Computing and Networking*, in MobiCom ’21. New York, NY, USA: Association for Computing Machinery, 2021, pp. 392–405. doi: 10.1145/3447993.3483251.

[157] G. Yuan, N. A. Drost, and R. A. McIvor, “Respiratory rate and breathing pattern,” *McMaster Univ. Med. J*, vol. 10, no. 1, pp. 23–25, 2013, Accessed: Oct. 09, 2022. [Online]. Available: https://www.mangalam.nl/wp-content/uploads/2018/12/Breathing-Pattern.pdf

[158] G. B. Smith, D. R. Prytherch, P. E. Schmidt, and P. I. Featherstone, “Review and performance evaluation of aggregate weighted ‘track and trigger’ systems,” *Resuscitation*, vol. 77, no. 2, pp. 170–179, 2008, doi: 10.1016/j.resuscitation.2007.12.004.

[159] C. A. Alvarez *et al.*, “Predicting out of intensive care unit cardiopulmonary arrest or death using electronic medical record data,” *BMC Med Inform Decis Mak*, vol. 13, no. 1, p. 28, 2013, doi: 10.1186/1472-6947-13-28.

[160] J.-K. Park *et al.*, “Noncontact RF Vital Sign Sensor for Continuous Monitoring of Driver Status,” *IEEE Trans Biomed Circuits Syst*, vol. 13, no. 3, pp. 493–502, 2019, doi: 10.1109/TBCAS.2019.2908198.

[161] K. E. , B. S. , B. S. M. , & B. H. L. Barrett, *Ganong’s review of medical physiology twenty*. McGraw Hill Lange, 2010.

[162] E. Martin, *Concise colour medical dictionary*. Oxford University Press, 2015.

[163] J. W. Choi, D. H. Yim, and S. H. Cho, “People Counting Based on an IR-UWB Radar Sensor,” *IEEE Sens J*, vol. 17, no. 17, pp. 5717–5727, 2017, doi: 10.1109/JSEN.2017.2723766.

[164] J. W. Choi, X. Quan, and S. H. Cho, “Bi-Directional Passing People Counting System Based on IR-UWB Radar Sensors,” *IEEE Internet Things J*, vol. 5, no. 2, pp. 512–522, 2018, doi: 10.1109/JIOT.2017.2714181.

[165] J. W. Choi, S. H. Cho, Y. S. Kim, N. J. Kim, S. S. Kwon, and J. S. Shim, “A counting sensor for inbound and outbound people using IR-UWB radar sensors,” in *2016 IEEE Sensors Applications Symposium (SAS)*, 2016, pp. 1–5. doi: 10.1109/SAS.2016.7479903.

[166] N. Munte, A. Lazaro, R. Villarino, and D. Girbau, “Vehicle Occupancy Detector Based on FMCW mm-Wave Radar at 77 GHz,” *IEEE Sens J*, vol. 22, no. 24, pp. 24504–24515, 2022, doi: 10.1109/JSEN.2022.3218454.

[167] C. and M. S. Breuer Pia and Eckes, “Hand Gesture Recognition with a Novel IR Time-of-Flight Range Camera–A Pilot Study,” in *Computer Vision/Computer Graphics Collaboration Techniques*, W. Gagalowicz André and Philips, Ed., Berlin, Heidelberg: Springer Berlin Heidelberg, 2007, pp. 247–260. doi: 10.1007/978-3-540-71457-6_23.

[168] F. al Farid *et al.*, “A Structured and Methodological Review on Vision-Based Hand Gesture Recognition System,” *J Imaging*, vol. 8, no. 6, 2022, doi: 10.3390/jimaging8060153.

[169] W. Zhao, R. Chellappa, P. J. Phillips, and A. Rosenfeld, “Face Recognition: A Literature Survey,” *ACM Comput. Surv.*, vol. 35, no. 4, pp. 399–458, Dec. 2003, doi: 10.1145/954339.954342.

[170] L. Yu, H. Abuella, M. Z. Islam, J. F. O’Hara, C. Crick, and S. Ekin, “Gesture Recognition Using Reflected Visible and Infrared Lightwave Signals,” *IEEE Trans Hum Mach Syst*, vol. 51, no. 1, pp. 44–55, 2021, doi: 10.1109/THMS.2020.3043302.

[171] F. and K. Y. E. and A. L. Keskin Cem and Kraç, “Real Time Hand Pose Estimation Using Depth Sensors,” in *Consumer Depth Cameras for Computer Vision: Research Topics and Applications*, J. and G. H. and R. X. and K. K. Fossati Andrea and Gall, Ed., London: Springer London, 2013, pp. 119–137. doi: 10.1007/978-1-4471-4640-7_7.

[172] X. Zeng, F. Wang, B. Wang, C. Wu, K. J. R. Liu, and O. C. Au, “In-Vehicle Sensing for Smart Cars,” *IEEE Open Journal of Vehicular Technology*, vol. 3, pp. 221–242, 2022, doi: 10.1109/OJVT.2022.3174546.

[173] Y.-H. Lin, J.-H. Cheng, L.-C. Chang, W.-J. Lin, J.-H. Tsai, and T.-W. Huang, “A Broadband MFCW Agile Radar Concept for Vital-Sign Detection Under Various Thoracic Movements,” *IEEE Trans Microw Theory Tech*, pp. 1–15, 2022, doi: 10.1109/TMTT.2022.3186014.

[174] S. M. A. T. Hosseini and H. Amindavar, “A New Ka-Band Doppler Radar in Robust and Precise Cardiopulmonary Remote Sensing,” *IEEE Trans Instrum Meas*, vol. 66, no. 11, pp. 3012–3022, 2017, doi: 10.1109/TIM.2017.2714480.

[175] A. T. Purnomo, K. S. Komariah, D.-B. Lin, W. F. Hendria, B.-K. Sin, and N. Ahmadi, “Non-Contact Supervision of COVID-19 Breathing Behaviour with FMCW Radar and Stacked Ensemble Learning Model in Real-Time,” *IEEE Trans Biomed Circuits Syst*, pp. 1–15, 2022, doi: 10.1109/TBCAS.2022.3192359.

[176] C. Gu, G. Wang, T. Inoue, and C. Li, “Doppler radar vital sign detection with random body movement cancellation based on adaptive phase compensation,” in *2013 IEEE MTT-S International Microwave Symposium Digest (MTT)*, 2013, pp. 1–3. doi: 10.1109/MWSYM.2013.6697618.

[177] K. Prażnowski, J. Mamala, M. Śmieja, and M. Kupina, “Assessment of the Road Surface Condition with Longitudinal Acceleration Signal of the Car Body,” *Sensors*, vol. 20, no. 21, 2020, doi: 10.3390/s20215987.

[178] A. Lazaro, D. Girbau, and R. Villarino, “Techniques for Clutter Suppression in the Presence of Body Movements during the Detection of Respiratory Activity through UWB Radars,” *Sensors*, vol. 14, no. 2, pp. 2595–2618, 2014, doi: 10.3390/s140202595.

[179] S. Yue, H. He, H. Wang, H. Rahul, and D. Katabi, “Extracting Multi-Person Respiration from Entangled RF Signals,” *Proc ACM Interact Mob Wearable Ubiquitous Technol*, vol. 2, pp. 1–22, Jul. 2018, doi: 10.1145/3214289.

[180] Z. Xu *et al.*, “Simultaneous Monitoring of Multiple People’s Vital Sign Leveraging a Single Phased-MIMO Radar,” *IEEE J Electromagn RF Microw Med Biol*, pp. 1–10, 2022, doi: 10.1109/JERM.2022.3143431.

[181] Z. Ling, W. Zhou, Y. Ren, J. Wang, and L. Guo, “Non-Contact Heart Rate Monitoring Based on Millimeter Wave Radar,” *IEEE Access*, vol. 10, pp. 74033–74044, 2022, doi: 10.1109/ACCESS.2022.3190355.

[182] L. Ren, H. Wang, K. Naishadham, O. Kilic, and A. E. Fathy, "Phase-Based Methods for Heart Rate Detection Using UWB Impulse Doppler Radar," *IEEE Trans Microw Theory Tech*, vol. 64, no. 10, pp. 3319–3331, 2016, doi: 10.1109/TMTT.2016.2597824.

[183] X. Hu and T. Jin, "Short-Range Vital Signs Sensing Based on EEMD and CWT Using IR-UWB Radar," *Sensors*, vol. 16, no. 12, 2016, doi: 10.3390/s16122025.

[184] M.-C. Huang, J. J. Liu, W. Xu, C. Gu, C. Li, and M. Sarrafzadeh, "A Self-Calibrating Radar Sensor System for Measuring Vital Signs," *IEEE Trans Biomed Circuits Syst*, vol. 10, no. 2, pp. 352–363, 2016, doi: 10.1109/TBCAS.2015.2411732.

[185] S. Kazemi, A. Ghorbani, H. Amindavar, and D. R. Morgan, "Vital-Sign Extraction Using Bootstrap-Based Generalized Warblet Transform in Heart and Respiration Monitoring Radar System," *IEEE Trans Instrum Meas*, vol. 65, no. 2, pp. 255–263, 2016, doi: 10.1109/TIM.2015.2482230.

[186] J. Yan, H. Hong, H. Zhao, Y. Li, C. Gu, and X. Zhu, "Through-Wall Multiple Targets Vital Signs Tracking Based on VMD Algorithm," *Sensors*, vol. 16, no. 8, 2016, doi: 10.3390/s16081293.

[187] Z. Yu, D. Zhao, and Z. Zhang, "Doppler Radar Vital Signs Detection Method Based on Higher Order Cyclostationary," *Sensors*, vol. 18, no. 1, 2018, doi: 10.3390/s18010047.

[188] L. Qu, S. Lian, Y. Sun, and L. Zhang, "Doppler Radar Vital Sign Detection Based on Complex Continuous Basis Pursuit Algorithm," in *2018 Progress in Electromagnetics Research Symposium (PIERS-Toyama)*, Jul. 2018, pp. 2371–2377. doi: 10.23919/PIERS.2018.8597866.

[189] X. Liang, H. Zhang, S. Ye, G. Fang, and T. Aaron Gulliver, "Improved denoising method for through-wall vital sign detection using UWB impulse radar," *Digit Signal Process*, vol. 74, pp. 72–93, 2018, doi: 10.1016/j.dsp.2017.12.004.

[190] M. Li and J. Lin, "Wavelet-Transform-Based Data-Length-Variation Technique for Fast Heart Rate Detection Using 5.8-GHz CW Doppler Radar," *IEEE Trans Microw Theory Tech*, vol. 66, no. 1, pp. 568–576, 2018, doi: 10.1109/TMTT.2017.2730182.

[191] N. and B.-L. O. and L. V. M. and P. B.-K. and Z. Q. Høst-Madsen Anders and Petrochilos, "Signal Processing Methods for Doppler Radar Heart Rate Monitoring," in *Signal Processing Techniques for Knowledge Extraction and Information Fusion*, M. and K. A. and O. D. and T. T. Mandic Danilo and Golz, Ed., Boston, MA: Springer US, 2008, pp. 121–140. doi: 10.1007/978-0-387-74367-7_7.

[192] S. Kazemi, A. Ghorbani, H. Amindavar, and C. Li, "Cyclostationary approach to Doppler radar heart and respiration rates monitoring with body motion cancelation using Radar Doppler System," *Biomed Signal Process Control*, vol. 13, pp. 79–88, 2014, doi: 10.1016/j.bspc.2014.03.012.

[193] J. Chen, D. Zhang, Z. Wu, F. Zhou, Q. Sun, and Y. Chen, "Contactless Electrocardiogram Monitoring With Millimeter Wave Radar," *IEEE Trans Mob Comput*, pp. 1–17, 2022, doi: 10.1109/TMC.2022.3214721.

[194] H. Zhao, Y. Ma, Y. Han, C. Tian, and X. Huang, "T-HSER: Transformer Network Enabling Heart Sound Envelope Signal Reconstruction Based on Low Sampling Rate Millimeter Wave Radar," *IEEE Internet Things J*, p. 1, 2023, doi: 10.1109/JIOT.2023.3291051.

[195] Z. Chen, Y. Liu, C. Sui, M. Zhou, and Y. Song, "A Novel Scheme for Suppression of Human Motion Effects in Non-Contact Heart Rate Detection," *IEEE Access*, vol. 11, pp. 84241–84257, 2023, doi: 10.1109/ACCESS.2023.3302918.

[196] K. Shi *et al.*, "Contactless analysis of heart rate variability during cold pressor test using radar interferometry and bidirectional LSTM networks," *Sci Rep*, vol. 11, no. 1, p. 3025, 2021, doi: 10.1038/s41598-021-81101-1.

[197] J.-Y. Park *et al.*, "Preclinical evaluation of noncontact vital signs monitoring using real-time IR-UWB radar and factors affecting its accuracy," *Sci Rep*, vol. 11, no. 1, p. 23602, 2021, doi: 10.1038/s41598-021-03069-2.

[198] X. Liang, J. Deng, H. Zhang, and T. A. Gulliver, "Ultra-Wideband Impulse Radar Through-Wall Detection of Vital Signs," *Sci Rep*, vol. 8, no. 1, p. 13367, 2018, doi: 10.1038/s41598-018-31669-y.

[199] X. Yang, Z. Zhang, Y. Huang, Y. Zheng, and Y. Shen, "Using a graph-based image segmentation algorithm for remote vital sign estimation and monitoring," *Sci Rep*, vol. 12, no. 1, p. 15197, 2022, doi: 10.1038/s41598-022-19198-1.

[200] S. M. J. M. Straus *et al.*, "Prolonged QTc Interval and Risk of Sudden Cardiac Death in a Population of Older Adults," *J Am Coll Cardiol*, vol. 47, no. 2, pp. 362–367, 2006, doi: 10.1016/j.jacc.2005.08.067.

[201] J. Qiao *et al.*, "Contactless multiscale measurement of cardiac motion using biomedical radar sensor," *Front Cardiovasc Med*, vol. 9, 2022, doi: 10.3389/fcvm.2022.1057195.

[202] C. Gu and C. Li, "Assessment of Human Respiration Patterns via Noncontact Sensing Using Doppler Multi-Radar System," *Sensors*, vol. 15, no. 3, pp. 6383–6398, 2015, doi: 10.3390/s150306383.

[203] Texas Instruments Inc., "User's Guide AWRx Cascaded Radar RF Evaluation Module (MMWCAS-RF-EVM)." Accessed: Aug. 16, 2023. [Online]. Available: https://www.ti.com/tool/MMWCAS-RF-EVM

[204] M. Chmurski, G. Mauro, A. Santra, M. Zubert, and G. Dagasan, "Highly-Optimized Radar-Based Gesture Recognition System with Depthwise Expansion Module," *Sensors*, vol. 21, no. 21, 2021, doi: 10.3390/s21217298.

[205] "Calculating Your Average Torso Length Relative to Height." Accessed: Jan. 02, 2023. [Online]. Available: https://hikemuch.com/average-torso-length/

[206] J. Ai, X. Qi, W. Yu, Y. Deng, F. Liu, and L. Shi, "A New CFAR Ship Detection Algorithm Based on 2-D Joint Log-Normal Distribution in SAR Images," *IEEE Geoscience and Remote Sensing Letters*, vol. 7, no. 4, pp. 806–810, 2010, doi: 10.1109/LGRS.2010.2048697.

[207] W. A. N. D. M. Z. Wang Bin AND Shi, "Confidence Analysis of Standard Deviational Ellipse and Its Extension into Higher Dimensional Euclidean Space," *PLoS One*, vol. 10, no. 3, pp. 1–17, May 2015, doi: 10.1371/journal.pone.0118537.

[208] "The mechanics of breathing." Accessed: Apr. 30, 2023. [Online]. Available: https://www.msdmanuals.com/home/lung-and-airway-disorders/biology-of-the-lungs-and-airways/control-of-breathing?fbclid=IwAR26fowcz65g54LBF6z3o_XaE3lLDUTiy4oenDp0Nm0hD2zknFx3nEhug44

[209] "Online Metronome." Accessed: Jun. 17, 2022. [Online]. Available: https://metronome-online.com/15-bpm

[210] Q. Zhai, X. Han, Y. Han, J. Yi, S. Wang, and T. Liu, "A Contactless On-Bed Radar System for Human Respiration Monitoring," *IEEE Trans Instrum Meas*, vol. 71, pp. 1–10, 2022, doi: 10.1109/TIM.2022.3164145.

[211] "AWR6443, AWR6843 Single-Chip 60- to 64-GHz mmWave Sensor datasheet." Accessed: Feb. 26, 2024. [Online]. Available: https://www.ti.com/lit/ds/symlink/awr6843.pdf

[212] A. Gharamohammadi and G. Shaker, "A novel back-projection algorithm improved by antenna pattern automatized by 2-D CFAR," in *2022 IEEE International Symposium on Antennas and Propagation and USNC-URSI Radio Science Meeting (AP-S/URSI)*, 2022, pp. 1158–1159. doi: 10.1109/AP-S/USNC-URSI47032.2022.9886587.

[213] A. Gharamohammadi, Y. Norouzi, and H. Aghaeinia, "Optimized UWB signal to shallow buried object imaging," *Progress in Electromagnetics Research Letters*, vol. 72, 2018, doi: 10.2528/PIERL17091506.

[214] A. Gharamohammadi, F. Behnia, and A. Shokouhmand, "Imaging Based on a Fast Back-Projection Algorithm Considering Antenna Beamwidth," in *2019 6th Iranian Conference on Radar and Surveillance Systems, ICRSS 2019*, 2019. doi: 10.1109/ICRSS48293.2019.9026574.

[215] A. Gharamohammadi, F. Behnia, and A. Shokouhmand, "Machine learning based identification of buried objects using sparse whitened NMF," *arXiv*. 2019.

[216] M. O. Bagheri, A. Gharamohammadi, S. Abu-Sardanah, O. M. Ramahi, and G. Shaker, "Radar near-field sensing using metasurface for biomedical applications," *Communications Engineering*, vol. 3, no. 1, p. 51, 2024, doi: 10.1038/s44172-024-00194-4.

[217] A. R. Hunt, “Use of a Frequency-Hopping Radar for Imaging and Motion Detection Through Walls,” *IEEE Transactions on Geoscience and Remote Sensing*, vol. 47, no. 5, pp. 1402–1408, 2009, doi: 10.1109/TGRS.2009.2016084.

[218] S. S. and S. G. Hamidi Shahrokh and Naeini, “An Overview of Vital Signs Monitoring Based on RADAR Technologies,” in *Sensing Technology*, B. and J. K. P. and R. J. K. and M. S. C. Suryadevara Nagender Kumar and George, Ed., Cham: Springer International Publishing, 2022, pp. 113–124.

[219] “Bella rose baby doll.” Accessed: Sep. 28, 2023. [Online]. Available: https://www.bradfordexchange.ca/

[220] R. Klabunde, *Cardiovascular physiology concepts*. Lippincott Williams & Wilkins, 2011.

[221] C. Li and J. Lin, “Optimal Carrier Frequency of Non-contact Vital Sign Detectors,” in *2007 IEEE Radio and Wireless Symposium*, 2007, pp. 281–284. doi: 10.1109/RWS.2007.351823.

[222] A. Gharamohammadi, M. Pirani, A. Khajepour, and G. Shaker, “Multibin Breathing Pattern Estimation by Radar Fusion for Enhanced Driver Monitoring,” *IEEE Trans Instrum Meas*, vol. 73, pp. 1–12, 2024, doi: 10.1109/TIM.2023.3345909.

[223] “Frontier X belt.” Accessed: Oct. 23, 2023. [Online]. Available: https://fourthfrontier.com/pages/frontierx-for-cardiac-care

[224] “BioRadio piezo electric respiratory effort belt .” Accessed: Oct. 23, 2023. [Online]. Available: https://www.glneurotech.com/product/piezo-electric-respiratory-effort-belt/

[225] H.-S. Cho, B. Choi, and Y.-J. Park, “Monitoring heart activity using ultra-wideband radar,” *Electron Lett*, vol. 55, no. 16, pp. 878–881, 2019, doi: https://doi.org/10.1049/el.2019.1438.

[226] Y. Du, C. Liu, D. Wu, and S. Li, “Application of Vehicle Mounted Accelerometers to Measure Pavement Roughness,” *Int J Distrib Sens Netw*, vol. 12, no. 6, p. 8413146, 2016, doi: 10.1155/2016/8413146.

[227] J. Yu *et al.*, “SenSpeed: Sensing Driving Conditions to Estimate Vehicle Speed in Urban Environments,” *IEEE Trans Mob Comput*, vol. 15, no. 1, pp. 202–216, 2016, doi: 10.1109/TMC.2015.2411270.

[228] J. Ruiz, H. Wu, and M. A. Colominas, “Enhancing Missing Data Imputation of Non-stationary Signals with Harmonic Decomposition,” *arXiv e-prints*, p. arXiv:2309.04630, Sep. 2023, doi: 10.48550/arXiv.2309.04630.

[229] Y. Nagasaka, “Lung Sounds in Bronchial Asthma,” *Allergology International*, vol. 61, no. 3, pp. 353–363, 2012, doi: 10.2332/allergolint.12-RAI-0449.

[230] G. Shanthakumari and E. Priya, “Performance Analysis: Preprocessing of Respiratory Lung Sounds,” in *Artificial Intelligence*, J. Hemanth, T. Silva, and A. Karunananda, Eds., Singapore: Springer Singapore, 2019, pp. 289–300.

[231] A. Basra, B. Mukhopadhayay, and S. Kar, “Temperature sensor based ultra low cost respiration monitoring system,” in *2017 9th International Conference on Communication Systems and Networks (COMSNETS)*, 2017, pp. 530–535. doi: 10.1109/COMSNETS.2017.7945448.

[232] C.-L. Wei, C.-F. Lin, and I.-T. Tseng, “A Novel MEMS Respiratory Flow Sensor,” *IEEE Sens J*, vol. 10, no. 1, pp. 16–18, 2010, doi: 10.1109/JSEN.2009.2035192.

[233] O. M. P. SIngh and M. B. Malarvili, “Review of Infrared Carbon-Dioxide Sensors and Capnogram Features for Developing Asthma-Monitoring Device.,” *Journal of Clinical & Diagnostic Research*, vol. 12, no. 10, 2018, doi: 10.7860/JCDR/2018/35870.12099.

[234] S. Xiao *et al.*, “Fast-response ionogel humidity sensor for real-time monitoring of breathing rate,” *Mater Chem Front*, vol. 3, no. 3, pp. 484–491, 2019, doi: 10.1039/C8QM00596F.

[235] S. H. Hwang *et al.*, “Unconstrained Sleep Apnea Monitoring Using Polyvinylidene Fluoride Film-Based Sensor,” *IEEE Trans Biomed Eng*, vol. 61, no. 7, pp. 2125–2134, 2014, doi: 10.1109/TBME.2014.2314452.

[236] A. Siqueira, A. F. Spirandeli, R. Moraes, and V. Zarzoso, “Respiratory Waveform Estimation From Multiple Accelerometers: An Optimal Sensor Number and Placement Analysis,” *IEEE J Biomed Health Inform*, vol. 23, no. 4, pp. 1507–1515, 2019, doi: 10.1109/JBHI.2018.2867727.

[237] J. L. Moraes, M. X. Rocha, G. G. Vasconcelos, J. E. Vasconcelos Filho, V. H. C. de Albuquerque, and A. R. Alexandria, “Advances in Photopletysmography Signal Analysis for Biomedical Applications,” *Sensors*, vol. 18, no. 6, 2018, doi: 10.3390/s18061894.

[238] P. H. Charlton, T. Bonnici, L. Tarassenko, D. A. Clifton, R. Beale, and P. J. Watkinson, “An assessment of algorithms to estimate respiratory rate from the electrocardiogram and photoplethysmogram,” *Physiol Meas*, vol. 37, no. 4, pp. 610–626, Mar. 2016, doi: 10.1088/0967-3334/37/4/610.

[239] C. B. Pereira, X. Yu, M. Czaplik, R. Rossaint, V. Blazek, and S. Leonhardt, “Remote monitoring of breathing dynamics using infrared thermography,” *Biomed. Opt. Express*, vol. 6, no. 11, pp. 4378–4394, Nov. 2015, doi: 10.1364/BOE.6.004378.

[240] K. Nakajima, Y. Matsumoto, and T. Tamura, “Development of real-time image sequence analysis for evaluating posture change and respiratory rate of a subject in bed,” *Physiol Meas*, vol. 22, no. 3, pp. N21–N28, Jul. 2001, doi: 10.1088/0967-3334/22/3/401.

[241] A. Shahshahani, C. Laverdiere, S. Bhadra, and Z. Zilic, “Ultrasound Sensors for Diaphragm Motion Tracking: An Application in Non-Invasive Respiratory Monitoring,” *Sensors*, vol. 18, no. 8, 2018, doi: 10.3390/s18082617.

[242] H. Lee, B.-H. Kim, J.-K. Park, S. W. Kim, and J.-G. Yook, “A Resolution Enhancement Technique for Remote Monitoring of the Vital Signs of Multiple Subjects Using a 24 Ghz Bandwidth-Limited FMCW Radar,” *IEEE Access*, vol. 8, pp. 1240–1248, 2020, doi: 10.1109/ACCESS.2019.2961130.

[243] M. Ali, A. Elsayed, A. Mendez, Y. Savaria, and M. Sawan, “Contact and Remote Breathing Rate Monitoring Techniques: A Review,” *IEEE Sens J*, vol. 21, no. 13, pp. 14569–14586, 2021, doi: 10.1109/JSEN.2021.3072607.

[244] C. Massaroni, A. Nicolò, D. Lo Presti, M. Sacchetti, S. Silvestri, and E. Schena, “Contact-Based Methods for Measuring Respiratory Rate,” *Sensors*, vol. 19, no. 4, 2019, doi: 10.3390/s19040908.

[245] P. S. Addison, J. N. Watson, M. L. Mestek, J. P. Ochs, A. A. Uribe, and S. D. Bergese, “Pulse oximetry-derived respiratory rate in general care floor patients,” *J Clin Monit Comput*, vol. 29, no. 1, pp. 113–120, 2015, doi: 10.1007/s10877-014-9575-5.

[246] P. S. Addison, J. N. Watson, M. L. Mestek, J. P. Ochs, A. A. Uribe, and S. D. Bergese, “Pulse oximetry-derived respiratory rate in general care floor patients,” *J Clin Monit Comput*, vol. 29, no. 1, pp. 113–120, 2015, doi: 10.1007/s10877-014-9575-5.

[247] E. Cardillo and A. Caddemi, “Radar Range-Breathing Separation for the Automatic Detection of Humans in Cluttered Environments,” *IEEE Sens J*, vol. 21, no. 13, pp. 14043–14050, 2021, doi: 10.1109/JSEN.2020.3024961.

[248] M. Alizadeh, G. Shaker, and S. Safavi-Naeini, “Experimental study on the phase analysis of FMCW radar for vital signs detection,” in *2019 13th European Conference on Antennas and Propagation (EuCAP)*, 2019, pp. 1–4.

[249] D. G. Cacuci, M. Ionescu-Bujor, and I. M. Navon, *Sensitivity and uncertainty analysis, volume II: applications to large-scale systems*. CRC press, 2005.

[250] M. Zakrzewski, A. Vehkaoja, A. S. Joutsen, K. T. Palovuori, and J. J. Vanhala, “Noncontact Respiration Monitoring During Sleep With Microwave Doppler Radar,” *IEEE Sens J*, vol. 15, no. 10, pp. 5683–5693, 2015, doi: 10.1109/JSEN.2015.2446616.

Appendices

Appendix A
Comparison Between Different BR Estimation Sensors

In this part, different BR estimation techniques have been compared for in-cabin sensing applications. Figure A.1 represents different techniques to estimate BR, whether contact-based or remote-based.

Sound sensing is one of the earliest sorts of medical tests. However, it is not accurate and proper for continuous monitoring [229], [230]. A thermistor under the nose is used in the temperature sensing approach to measure the temperature differential between the air being breathed and exhaled [231]. In the pressure sensing method, when the airflow is supplied to the sensor, the sensor deforms, and its resistance varies. The sensor output voltage changes linearly because of this [232]. By measuring the amount of carbon dioxide (CO_2) that the person has exhaled, one may determine their BR. The most used technique for calculating the quantity of CO_2 in gas samples is IR spectroscopy [233]. A humidity sensor positioned close to the patient's nose or mouth can be used to monitor BR since the expelled air is more humid than the air inhaled [234]. In chest movement estimation, a thin sheet of the piezoelectric substance can be used to quantify how much the body volume changes while breathing [235]. Another approach to estimating chest wall activity among contact sensors is the accelerometer. Using the accelerometer and/or gyroscope sensors, it is possible to track the movements of the thoracic and/or abdominal cavities to identify breathing activity [236]. An optical, non-invasive technique used to measure blood perfusion across tissues is called photoplethysmography (PPG). It is based on using IR light to illuminate blood vessels, often through the patient's finger. The quantity of IR light reflected or absorbed by blood is then measured by a PPG sensor, which indicates changes in blood volume [237]. Devices for ECG track the electrical field in the chest that the heart and breathing make [238].

IR thermography is an approach to measuring BR since the temperature near the nostrils changes during the breathing cycle (it is 31.17°C during inspiration and 31.44°C during expiration) [239]. Analysis of chest movements in various ROIs recorded by a video camera might be used to derive BRs [240]. In the Ultrasound approach, the sensor's attenuation characteristics are used to calculate the sensor's distance from the subject. Then, based on the phase of the detected peak, the BR can be estimated [241]. In addition, acoustic waves are unable to travel over great distances and can be quickly disrupted by mechanical motion [95]. Hence, it is not a suitable selection for in-cabin monitoring applications. Using radars has been

investigated widely to estimate BRs in several applications. The reflected signal from the chest wall can be used to estimate BR [242].

Table A. 1 compares different BR monitoring techniques. This evaluation is based on some parameters that can be applied to continuous monitoring. Based on several factors in [243], a radar sensor is the best solution inside a vehicle, especially because of its comfort level and protection of privacy. Doppler radars based on phase shift are capable of detecting human body vibration. Chest wall displacement caused by breathing and heart vibrations can be sensed to monitor people inside a car [25]. To achieve this goal, many aspects should be investigated.

Table A. 1: Comparison between different BR monitoring techniques [243].

Method	Integrated solution	Installation on the body	The comfort level for continuous monitoring	Privacy issues	Price issue
Sound sensing	No	Direct contact	High	Yes	No
Temperature sensing	No	Direct contact	Low	No	No
CMOS MEMS-based	Yes	Direct contact	Low	No	Yes
CO_2 sensing	No	Direct contact	Low	No	No
Humidity sensing	No	Direct contact	Low	No	No
Piezoelectric transducer	Yes	On a dress or bed mattress	Low	No	No
Accelerometer	No	Direct contact	Low	No	No
Impedance fluctuation sensing	No	On a dress or chair	High	No	No
IR thermography	No	No contact	High	Yes	No
Ultrasound	No	No contact/ contact	High	No	No
radar	Yes	No contact	High	No	No

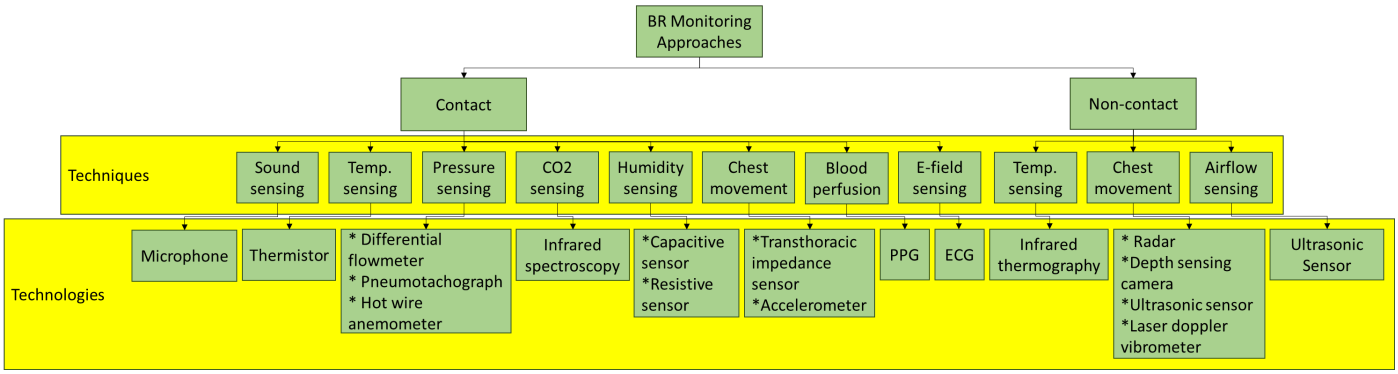

Figure A.1: BR monitoring techniques [243], [244].

Appendix B
Ground Truth

Different investigations used different types of ground truths to assess their proposed algorithms for vital sign monitoring inside a car. As can be seen in Table B.1, the most common ground truth for the evaluation of estimated BR is pulse oximetry. Figure B. 1 shows the Pulse oximeter used in [20]. It is a non-intrusive way to measure oxygen saturation, which can lead to BR and HR [52], [245], [246].

Figure B. 1: Pulse oximeter used in [20].

Table B. 1: Comparison between the different in-cabin published papers for vital sign monitoring based on their setup, namely, sensor place, frequency, ground truth, and Radar brand and/or package size.

Reference	Sensor place	Frequency (GHz)	Ground truth	Radar brand and/or package size
[25]	Mobile holder (right side of steering wheel)	60	Airflow, Temperature sensor	XM132 (25×20 mm)
[28], [32]	In front of the chest of the main subject	60	ECG	XM112
[34]	on the steering wheel	4.3	Edan iM50	Not specified

[43]	Rearview mirror	7.25	A USB pressing button to count breaths as a ground truth	X2M200 (50×70 mm)
[53]	The upper left of the windshield	7.5	Pulse oximetry	X4M300 (50×70 mm)
[52]	In front of the chest of the main subject	77	Pulse oximetry	Not specified
[47]	Under the steering wheel	6.8	Nasal breath sound recordings from a smartphone, ECG (PSL-iECG2)	X2 (50×70 mm)
[20]	The upper left of the windshield	7.29 and 8.748	Pulse oximetry	X4M300 (50×70 mm)
[48]	The lower left of the steering wheel	2.4	Self-assessment of the participant for being drowsy	Not specified
[57]	Behind the seat	60	A pressure sensor is worn on the abdomen	50×50 mm
[45]	Under the steering wheel	77	ECG, Respiration belt	IWR1843BOOST
[44]	Behind the seat	24	ECG	Not specified
[51]	In the driver's seat	Millimeter wave	Camera, Wearable physiological detection instrument	Not specified
[30]	Rearview mirror	77	Polar H10 heart monitor	AWR1642BOOST
[31]	Rearview mirror	120	Spirometer	Not specified
[112]	The left top side of the subjects' chest	60	A clinical reference sensor BSM6501K	IWR6843

Appendix C
Radar Brand and/or Package Size

The most common brand used by recent investigators is XeThru. Their dimensions are less than 50×70 mm. Hence, it is a suitable selection for in-cabin applications. Figure C. 2 shows the used radar and radar setup inside a vehicle for vital sign monitoring of the driver [20].

(a) **(b)**

Figure C. 2: X4M300 used in [20]: (a) radar board and (b) radar setup inside a car for vital sign monitoring of driver.

Appendix D
Micro-Doppler Signatures for In-Cabin Applications

Micro-doppler signatures inside a vehicle can be used in different applications, including abnormal driver behavior detection, occupancy detection, and gesture recognition for driver assistance.

One of the solutions to detect drowsy and distracted drivers is based on micro-doppler signatures, especially head motions [59], [60], [61]. In [61], different head motions have been classified based on velocity-time maps by a neural network. A millimeter wave radar in 77 GHz has been placed in front of the driver to monitor the driver's head, as seen in Figure D. 1. In [59], the range-time maps, on the other hand, have been utilized to monitor the head movements by a 61 GHz radar. Distracted drivers by mobile have been investigated along with vital sign monitoring [47]. It is shown that using mobile while driving can be detected based on reflected signals after suppressing clutter.

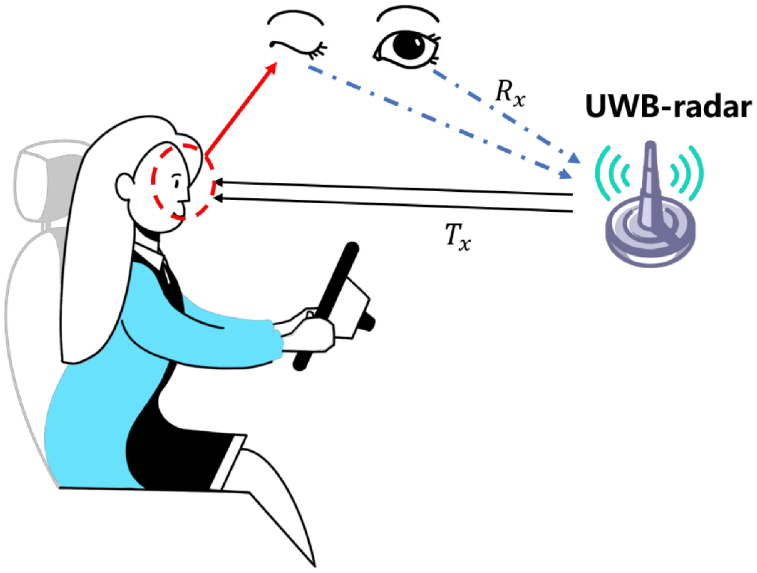

Figure D. 1: The eye blink radar setup [65].

Another approach to detecting the drowsy driver is based on monitoring eyeblinks [21], [65], [66], [67], [68], [69]. In [66], [68], a 77 GHz radar was used for recording signals from eyeblink. They have used ensemble empirical mode decomposition to decompose signals. Based on useful information, the signals were reconstructed and fed to a short-time Fourier transformation. Finally, a cell average CFAR has been

applied to detect eye blinks. However, in [69], other vital signs like heartbeat and respiration were filtered before applying CFAR. Figure D. 2 shows the eye blink in the time-frequency spectrum.

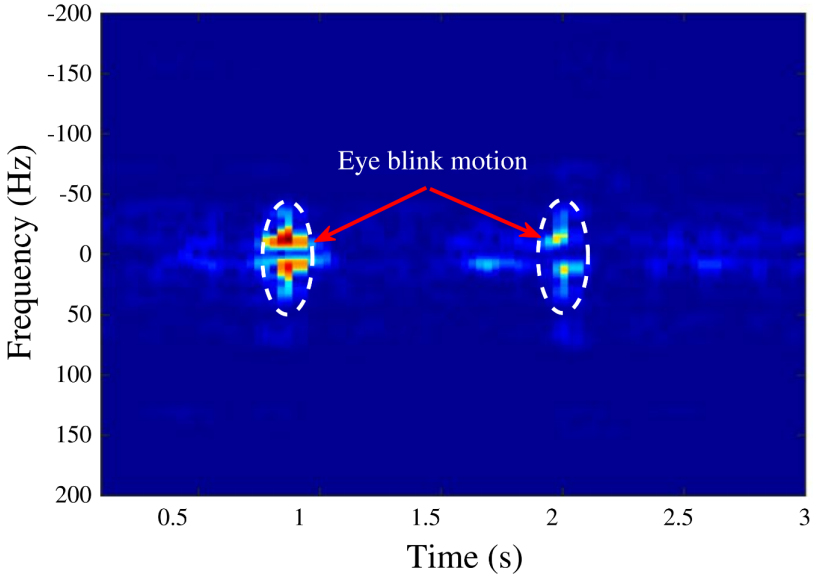

Figure D. 2: The eye blink in the time-frequency spectrum [68].

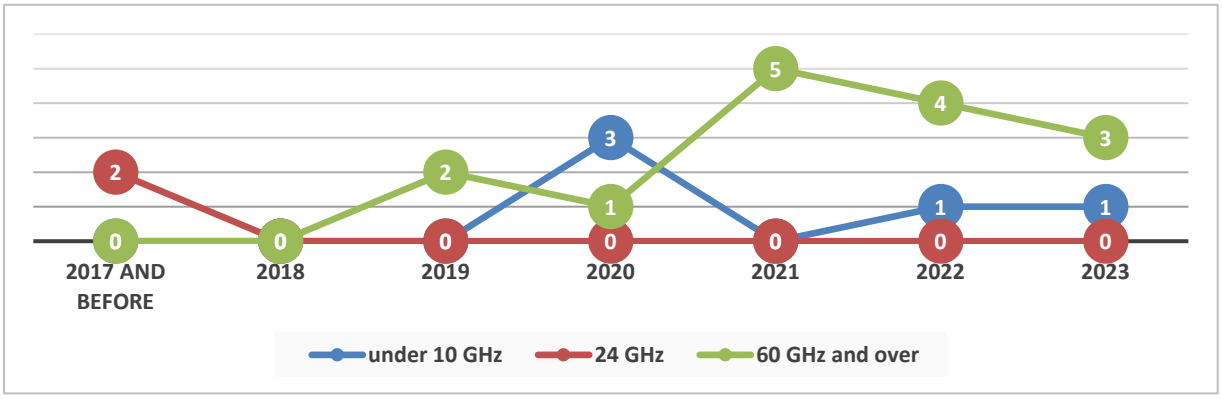

Figure D. 3: Distribution of recent studies in frequency selection for occupancy detection inside a vehicle by radar over the years.

Occupancy detection is one of the most popular in-cabin applications. Recent studies have mostly focused on micro-doppler signatures. These signatures will appear in processed raw signals. Most recent studies extracted features from processed raw radar signals [7], [11], [25], [70], [73], [75], [78], [98], [99], [100], [102]. These features are fed to an AI approach to be used in classification. These signatures can also

appear in different types of data like time–frequency [71], [72], [73], [77], [79]. Another factor in occupancy detection application by radar inside a vehicle is frequency selection. As seen in Table D. 1 and Figure D. 3, most in-cabin sensing investigations by radar for occupancy detection have used millimeter wave radar (60 GHz and over). Regarding sensor placement, because the radar should be placed under the car roof in occupancy detection applications, the dimensions of the radar package are less important in comparison to vital sign monitoring applications. More details about the recent works can be found in Table D. 1.

Table D. **2** compares the different in-cabin published papers for occupancy detection based on their accuracy or advantages and limitations by radar. All the recent investigations have reached more than 90% accuracy, but some limitations should be addressed in the next publications. One of the most important limitations is the use of inappropriate methods to estimate vital signs in occupancy detection. In [77], [79], the assumed HR does not cover children's HR properly, and there is no harmonic analysis for HR estimation. The HR of children can be more than 120 beats per minute [112]. In [77], the BR is also considered to be less than 18, while it can be higher for children [112].

In [6], [71], to train the AI approach, all gathered data are pooled and shuffled. Although this method might offer extremely high accuracy, the evaluation method cannot be used for new measurements. Because radar has many samples per second, combining all samples and selecting a part of them to test would not guarantee that test samples were fully invisible to the model.

Some studies have designed their occupancy detection algorithms to detect a single occupied seat [25]. Hence, their proposed method cannot be used for multiple-person occupancy detection. These algorithms are applied before vital sign monitoring, especially for the driver vital sign monitoring application [25].

The employed radar system has a direct effect on efficiency. The number of receivers determines the angular resolution of the radar. More receiver channels will result in better angular resolution and better discrimination. In [70], [78], [79], the authors could use more channels to have better angular resolution and reliable results. However, they have used one receiver to collect data. By one receiver, the FMCW radar cannot discriminate targets in the same range accurately [124]. As seen in Figure D. 4, seat 4 and seat 3 have the same time distance from the radar. A radar with more receivers can discriminate against them.

Figure D. 4: The radar setup in [70]. Seat 3 and seat 4 have the same time distance from the radar. The discrimination of these two seats is possible by having more receivers.

Table D. 1: Comparison between the different in-cabin published papers for occupancy detection based on setup frequency and methodology by radar.

Reference	Frequency (GHz)	Data representation	Approach	Other considerations
[77]	7.29	Spatial-temporal-circulated gray level co-occurrence matrix	Stochastic gradient descent using 3 different classifiers	• Extracted features by singular value ratio from vital signs, including BR, and HR
[70]	6.8	Processed raw radar signals	Deep neural network	• The model has been evaluated by changing the activation function, the number of nodes in hidden layers, and the number of layers
[78]	6.8	Extracted statistical features from raw radar signals	Bagging with decision tree	• A feature selection approach based on neighborhood component analysis is used to select the best features.
[7]	61	The spectral power and Wiener entropy of processed raw radar signals	Linear discriminant analysis and maximum likelihood estimation	
[6], [74]	77	Range-azimuth	KNN, SVM, and random forest	
[75]	60	Point cloud map	An enhanced Euclidean clustering	• Adaptive monitoring of target presence by an enhanced Euclidean clustering as well as a state machine technique

[11], [73]	77	Processed raw radar signals	KNN, SVM, and random forest	• For the left-behind human detection, a novel approach based on correlation has been employed
[72]	2.45	Time-frequency	Binary decision tree	• There are three specific extracted features based on the degree of scattering points and vital signs to detect people.
[71]	77	Range-azimuth	SVM	
[79]	61	Time-frequency	AUC, SMD, Bhattacharyya coefficient and Hellinger distance	
[80]	60	Range-doppler	Regression predictions based on a novel loss function, namely Label-Aware Ranked loss	
[25]	60	Processed raw radar signals	The standard deviation of the envelope amplitude	
[98], [99]	24	Processed raw radar signals	Cross-correlation	
[100]	80	Processed raw radar signals	Peak detection	• An antenna design for in-cabin sensing
[102]	24	Processed raw radar signals	Peak detection	• A patch antenna design for in-cabin sensing
[97]	0.868			• A patch antenna design for occupancy detection
[101]	24			• Simulation of the in-cabin environment to study the multipath effect on reflected signals.

Table D. 2: Comparison between the different in-cabin published papers for occupancy detection based on their accuracy or advantages and limitations of radar.

Reference	Accuracy or advantages	Limitations
[77]	• In counting the number of occupied seats in a stationary and moving vehicle, the accuracy is 97.5% and 97%, respectively. • A novel feature extraction method based on spatial-temporal-circulated gray-level co-occurrence matrix. • Collecting a valuable database	• No harmonic analysis to estimate HR. • The BR is assumed to be 12 to 18. But it could be more than 18 [112]. • The HR is assumed to be 60 to 120. But it could be more than 120 [112].
[70]	• Classification accuracy by deep neural network: 99.5% • Collecting a valuable database	• The designed radar system works with a single receiver. More receivers are required to discriminate targets from different angles.
[78]	• Classification accuracy: More than 90%. • A deep investigation of statistical feature extraction	• The designed radar system works with a single receiver. More receivers are required to discriminate targets from different angles. • lower age diversity in experiments
[7]	• The average accuracy of linear discriminant analysis and MLE: 96.14% and 98.88%, respectively.	• The designed radar system works with a single receiver. More receivers are required to discriminate targets from different angles instead of referring to the range. • More features can be extracted to have reliable results.
[6], [74]	• The accuracy of the multiclass classification and binary classification methods: 97%	• No theoretical information for the CFAR detector • Inappropriate model evaluation based on k-fold
[75]	• The accuracy of detection in different postures: more than 84% • The accuracy of detection of dynamic experiments: more than 91%	• No theoretical background for a CFAR detector
[11], [73]	• The accuracy of occupancy detection is more than 90% • The accuracy of left-behind human detection is 100%	• There is not enough theoretical background in threshold detection in the proposed algorithm for left-behind human detection.
[72]	• The average classification accuracy for a human with or without motion is 98.6%.	• Multi-passenger has not been tested.
[71]	• The accuracy of occupancy detection in each row of a car is 97.8%.	• The occupancy of detection has not been tested for each seat of a row separately. • Inappropriate model evaluation
[79]	• The performance of the proposed method for passenger detection is	• The designed radar system works with a single receiver. More receivers are required

	validated by an area under the curve greater than 0.98.	to discriminate targets from different angles instead of referring to the range. • No harmonic analysis to estimate HR. • The HR is assumed to be 48 to 108. But it could be more than 120 [112].
[25]	• Accurate occupancy detection	• Single-seat occupancy detection
[98], [99]	• The sensor is highly robust to noise and environmental influences like traffic or weather, resulting in fewer false alarms.	• Single-seat occupancy detection • Not enough tests have been done
[100]	• The peak of the reflected signal from a human differs significantly from that of an unoccupied seat. • A unique antenna design for in-cabin sensing	• Single-seat occupancy detection • Lack of collected data in real driving environments

One of the hottest research areas is hand-based gesture detection, which is crucial for creating human-computer interfaces. An in-cabin gesture interface can help the driver to do a variety of functions. Using radar for gesture recognition for the human-car interface inside a vehicle by radar can overcome other kinds of sensor issues, especially privacy concerns and unaffordable prices [121]. In addition, it is a contactless sensor and can work in a dark environment [116].

Recent studies have considered several parameters in their system design. The first parameter is the used frequency. Recent papers have mostly used mm-wave radar to have accurate detections. As seen in Table D. 3, higher frequencies are more sensitive to small RCS changes and would have better results [115]. The bandwidth signal determines the range resolution. Better range resolution provides better and more accurate data for classification. To have better range resolution and better Doppler signatures, recent studies have used the maximum frequency bandwidth of employed radar. Recent studies mostly employed a package radar to be easily used inside a car.

Based on the expected functionality of the system, other crucial variables will be defined. One of the key elements is how many gestures are proposed to be determined. The task of classification will become more challenging with more gestures. According to recent studies, there are typically 7 to 8 features to classify and identify. Another crucial element is the distance of the hand from the radar. Most recent investigations have proposed that their algorithms can identify gestures in hand-to-radar distances up to 100 centimeters.

Table D. 3: Comparison between different in-cabin published papers for gesture recognition for human-car interface by radar.

Reference	Data representation and data dimensions	Approach	Frequency (GHz)	No. of gestures	Hand-to-radar distance (cm)	No. of participants and samples for each gesture
[116]	Range–Doppler (2D)	Random forest	60	6	Not specified	Not specified, 20
[117]	Range-doppler, horizontal angle-range, and pitch angle-range(3D)	3DCNN and series LSTM network	60	8	10-90	4, 1000, (2 seconds for each recording)
[115]	Time-frequency (2D)	CNN	77	9	20-100	Not specified, 360
[118]	Time-frequency (2D)	Decision tree	25	6	0-30	4, 60, (4 seconds for each recording)
[119]	Time-frequency receiver 1, time-frequency receiver 2, and time-frequency receiver 3 (3D)	3DCNN	24	10	0-50	3, 1714
[121]	Frequency of the reflected signal, Variation of time of arrival, the variance of the probability density function	K-means	6.8	5	0-100	3, 50
[120]	Time–Doppler (2D)	Energy estimation	25	10	0-150	Not specified
[122]	3 extracted features from the time-range (the variance of the hand's displacement, the magnitude variance, and the hand's surface area)	Neural Network	6.8	6	Not specified	1, Not specified (10 seconds for each recording)

Appendix E
FMCW Radar Fundamentals

FMCW radar has some advantages over other radar systems. The first one is the high-range resolution. This radar can discriminate targets in range accurately due to high-frequency bandwidth [143], [144], [213]. This kind of radar can work with millimeter wave signals and is sensitive to insignificant changes in the range of the target. It can estimate chest wall displacements accurately [247]. In addition, it is highly robust to noise since the useful information is usually in its phase. Hence, it is less sensitive to noise than impulse radar [133].

Radars transmit an electromagnetic signal into an environment in which there are many reflectors. The wave's echo is then collected by radar receivers. A sinusoidal signal is swept by an FMCW radar from f_{min} to f_{max}. The frequency bandwidth of an FMCW signal is f_{max} - f_{min}. A signal known as the beat signal is created once the received signal at the output port of the receiver antenna is correlated with the transmitted signal. The beat signal provides details about targets. For example, the frequency difference between the sent and received chirps can achieve the range of the target in the received signal [133].

Assume that the transmitted signal is:

$$x_{Tx}(t) = A_{Tx}\cos\left(2\pi f_c t + \pi\frac{B}{T}t^2\right), \tag{E.1}$$

where A_{Tx} is the amplitude of the transmitted signal, f_c is the carrier frequency, B is frequency bandwidth, and T is the duration of every chirp. The slope of the chirp is:

$$k = \frac{B}{T}. \tag{E.2}$$

By applying this assumption, the transmitted signal will be:

$$x_{Tx}(t) = A_{Tx}\cos(2\pi f_c t + \pi k t^2). \tag{E.3}$$

The reflected signal off a target with a delay of t_d is as follows:

$$x_{Rx}(t) = A_{Rx}\cos(2\pi f_c(t - t_d) + \pi k(t - t_d)^2), \tag{E.4}$$

in which A_{Rx} is the amplitude of the received signal. An attenuated version of the transmitted signal will be correlated with the received signal. Then, the filtered version of the output signal will be the beat signal. The beat signal is as follows:

$$y(t) = \alpha . x_{Tx}(t) . x_{Rx}(t) = \alpha A_{Tx} \cos(2\pi f_c t + \pi k t^2) . A_{Rx} \cos(2\pi f_c (t - t_d) + \pi k (t - t_d)^2) \xrightarrow{\text{low pass filter}} \alpha A_{Tx} A_{Rx} \cos(2\pi f_c t_d + 2\pi k (t . t_d - {t_d}^2)), \quad \text{(E.5)}$$

in which α is the attenuation factor. By assuming that $t_d << t$, the y(t) can be simplified as follows:

$$y(t) \approx \alpha A_{Tx} A_{Rx} \cos(2\pi f_c t_d + 2\pi k t t_d). \quad \text{(E.6)}$$

The time delay in the beat signal depends on the range of the target [248]. If the target is a moving object like the chest wall of the human body, the delay is:

$$t_d = \frac{2R(t)}{c}, \quad \text{(E.7)}$$

where R(t) is the range of the target, hence, the beat signal based on a time-varying range of the target is:

$$y(t) \approx \alpha A_{Tx} A_{Rx} \cos(\frac{4\pi f_c R(t)}{c} + \frac{4\pi k t R(t)}{c}). \quad \text{(E.8)}$$

The beat frequency and phase of the beat signal can be expressed as follows:

$$\omega_b(t) = \frac{4\pi k R(t)}{c}, \quad \text{(E.9)}$$

$$\psi(t) = \frac{4\pi f_c R(t)}{c}.$$

The beat signal is a cosine wave. Its frequency and phase have the information of range. The sensitivity of phase and frequency to the target's range can be compared [249]. The sensitivity of phase to the target's range in comparison with the sensitivity of frequency to the target's range is as follows:

$$\frac{\frac{d\psi(t)}{dR(t)}}{\frac{d\omega_b(t)}{dR(t)}} = \frac{k}{f_c} = \frac{B}{f_c . T}. \quad \text{(E.10)}$$

For example, when f_c is 60 GHz, B is 5 GHz, and T is 64 μs, the sensitivity of phase to chest wall vibrations is by far more than frequency. Hence, after taking a FFT from the beat signal, the phase can be employed to estimate the BR of subjects.

The chest wall displacement can be calculated as follows [124]:

$$R(t) = \frac{\psi(t) . c}{4\pi f_c}. \quad \text{(E.11)}$$

The chest wall displacement rate is equal to the BR. The BR is the frequency of peak after taking FFT from the chest wall displacement [133].

Appendix F

Further Discussion on the Signal Processing Chain for BR Estimation

In this appendix, some further methods in the signal processing chain are discussed. It completes the proposed approach for BR estimation.

The DC value of the signal must be eliminated; otherwise, the phase quality will be affected [248]. In the frequency domain, the DC of a signal is at zero frequency. Figure E.1 represents a raw signal in the frequency domain before and after DC bias removal. The zero frequency of this raw signal becomes zero after this process.

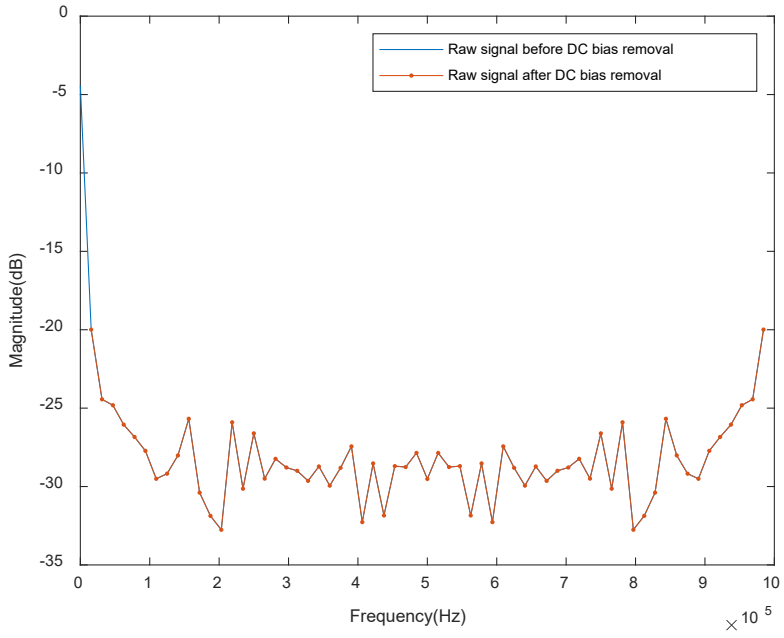

Figure E. 1: A raw signal before and after DC bias removal.

Figure E. 2 shows the range-slow time-frame cube reconstructed from raw signals after the fast time FFT. For a specific range, a matrix of slow time frames will be processed to estimate breathing signals [133].

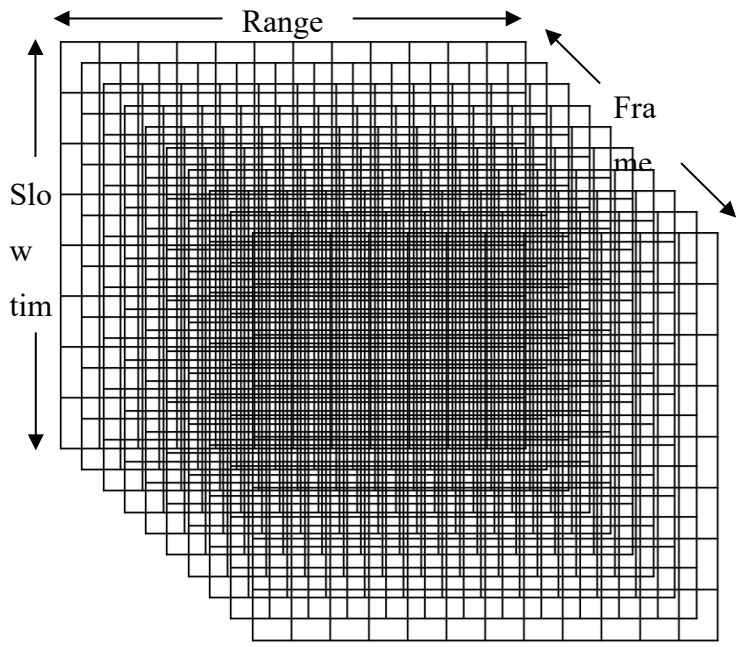

Figure E. 2: Range-slow time-frame cube.

Another used approach in the proposed signal processing chain is the phase unwrapping algorithm. Figure G.3 shows this algorithm [250].

```
threshold = pi;
for i = 1:N-1
    if (phase(i+1)-phase(i) > threshold)
        for j = i+1:N
            phase(j) = phase(j)-2*pi;
        end
    else
        if (phase(i+1)-phase(i) < -threshold)
            for j = i+1:N
                phase(j) = phase(j)+2*pi;
            end
        end
    end
end
```

Figure E. 3: Phase unwrapping algorithm.

The mean subtraction from the breathing signal removes non-vibrational clutters with strong reflections [248]. Figure E. 4 shows how mean subtraction removes the constant range of the target from the breathing signal.

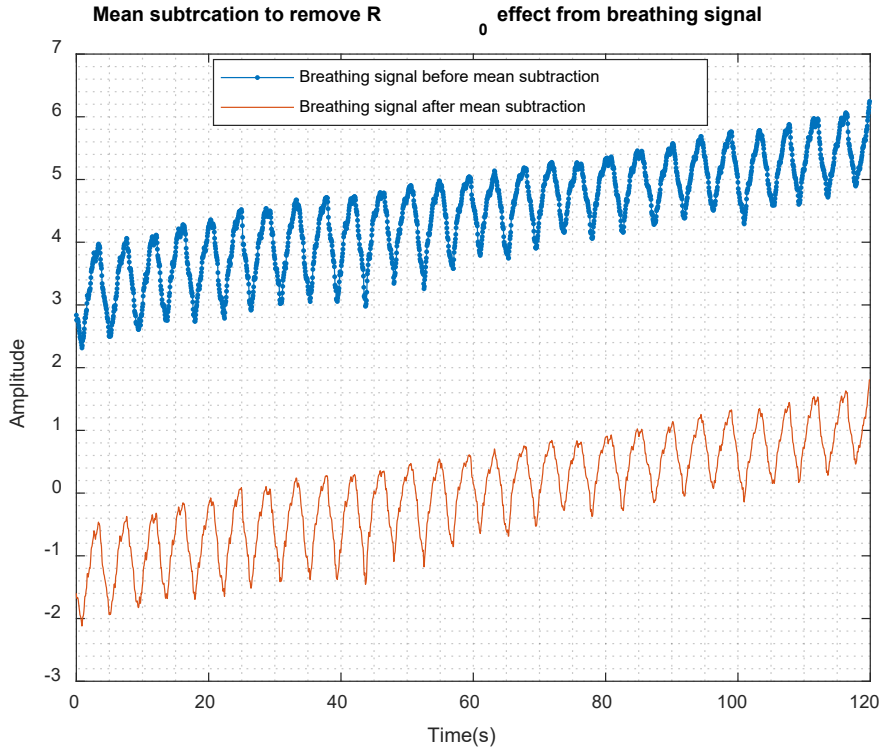

Figure E. 4: mean subtraction to remove a constant range of targets from the breathing signal.

The breathing signal should be filtered to remove unwanted vibrations and estimate the BR. Figure E. 5 shows the frequency response of the designed filters. The magnitude of out-of-band signals is suppressed by almost 10 and 20 dB, respectively. Additionally, the phase of the filters has a line equation, resulting in constant time delays in signals. Figure E. 6 depicts the magnitude of the breathing signal before and after these two filters. The applied filters suppressed out-of-band signals significantly, while in-band ones remained without any attenuation. The ripple of the pass band is low. A high ripple can affect the breathing signal waveform.

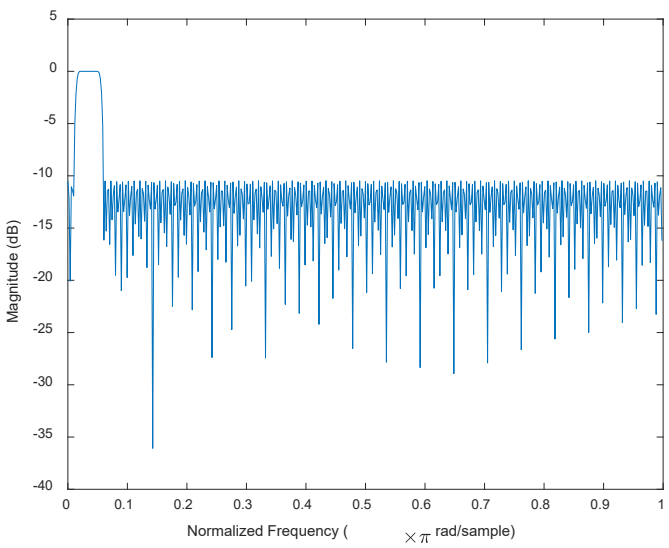

(a)

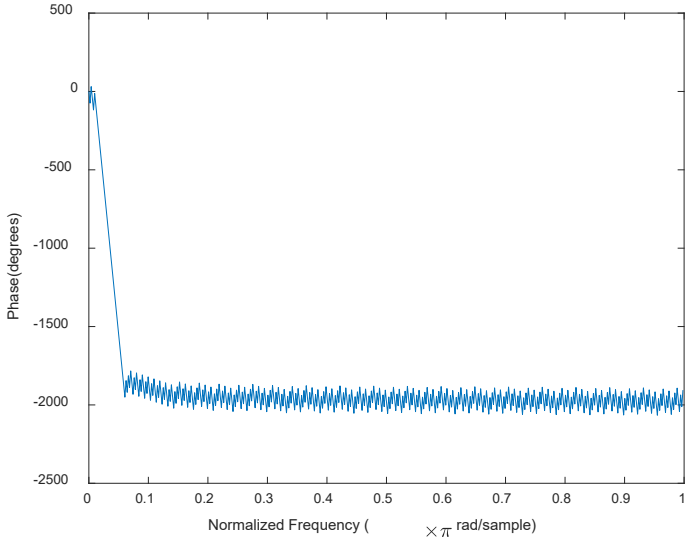

(b)

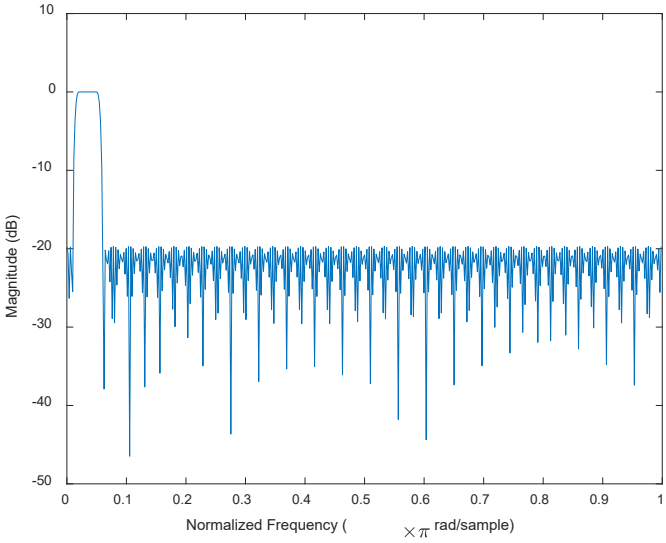

(c)

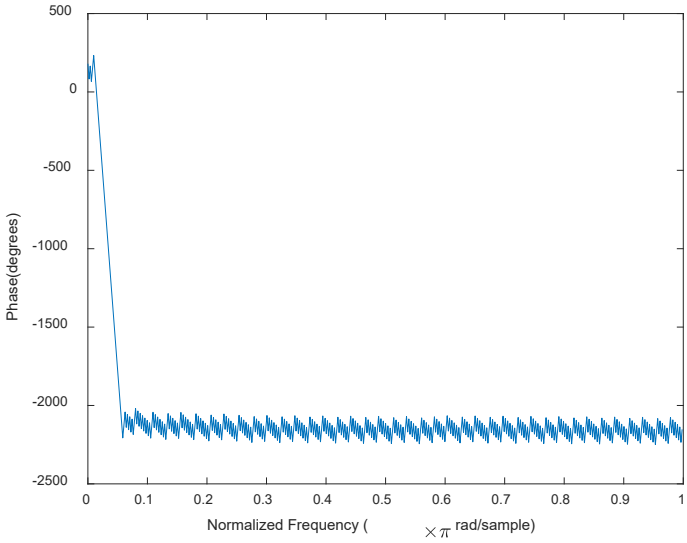

(d)

Figure E. 5: Frequency response of two assumed filters (a) magnitude of the frequency response of an FIR filter with 10 dB loss for out-of-band signals, (b) phase of the frequency response of an FIR filter with 10 dB loss for out-of-band signals, (c) magnitude of the frequency response of an FIR filter with 20 dB loss for out-of-band signals, and (d) phase of the frequency response of an FIR filter with 20 dB loss for out-of-band signals.

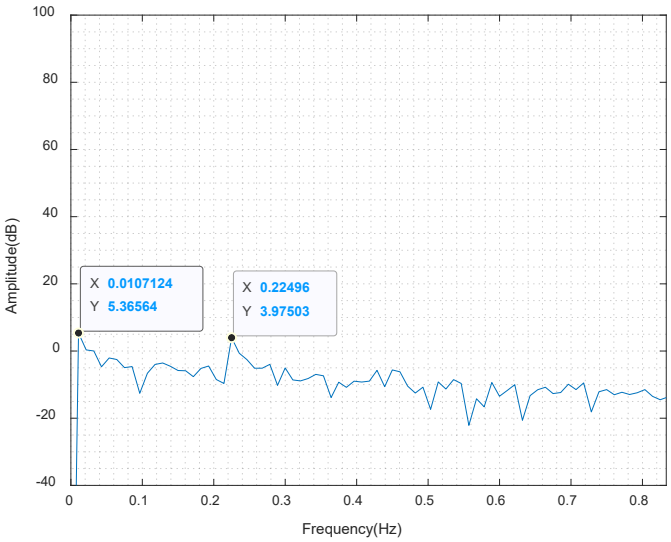

(a)

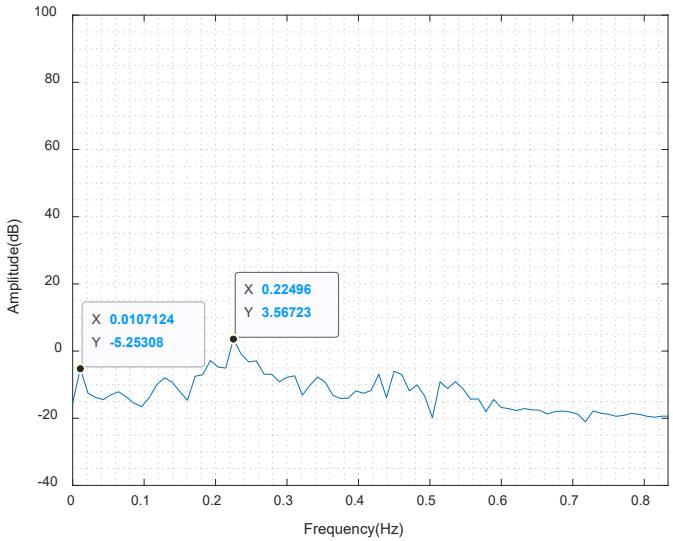

(b)

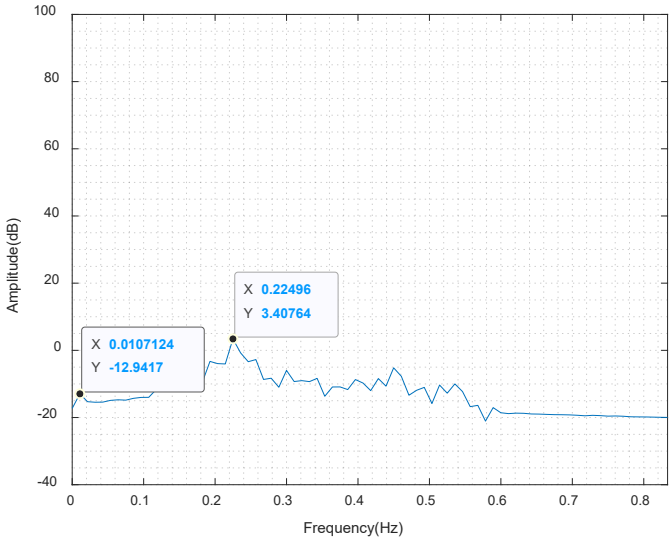

(c)

Figure E. 6: The magnitude of the breathing signal in the frequency domain: (a) before filtering, (b) after filtering by a filter with 10 dB loss for out-of-bound signals, and (c) after filtering by a filter with 20 dB loss for out-of-bound signals.

The human body vibrations can make many harmonics. Figure E. 7 shows the harmonics of a pulse train in the frequency domain. The frequency distance of two sequential harmonics in the frequency domain is the frequency of the pulse train. The breathing signal resembles a pulse train. There exists breathing harmonics, heartbeat harmonics, and a combination of both in the human vibration signal [134]. Figure E.

8 shows the harmonics of human body vibrations in the frequency domain. F_b is the breathing signal frequency. There are other harmonic components with frequencies nF_b for n=2,3,4. F_h is the heartbeat signal frequency. The main problem of harmonics is other harmonic components with frequencies $F_b - nF_h$ for n=1,2. They can make BR estimation difficult.

Another issue with BR estimation in the frequency domain is having a strong $2F_b$. Figure E. 9 depicts two simulated breathing patterns with different peak frequencies. The peak frequency of the first breathing pattern is two times of the second one. But they are very similar in the time domain. Figure E. 10 shows two chest wall displacements from one measurement estimated in two sequential range bins. The estimated BR for the first one is two times the actual BR. But the second one has an accurate estimation. In this research proposal, the wrong estimation based on the second harmonic has been replaced by the actual value based on other range bins. This is another advantage of using more than one range bin for BR estimation.

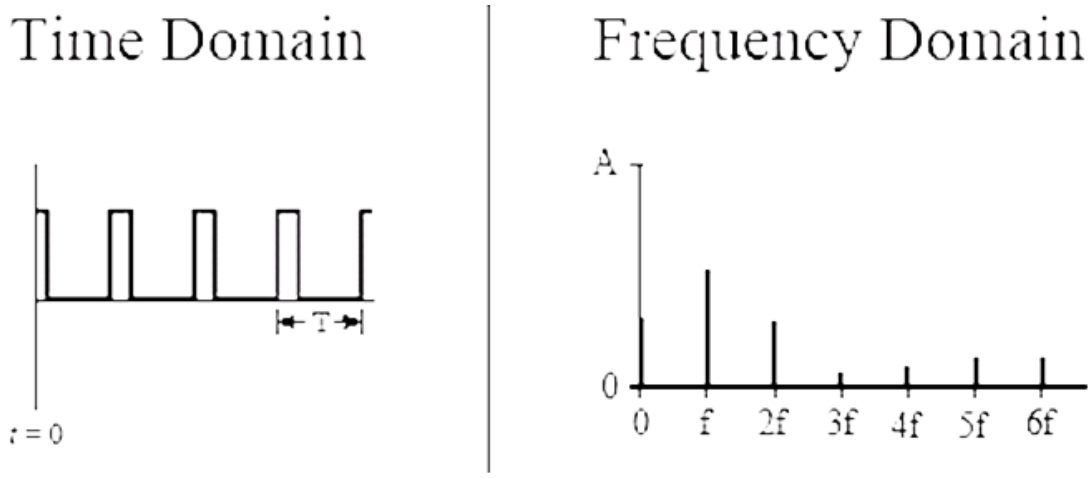

Figure E. 7: A pulse train in the frequency and time domains.

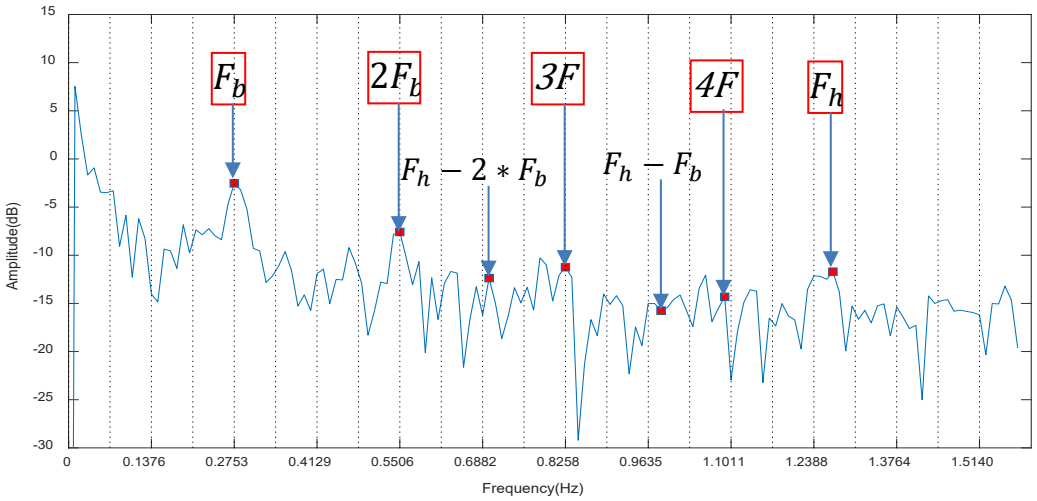

Figure E. 8: Human vibration signal in the frequency domain.

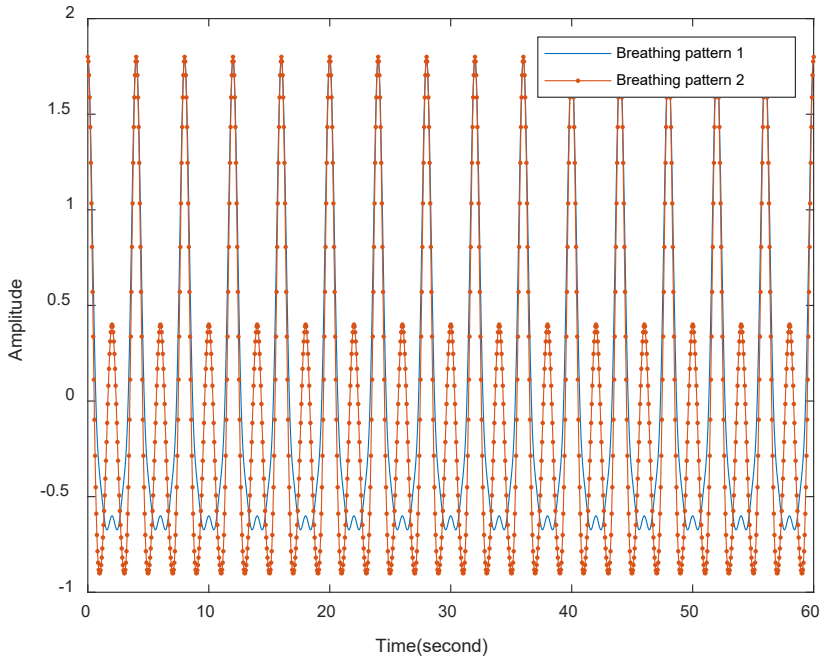

Figure E. 9: Two simulated breathing patterns with different peak frequencies.

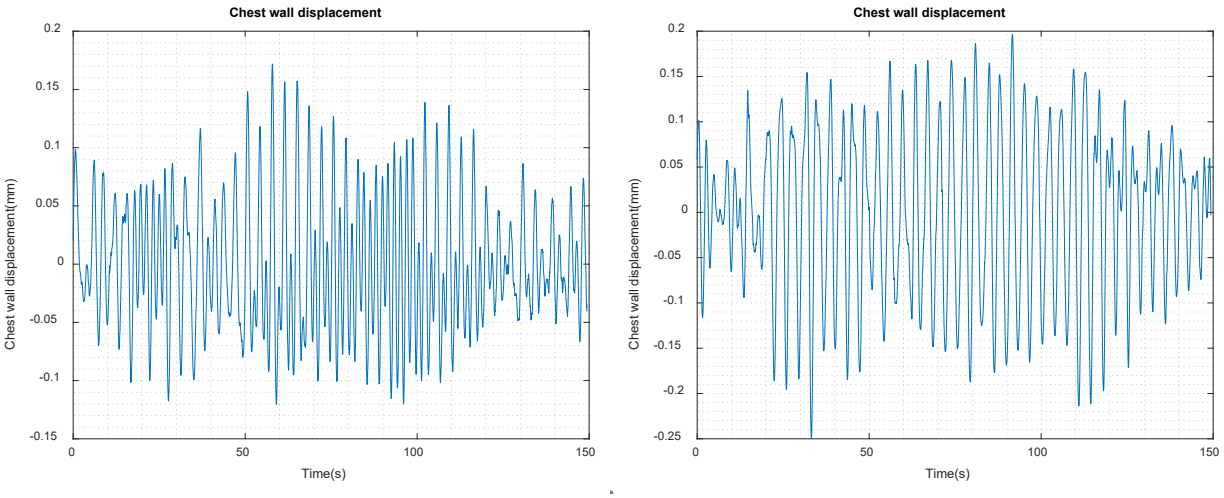

(a) (b)

Figure E. 10: Two breathing patterns estimated from one measurement in two sequential range bins: (a) the estimated BR is two times the actual BR, and (b) the estimated BR is equal to the actual BR.